Industrial Chemistry & Materials

REVIEW

Check for updates

Unlocking the potential of chemical-assisted water electrolysis for green hydrogen production†

Jiwoo Lee,[a] Sol A. Lee,[ab] Tae Hyung Lee[c] and Ho Won Jang [iD] *[ad]

Despite global efforts to reduce the use of fossil fuels, carbon dioxide (CO_2) emissions continue to rise. As the demand for clean energy grows, hydrogen (H_2), which does not emit CO_2 during combustion, is emerging as a promising energy resource. Among the various hydrogen production technologies, water electrolysis is attracting attention as a method for producing green hydrogen without carbon emissions. However, its high reaction overpotentials, due to complex reaction pathways, are a major factor limiting its energy efficiency. To address these issues, chemical-assisted water electrolysis is considered as an innovative alternative. This technology enables hydrogen production at lower voltages. Moreover, it can generate high-value products and remove pollutants, providing both environmental and energy benefits. In this review, we introduce various types of chemical-assisted water electrolysis and discuss the latest advances in catalyst design and reaction mechanisms aimed at reducing applied system voltage. Finally, we address the main challenges and prospects of chemical-assisted water electrolysis.

Keywords: Chemical-assisted water electrolysis; Hybrid water electrolysis; Overpotential; Hydrogen; Electrocatalyst; Value-added product.

a Department of Materials Science and Engineering, Research Institute of Advanced Materials, Seoul National University, Seoul 08826, Republic of Korea. E-mail: hwjang@snu.ac.kr

b Department of Applied Physics and Materials Science, California Institute of Technology, Pasadena 91126, USA

c School of Chemical and Biological Engineering, and Institute of Chemical Process, Seoul National University, Seoul 08826, Republic of Korea

d Advanced Institute of Convergence Technology, Seoul National University, Suwon 16229, Republic of Korea

† Electronic supplementary information (ESI) available. See DOI: https://doi.org/10.1039/d4im00163j

1 Introduction

Global carbon dioxide (CO_2) emissions from fossil fuels were expected to reach 37.4 billion tons in 2024, reflecting a 0.8% increase compared to the previous year, according to recent data from the Global Carbon Project.[1] This trend runs counter to global efforts to move toward a carbon-neutral society, highlighting the urgent need to reduce fossil fuel consumption and develop alternative clean energy technologies. Among these, hydrogen (H_2) emerges as a

Jiwoo Lee is currently a PhD candidate under the supervision of Prof. Ho Won Jang at the Department of Materials Science and Engineering of Seoul National University (SNU). She received her BS degree in Materials Science and Engineering from Korea University in 2022. Her current research focuses on the design of metal-based catalysts and their application to the ammonia oxidation reaction.

Jiwoo Lee

Sol A Lee received her PhD degree from the Department of Materials Science and Engineering of Seoul National University in 2021 under the supervision of Prof. Ho Won Jang. She is currently a postdoctoral associate at the California Institute of Technology under the supervision of Prof. Harry Atwater. Her current research focuses on synthesizing electrocatalysts and semiconductors for energy conversion and designing unassisted tandem devices.
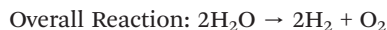
Sol A Lee

critical resource for the transition to sustainable energy due to its ability to produce zero carbon dioxide (CO₂) upon combustion.² Hydrogen has a high energy density (140 MJ kg⁻¹), which is significantly higher than that of conventional solid fuels (50 MJ kg⁻¹).³ Moreover, hydrogen plays a key role in addressing the challenges of intermittent renewable energy supply, such as from solar and wind sources.⁴,⁵ By converting excess electricity into hydrogen and storing it, hydrogen offers a viable solution for energy storage and transportation. To fully realize this potential, it is crucial to produce hydrogen in a manner that does not emit carbon. Water electrolysis, a process that splits water (H₂O) into hydrogen and oxygen (O₂) using electricity, is the key technology for producing green hydrogen without carbon emissions.⁶,⁷ For this reason, water electrolysis is gaining increasing attention as a key technology for both energy transition and the realization of a sustainable society.

The water electrolysis process consists of the following two half-cell reactions:

Hydrogen Evolution Reaction (HER): 4H⁺ + 4e⁻ → 2H₂

Oxygen Evolution Reaction (OER): 2H₂O → O₂ + 4H⁺ + 4e⁻
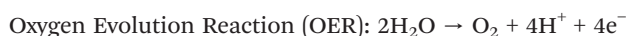
The overall reaction for water electrolysis is as follows:

Overall Reaction: 2H₂O → 2H₂ + O₂

Despite its great potential to produce clean hydrogen, water electrolysis still faces several challenges that must be addressed. While the HER is relatively simple, involving the transfer of only two electrons, the OER is far more complex, requiring the transfer of four electrons.⁸ The OER proceeds through a sequence of reaction intermediates: *OH → *O →

*OOH → *O₂. According to Man et al., the free energies required for the formation of these intermediates are theoretically the same, at 1.23 eV under ideal conditions.⁹ However, the *OH → *O and *O → *OOH transition steps require higher free energies in real systems. This results in the generation of an overpotential, requiring a higher applied potential to drive the reaction forward. Although significant efforts have been made to develop OER electrocatalysts with low overpotentials, current water electrolysis systems still face limitations in their efficiency for H₂ production. One challenge is that O₂ and H₂ are produced simultaneously during the HER and OER processes, requiring complex systems for efficient gas separation and storage.¹⁰ In addition, O₂ has limited economic value, underscoring the need for research aimed at producing value-added products at low potential.¹¹
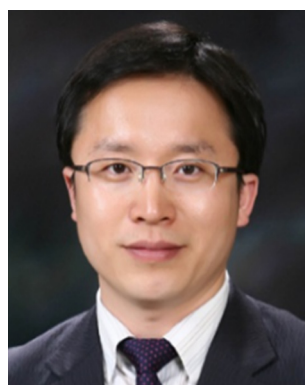
To address these limitations, chemical-assisted water electrolysis is emerging as a promising alternative to conventional water electrolysis.¹² This approach replaces the anodic OER with alternative oxidation reactions that can occur at a lower voltage, thereby reducing the overall system voltage and improving energy efficiency. Various oxidation reactions, including the alcohol oxidation reaction, ammonia oxidation reaction, urea oxidation reaction, hydrazine oxidation reaction, and biomass oxidation reaction, can be employed at the anode in chemical-assisted water electrolysis.¹³⁻¹⁷ Fig. 1 illustrates the thermodynamic potentials of several chemical-assisted water electrolysis reactions. These reactions can be operated at lower voltages while generating high-value products or removing pollutants, depending on the operating conditions.¹⁸,¹⁹ This allows for both environmental improvement and energy generation. However, chemical-assisted water electrolysis faces challenges, including high overpotential, which arise from several reasons. To deal with the challenges and reduce the voltage for hydrogen generation, various strategies are being

Tae Hyung Lee received his PhD degree from the Department of Materials Science and Engineering of Seoul National University in 2021 under the supervision of Prof. Ho Won Jang. He is currently a postdoctoral associate at the Seoul National University under the supervision of Prof. Jungwon Park. His current research focuses on fabricating electrochemical catalysts for various energy conversion systems and their theoretical investigation through simulations.

Tae Hyung Lee

Ho Won Jang is a full professor at the Department of Materials Science and Engineering, Seoul National University. He received his PhD degree from the Department of Materials Science and Engineering, Pohang University of Science and Technology in 2004. He worked as a research associate at the University of Madison-Wisconsin from 2006 to 2009. He worked at the Institute of Science and Technology of Korea as a senior research scientist before joining Seoul National University. His research interests include the design of materials and device fabrication for (photo)electrocatalysis, thin film transistors, memristors, chemical sensors, and micro-light-emitting diodes.
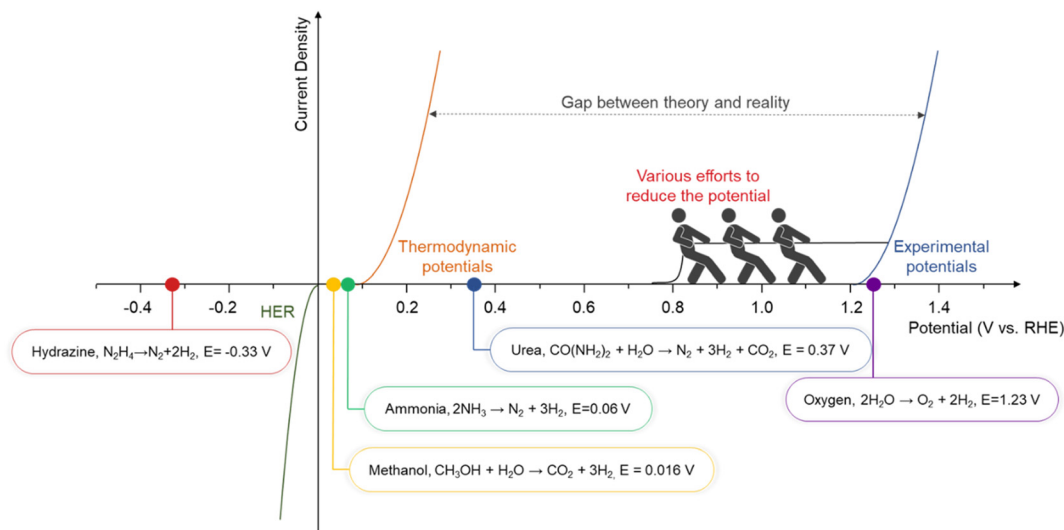
Ho Won Jang

Fig. 1 The gap between theoretical potential and practical application in various types of chemical-assisted water electrolysis.

explored, such as facet engineering, nanostructuring, alloying, doping, and computational prediction.[20–24]
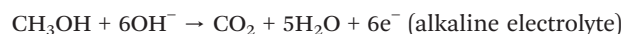
In this review, we examine various chemical-assisted water electrolysis systems—alcohol oxidation, ammonia oxidation, urea oxidation, hydrazine oxidation, and biomass oxidation—that enable hydrogen production at low voltages. As previously mentioned, the HER is relatively simple, and its overpotential does not vary significantly with the presence or absence of additives.[25–27] Therefore, in this review, we primarily focus on anodic reactions, as they are critical in determining the overall energy efficiency and performance of chemical-assisted water electrolysis systems. Additionally, we explore the latest research trends in catalyst design and reaction mechanisms, focusing on the strategies to reduce the system voltage. Finally, we address the main challenges that chemical-assisted water electrolysis must overcome and provide insights into future prospects.

2 Strategies to reduce the overpotential of hybrid water electrolysis

2.1 Alcohol oxidation reaction

2.1.1 Methanol oxidation reaction. Direct alcohol fuel cells (DAFCs), which oxidize alcohol fuels to produce electricity, are emerging as a clean chemical energy conversion technology.[28,29] Alcohol fuels offer several advantages, including safety, low cost, and high energy density. However, achieving high efficiency and performance in DAFCs requires significant improvements in catalyst performance at the anode, where alcohol electrooxidation occurs.[14,30] In this section, we will briefly introduce the alcohol oxidation reactions of methanol (a C1 alcohol) and ethanol (a C2 alcohol)—the primary feedstocks used in DAFCs—and discuss various catalyst studies aimed at reducing the reaction overpotential.

Methanol (CH_3OH), as the simplest alcohol, has been extensively studied. In the methanol oxidation reaction (MOR), six electrons are involved in the complete oxidation of methanol to CO_2. The thermodynamic potential of this process is 0.016 V, which is notably lower than that of the OER.[31,32] The methanol oxidation reaction at the anode proceeds as follows:

$$CH_3OH + H_2O \rightarrow CO_2 + 6H^+ + 6e^- \text{ (acidic electrolyte)}$$

$$CH_3OH + 6OH^- \rightarrow CO_2 + 5H_2O + 6e^- \text{ (alkaline electrolyte)}$$

The MOR can occur under acidic, neutral, and alkaline conditions. A study by Mekazni *et al.* showed that the MOR only proceeds in the presence of adsorbed OH.[33] The adsorbed OH breaks the O–H bonds in methanol and promotes its oxidation. Density functional theory (DFT) calculations confirmed that the simultaneous adsorption of OH and methanol reduces the activation energy for methanol dehydrogenation. If methanol is not fully oxidized during the reaction, additional products such as formaldehyde and formate are formed, both of which are high-value compounds. Formaldehyde is widely used in industry as a crosslinking agent in paints, resins, and polymers. Formate, an essential chemical for the textile, rubber, and pharmaceutical industries, has a significantly higher market value (1300$ per ton) compared to methanol (350$ per ton).[11,34,35]

The MOR can proceed *via* two distinct pathways: the direct pathway and the indirect pathway, which differ in the formation of CO intermediates.[31,36] In the direct pathway, methanol adsorbs on the catalyst, is gradually oxidized, and is eventually converted to CO_2. In the indirect pathway, methanol adsorbs onto the catalyst surface, and its C–H bonds are sequentially broken to form $COH_{x,ads}$ intermediates and, finally, CO_{ads}. However, strongly adsorbed

CO$_{ads}$ species can deactivate the catalyst, resulting in a reduction in catalytic activity.

Platinum (Pt) is widely recognized as the most effective catalyst for the MOR. However, its application is hindered by slow reaction kinetics, which require an overpotential exceeding 0.4 V.[37] This sluggish behavior is attributed to the complexity of the reaction mechanism, which involves a six-electron transfer. Furthermore, platinum is highly susceptible to poisoning by CO$_{ads}$, limiting its long-term stability.[38] To overcome these challenges, researchers have actively pursued the development and synthesis of advanced catalysts, employing various strategies to mitigate CO poisoning and enhance the performance of Pt-based electrocatalysts at low overpotentials.

Kim *et al.* proposed a single-atom-to-cluster (SAC) approach to form a monolayer of single Pt atoms on the surface of thiolated multiwalled carbon nanotubes (S-MWNTs) and then controlled the cluster size by heat treatment followed by slow quenching (q).[39] Fig. 2a shows that the Pt cluster size varies with the heat treatment temperature (T_h), and the particle size becomes larger and the size distribution becomes wider as T_h increases. *In situ* X-ray diffraction (XRD) analysis proves that increasing T_h enhances the crystallinity and enlarges the cluster size. In addition, the cyclic voltammetry (CV) patterns of Pt$_{h-q}$/MWNTs processed at different T_h, shown in Fig. 2b, show that the onset potential of Pt$_{h-q}$/MWNTs decreases with smaller cluster size. This onset potential downshift is because the quantum-size effect becomes more pronounced

as the Pt cluster size decreases, which leads to an increase in s–d mixing. X-ray absorption fine structure (EXAFS) and near edge structure (XANES) were used to quantitatively confirm the cluster size and electronic structure changes, and it was observed that the Pt–Pt bonding peak becomes more pronounced with increasing T_h, and the electronic structure approaches the bulk state. These results demonstrate the transition of Pt from single atoms to clusters. Similarly, Chen *et al.* demonstrated the size effect of Pt-on-Au core–satellite nanocomposites by controlling the size of Pt particles from 2.1 to 7.6 nm using a seed-mediated growth method.[40] Pt nanoparticles as small as 2.1 nm exhibited outstanding performance in the MOR, with a higher j_f/j_b ratio, indicating improved CO tolerance. This superior CO tolerance resulted in better long-term stability compared to nanocomposites with larger Pt nanoparticles.

In addition to particle size control, introducing other metals has become a key strategy in enhancing the performance of MOR catalysts. Ruan *et al.* proposed a novel approach by introducing Co single atoms on nitrogen-doped carbon (N–C) supports, followed by anchoring them to Pt nanoparticles.[41] As shown in Fig. 2c, the Co single atoms modify the electronic structure of Pt by redistributing electrons on the support, thereby optimizing the activity of Pt nanoparticles. One of the significant contributions of Co single atoms is their oxophilic property, which promotes OH$^-$ adsorption and facilitates the oxidation of CO$_{ads}$ intermediates at the Pt active center. Fig. 2d shows the mass activity of Co-N–C-x/Pt in 1 M KOH with 3 M methanol,
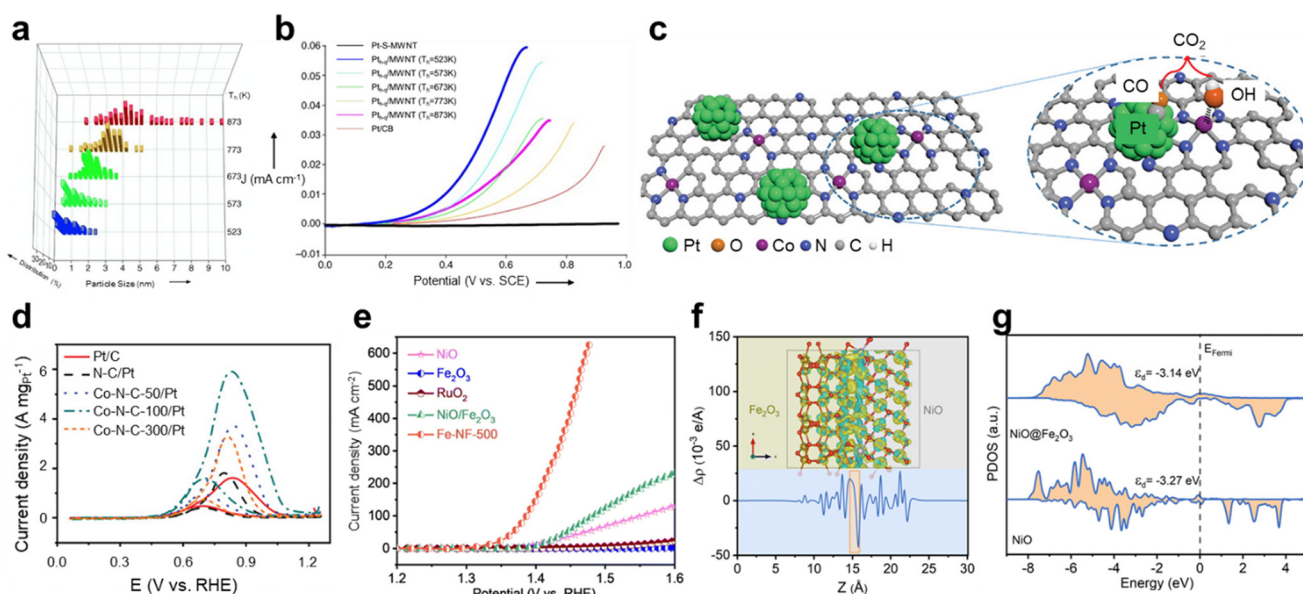

Fig. 2 Methanol oxidation reaction (MOR). (a) Size distribution of Pt$_{h-q}$/MWNTs treated at various heating temperatures. (b) MOR CV graph of Pt-S-MWNTs and Pt$_{h-q}$/MWNTs treated at various heating temperatures and of Pt/CB in 0.5 M H$_2$SO$_4$ with 2 M CH$_3$OH. (a and b) Adapted with permission.[39] Copyright 2006, WILEY-VCH. (c) Scheme of the synergistic catalytic process between Co single atoms and adjacent Pt sites. (d) MOR LSV curves of Pt/C, N–C/Pt, and Co–N–C-x/Pt (x = 50, 100, and 300) in 1 M KOH with 3 M CH$_3$OH. (c and d) Adapted with permission.[41] Copyright 2022, Wiley-VCH GmbH. (e) MOR LSV curves of NiO, Fe$_2$O$_3$, RuO$_2$, NiO/Fe$_2$O$_3$ mixture and Fe-NF-500 in 1 M KOH with 1 M CH$_3$OH. (f) Charge density distribution of the Fe$_2$O$_3$/NiO heterojunction and plane-average electron difference diagram. (g) PDOS calculated for NiO and Fe$_2$O$_3$/NiO. (e–g) Adapted with permission.[42] Copyright 2023, The Royal Society of Chemistry.

showing that the Co–N–C/Pt sample exhibited higher current density than N–C/Pt (1.8 A mg_{Pt}^{-1}) and commercial Pt/C (1.6 A mg_{Pt}^{-1}). Notably, Co–N–C-100/Pt reached a current density of about 6 A mg_{Pt}^{-1} and had a low onset potential. The effectiveness of the Co single atoms was demonstrated by CO-stripping measurements. The onset potential of the CO oxidation peak of Co–N–C-x/Pt was lower than that of N–C/Pt and commercial Pt/C, indicating that a smaller driving force is required to remove CO_{ads} intermediates from the Pt surface. This indicates that the Co single atoms greatly enhance the CO tolerance of the Pt active sites. In addition, in the durability test, Co–N–C/Pt retained 60% of its initial current density after 4000 seconds, compared to only 25% for commercial Pt/C, demonstrating outstanding stability. Kuang et al. synthesized Pt/N-MoSe$_2$@MHCS by applying N-doping and interfacial engineering to MoSe$_2$ supported on mesoporous carbon spheres.[43] N-doping with NH$_3$ plasma enhanced the interaction between the support and Pt nanoparticles, leading to uniform dispersion. When Pt/N-MoSe$_2$@MHCS is used as both an anode and a cathode in a two-electrode system, only 0.60 V is required to generate a current density of 10 mA cm^{-2} in 0.5 M H$_2$SO$_4$ with 1 M methanol. This is 1.07 V lower than that required for conventional water electrolysis, demonstrating that H$_2$ production can be achieved with significantly lower energy input. Similarly, Zhou et al. synthesized Pt nanoparticles supported on CoSe/N-doped carbon nanospheres (Pt-CoSe/NCs) and utilized them as MOR catalysts, achieving a peak current density of 84.2 mA cm^{-2} in 0.5 M H$_2$SO$_4$ and 1 M methanol, a 3.1-fold increase over Pt/C.[44] Pt-CoSe/NCs exhibited a low overpotential and high stability over 1000 cycles for HER performance. DFT calculations confirmed that CoSe/NCs enhanced the charge density of Pt, optimizing the H and CO adsorption energies. In the two-electrode system, Pt/C‖Pt/C required 0.84 V to achieve 10 mA cm^{-2}, whereas Pt-CoSe/NC-800‖Pt-CoSe/NC-800 required only 0.67 V. Zhang et al. synthesized Pt–Ln/C catalysts (Ln = La, Ce, Pr, Nd) and explored how lanthanide elements induce electronic perturbations that influence catalytic activity.[45] Alloying Pt with a Ln element modulates the electronic structure of Pt, significantly affecting CO adsorption and poisoning. DFT calculations revealed that the d–f bonding effect of Ce optimizes the d-band centers of Pt. This adjustment weakens the binding strength of intermediates such as CO_{ads}. Furthermore, the electronic interaction between Pt and Ce redistributed the electron density on the Pt surface, increasing the energy barrier for CO formation while lowering the adsorption energy of CO_{ads}. It significantly affects the onset potential, with Pt$_5$Ce/C showing an onset potential of 0.17 V vs. RHE in 1 M KOH with 1 M methanol, which is 0.25 V lower than that of the Pt/C catalyst (0.42 V vs. RHE). These combined mechanisms inhibit the formation of CO_{ads}, mitigate poisoning effects, and significantly enhance the durability of Pt catalysts.

The alloying of multiple elements ultimately leads to the fabrication of high entropy alloys (HEAs). Li et al. successfully synthesized Pt$_{18}$Ni$_{26}$Fe$_{15}$Co$_{14}$Cu$_{27}$/C nanoparticles using a simple low-temperature oil phase synthesis method.[46] This HEA exhibited exceptional MOR performance due to its multiple active sites and fast electron transfer ability. Partial projected density of states (PDOSs) analysis revealed that the strong electronic interactions between non-noble transition metals (Ni, Fe, Co, Cu) and Pt in the HEA structure shifted the d-band center of Pt closer to the Fermi level compared to commercial Pt/C. This modification in the electronic structure efficiently lowers the reaction energy barrier and enhances the structural stability of the catalyst, resulting in significant catalytic performance improvements. This also influences the onset potential, with the Pt$_{18}$Ni$_{26}$Fe$_{15}$Co$_{14}$Cu$_{27}$/C nanoparticles exhibiting an onset potential of 412 mV vs. RHE, representing a significant 133 mV reduction compared to the commercial Pt/C catalyst. The HEA catalyst exhibited a peak mass activity of 15.04 A mg_{Pt}^{-1} and a peak area activity of 114.93 mA cm^{-2} in 1 M KOH with 1 M methanol, respectively, which were superior to those of the commercial Pt/C catalyst (1.45 A mg_{Pt}^{-1} and 27.48 mA cm^{-2}, respectively). Moreover, durability tests revealed that the Pt$_{18}$Ni$_{26}$Fe$_{15}$Co$_{14}$Cu$_{27}$/C catalyst retained 93.6% of its initial performance after 1000 cycles, demonstrating excellent stability compared to Pt/C, which showed 26.9% degradation.

Due to the problem of low stability caused by CO poisoning and the high cost of noble metals, non-noble metal-based MOR electrocatalysts, which are naturally abundant and theoretically exhibit excellent electrocatalytic activity, have recently attracted attention.[47] Li et al. converted a Ni-metal organic framework (MOF) to Ni(OH)$_2$-x through alkali treatment using different NaOH concentrations (x = 0.025, 0.25, and 0.5).[48] Among these, the Ni(OH)$_2$ treated with 0.25 M NaOH exhibited the best balance between structural stability and active sites, showing better activity compared to the other samples at both low (1.5 V vs. RHE) and high potential (1.7 V vs. RHE). Notably, at 1.5 V vs. RHE, Ni(OH)$_2$-0.25 recorded 171.8 mA cm^{-2} in 1 M KOH with 1 M methanol, exceeding the performance of Ni(OH)$_2$-0.025 and Ni(OH)$_2$-0.5 by 1.5- and 2.5-fold, respectively. The alkali treatment converted the Ni-MOF to Ni(OH)$_2$, enhancing the number of active sites and optimizing the electron transfer pathway. Furthermore, Ni(OH)$_2$ promotes the MOR more effectively by increasing the surface oxygen vacancies and Ni^{3+}/Ni^{2+} ratio, which are crucial for improving catalytic performance. The effect of oxygen vacancies (V_O) has been investigated by Yang et al. in ultrathin-NiO nanosheets prepared by controlling the calcination reaction time.[49] In 1 M KOH with 0.5 M methanol, V_O-rich NiO achieved a current density of 85.3 mA cm^{-2} at 0.7 V vs. Ag/AgCl, which is 2.3 and 3.5 times higher activity than that of V_O-poor and bulk NiO, respectively. In addition, the Tafel slope was reduced to 42 mV per decade on V_O-rich NiO, compared to 80 mV per decade on V_O-poor NiO and 111 mV per decade on bulk NiO, highlighting excellent reaction kinetics. V_O-rich NiO also maintained a stable current density of approximately 25 mA cm^{-2} at 0.5 V vs. Ag/AgCl for 30 000 s. These results indicate

© 2025 The Author(s). Co-published by the Institute of Process Engineering, Chinese Academy of Sciences and the Royal Society of Chemistry

Ind. Chem. Mater., 2025, **3**, 277–310 | **281**

that oxygen defects in VO-rich NiO play a critical role in enhancing MOR catalytic performance. Hou *et al.* synthesized Ni NPs coated with ultrathin graphitic carbon shells by pyrolysis of Ni–Zn MOFs and utilized them as bifunctional catalysts for the HER and MOR.[50] DFT calculations confirmed that the thin carbon shells optimized the electron transfer to Ni, ideally tuning the Gibbs free energy for H adsorption. Comparison of the LSV curves of the HER in 1 M KOH with and without 1 M methanol confirmed that the electrolyte does not interfere with the HER process. The two-electrode system using $Ni_1(Zn)@C$ as an anode and a cathode requires 1.63 V to achieve a current density of 10 mA cm^{-2} and shows good durability. Hao *et al.* investigated Fe_2O_3/NiO heterostructure catalysts synthesized *via* an ultrafast solution combustion strategy.[42] Fe-NF-500 quickly reached an industrial-scale current density of 600 mA cm^{-2} at a low potential of 1.472 V *vs.* RHE in 1 M KOH with 1 M methanol, significantly outperforming other catalysts (Fig. 2e). The onset potential of Fe-NF-500 is close to the Ni^{2+}/Ni^{3+} redox, indicating that Ni^{3+} was the actual active site in the MOR. The highly dispersed Fe–O–Ni interface promoted the electron excitation into the conduction band, improving the charge transport and diffusion ability. This accelerated the kinetics of the methanol oxidation process. DFT calculations also supported this electron transport mechanism. As shown in Fig. 2f, the plane-average electron difference diagram plotted along the direction of the heterojunction showed that electrons were transferred and accumulated from NiO to Fe_2O_3, and the NiO at the interface became electron-deficient. Additionally, the PDOS results in Fig. 2g showed that the d-band center of the Fe_2O_3/NiO heterojunction was significantly closer to the Fermi level compared to pure NiO. This shift enhances the anti-bonding state, which contributes to the strong coupling between the catalyst and methanol. Fig. 3 shows the stability time as a function of the potential applied to the MOR electrocatalyst. While noble metal-based catalysts exhibit shorter stability times, they facilitate reactions at relatively low potentials. However, non-noble metal-based catalysts operate at higher potentials, requiring more energy but demonstrating longer stability times.
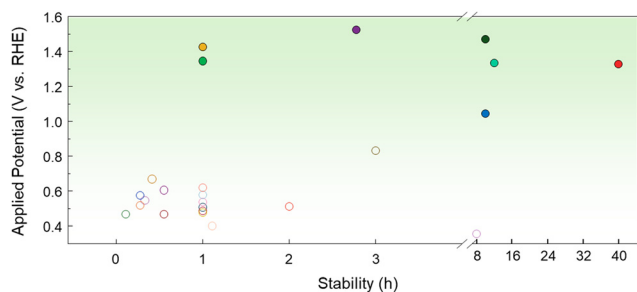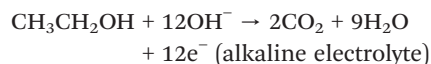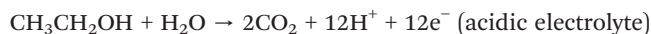

Fig. 3 Comparison of the MOR performance of various electrocatalysts. Each potential was converted to RHE, considering the reference electrode and pH of the electrolyte. The detailed values are shown in the ESI.†

2.1.2 Ethanol oxidation reaction. Unlike methanol, which is a C1 molecule, ethanol has a more complex oxidation reaction mechanism due to the presence of C–C bonds in its molecular structure. The ethanol oxidation reaction (EOR) can be categorized into the C1 pathway and C2 pathway, depending on whether the C–C bond is cleaved. In the C1 pathway, the C–C bond of ethanol is broken, resulting in the complete oxidation of ethanol to CO_2 through a 12-electron transfer process.[51,52] The reaction equations are as follows:

$$CH_3CH_2OH + H_2O \rightarrow 2CO_2 + 12H^+ + 12e^- \text{ (acidic electrolyte)}$$

$$CH_3CH_2OH + 12OH^- \rightarrow 2CO_2 + 9H_2O + 12e^- \text{ (alkaline electrolyte)}$$

However, the selectivity of the C1 pathway is low, and the overpotential is high because cleaving the C–C bond requires substantial energy. Furthermore, C–C bond cleavage produces intermediates such as CO_{ad} and $CH_{x,ads}$, which can deactivate the catalyst by strongly adsorbing onto its surface.[53] Oxidizing these intermediates requires higher potentials, reducing the overall reaction efficiency. On the other hand, the C2 pathway leaves the C–C bond intact, resulting in partial oxidation products, such as acetaldehyde (CH_3CHO) and acetic acid (CH_3COOH), which are valuable in various industries. Therefore, effective catalyst designs are necessary to remove intermediates efficiently and precisely control reaction selectivity. This is essential for activating the C1 pathway efficiently and utilizing the C2 pathway selectively.[54] In addition, catalyst properties must be optimized to lower the activation energy, enabling the reaction to proceed at lower overpotentials.

Similar to MOR catalysts, EOR catalysts also exhibit low overpotential in Pt-based materials, prompting numerous studies to enhance their efficiencies. Li *et al.* evaluated the MOR performance of Pt combined with hydroxyl-rich CeO_2 and observed that the abundant OH groups and oxygen vacancies in the support optimized the electron transfer to Pt.[55] This optimization reduced the adsorption of CO_{ads} intermediates, resulting in high catalytic activity and durability. Wang *et al.* investigated how the surface structures of Pt influence the reaction pathway and product selectivity.[56] Using transition-state (TS) searching methods and DFT calculations, they calculated the reaction barriers and adsorption energies of intermediates on Pt(111), Pt(211), and Pt(100) surfaces. Their findings revealed that Pt(100) is the most effective surface for the complete oxidation of ethanol to CO_2. This efficiency arises from its ability to promote C–C bond cleavage through strongly adsorbed intermediates such as CH_2CO or CHCO. In contrast, Pt(111) favors the formation of partial oxidation products such as CH_3CHO and CH_3-COOH, showing that the selectivity of the EOR is highly sensitive to the surface structure. Pierozynski experimentally analyzed the effect of the surface crystal structure on the EOR in alkaline media using polycrystalline Pt, Pt(111), and

Pt(100) single-crystal surfaces.[57] The experimental results showed that Pt(111) exhibited higher catalytic activity and faster kinetics than Pt(100) and polycrystalline Pt. This is attributed to the separation of the underpotential deposition (UPD) H region at low potential and the OH^- adsorption region at high potential. These distinct regions prevent competitive adsorption and allow for more efficient catalytic reactions. In contrast, on Pt(100), the overlap of the OH^- and H adsorption regions causes OH^- and H to be competitively adsorbed at the same site and reduces the catalytic reaction efficiency. The results show that Pt(111) promotes the oxidation of partial oxidation products such as CH_3CHO and CH_3COOH, while reducing the poisoning of intermediates such as CO_{ads}, which can improve the reaction performance.

Extending this, researchers are focusing on facet modification to increase EOR efficiency. Liu *et al.* proposed a lattice expansion strategy for Pd@Pt core–shell nanoparticles to enhance the EOR performance.[58] The lattice of the Pt shell was expanded by inserting H into the Pd core, thereby converting it to $PdH_{0.43}$, which optimized the electronic structure of the catalyst and significantly improved the catalytic performance. Through high-angle annular dark-field scanning transmission electron microscopy (HAADF-STEM) images and fast Fourier transform (FFT) analysis, they confirmed that the core–shell structure was not destroyed and the lattice was expanded after H insertion. Notably, the Pt–Pt spacing increased during conversion to the $PdH_{0.43}$ core, resulting in a lattice expansion of about 2.55% on the Pt(100) side. DFT calculations were conducted to determine the free energies of OH and CO adsorption on the Pt(100) and Pt(111) sides. The results demonstrated a reduction in the adsorption free energy of OH on the $PdH_{0.43}$@Pt surface, facilitating OH adsorption. This effect is particularly pronounced on the (100) facet, which exhibits stronger Pt–OH and Pt–CO bonds due to its lower coordination number. Although the adsorption free energy of CO shows little change, the enhanced OH adsorption contributes to the more effective removal of CO poisoning. Consequently, the specific activity of $PdH_{0.43}$@Pt was 14.86 A mg_{Pt}^{-1}, representing a 25.19-fold improvement over commercial Pt/C in 1 M KOH with 1 M methanol.

Alloying is a strategy used to increase the efficiency of catalysts by modifying the structural and electronic properties of Pt. Yan *et al.* synthesized Pt_3Ga-200/C catalysts by alloying Ga with Pt to improve the oxidation efficiency of the C2 pathway by tuning the electronic structure of Pt.[59] The specific activity of Pt_3Ga-200/C was 2.461 mA cm^{-2} at 0.56 V *vs.* SCE, which was more than four times higher than that of Pt/C, measured to be 0.584 mA cm^{-2} at 0.59 V *vs.* SCE in 0.1 M $HClO_4$ with 0.1 M ethanol. According to the *in situ* Fourier transform infrared reflection (FTIR) spectroscopy results in Fig. 4a, compared to Pt_3Ga-200/C, Pt/C showed a weaker CO_2 signal and a distinct CO band caused by partial acetaldehyde dissociation. In contrast, Pt_3Ga-200/C directly and continuously oxidized acetaldehyde to efficiently produce CO_2. Fig. 4b shows the CO_2 band area ratio calculated from the FTIR results, indicating that Pt_3Ga-200/C achieved much higher CO_2 selectivity than Pt/C. This highlights the critical role of Ga in enhancing catalytic efficiency. The CO stripping voltammetry results in Fig. 4c show that the Pt_3Ga/C catalysts, including Pt_3Ga-200/C, exhibit significantly better resistance to CO poisoning than Pt/C. This is attributed to the electronic modification of Ga, which reduces
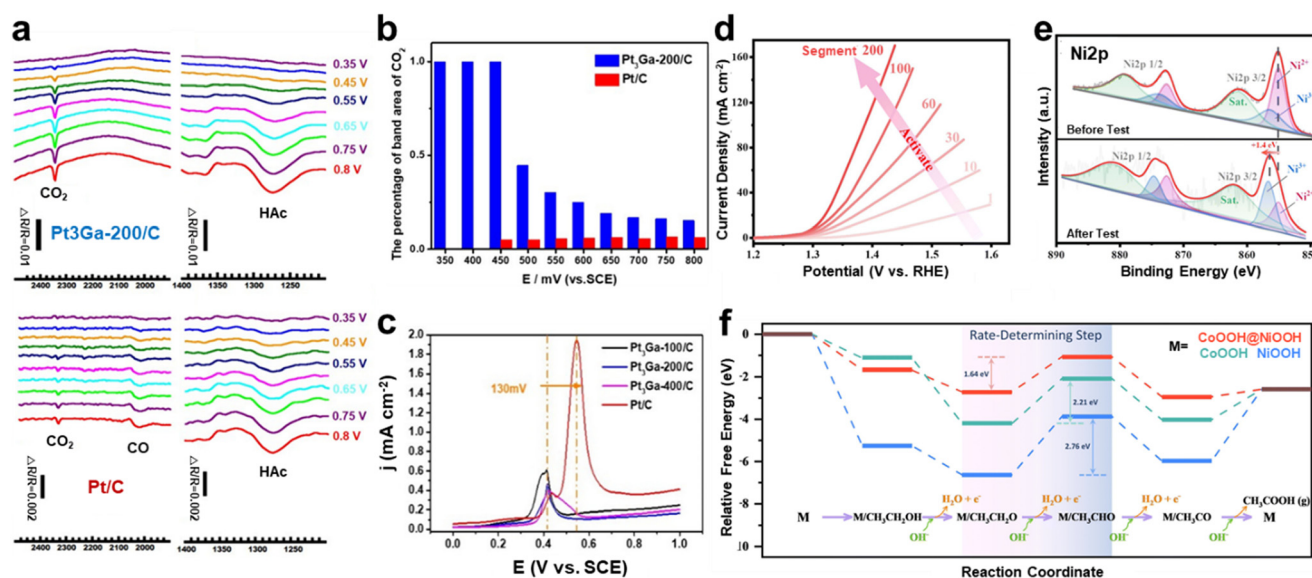

Fig. 4 Ethanol oxidation reaction (EOR). (a) *In situ* MSFTIR spectra of Pt_3Ga-200/C and Pt/C for CO_2 and HAc during the EOR. (b) The percentage of band area of CO_2 ($S_{CO_2}/(S_{CO_2} + S_{HAc})$). (c) CO-stripping voltammetry of catalysts in 0.1 M $HClO_4$. (a–c) Adapted with permission.[59] Copyright 2023, American Chemical Society. (d) LSV activation curve of Co(OH)$_2$@Ni(OH)$_2$. (e) Ni 2p XPS spectra before and after electrochemical activation. (f) EOR free energy diagram for CoOOH, NiOOH and CoOOH@NiOOH based on DFT calculations. (d–f) Adapted with permission.[61] Copyright 2023, The Royal Society of Chemistry.

© 2025 The Author(s). Co-published by the Institute of Process Engineering, Chinese Academy of Sciences and the Royal Society of Chemistry

*Ind. Chem. Mater.*, 2025, **3**, 277–310 | **283**

CO adsorption and promotes the rapid oxidation of CO. This effect arises from the shift of the d-band center of Pt atoms, which decreases CO adsorption, and the high hydrophilicity of the Ga surface facilitates the generation of more *O or *OH species, promoting CO oxidation at Pt sites. Wang et al. enhanced the EOR performance by incorporating monodispersed Ga atoms into Pt_3Mn nanocrystals, forming Ga–O–Pt interfaces.[60] The Ga–O–Pt_3Mn nanocatalyst achieved a high activity of 4.71 mA cm^{-2} at 0.7 V vs. RHE in 0.1 M $HClO_4$ with 0.5 M ethanol, outperforming Pt_3Mn and commercial Pt/C by 3.68 and 8.41 fold, respectively. In situ FTIR spectroscopy revealed that CO_2 generation occurred at 0.54 V vs. RHE on Ga–O–Pt_3Mn, significantly lower than the 0.74 V vs. RHE required for Pt_3Mn, demonstrating the inhibition of toxic CO intermediate formation. This result is consistent with the C1/C2 product ratio, indicating that Ga–O–Pt_3Mn promotes C–C decomposition and follows a complete oxidation pathway. DFT calculations further confirmed that p–d orbital hybridization at the catalytic interface reduces both the intermediate formation and reaction energy barriers, facilitating efficient C–C bond cleavage. These results demonstrate that Ga doping enables effective ethanol oxidation at low potentials.

In recent decades, significant efforts have been made to enhance the catalytic activity of Ni-based EOR catalysts through the rational design of active surfaces and interfaces.[62] These improvements have been achieved by manipulating factors such as the atomic arrangement, electronic structure, and the incorporation of dopant elements.[12] Chi et al. synthesized 2D MOF1-CDs@CC by combining a Ni-MOF with carbon dots (CDs) through a solvothermal method.[63] The CDs enhanced the conductivity of the MOF, improving charge transfer efficiency and promoting ethanol adsorption. In 1 M KOH with 1 M ethanol, the optimized MOF1-CDs@CC demonstrated a high current density of 119 mA cm^{-2} at 1.6 V, with a significantly accelerated EOR onset compared to MOF1. This improvement is attributed to the increased surface area and high stability provided by the CDs, emphasizing the critical role of the support in catalytic performance. Metal doping can modify the electronic structure to increase catalytic activity. Wang et al. synthesized Cu-doped NiOOH by electrochemical reconstruction of a NiCu alloy.[64] X-ray photoelectron spectroscopy (XPS) analysis revealed that the Ni^{3+}/Ni^{2+} ratio in Cu-doped NiOOH is 72%, approximately twice that of NiOOH. This indicates that Cu doping increases the proportion of high-valence Ni species, which enhances the conductivity of NiOOH and facilitates higher charge transfer rates. In situ electrochemical Raman spectroscopy confirmed the production of acetaldehyde and acetate at different potentials during the EOR. However, ^{1}H nuclear magnetic resonance (NMR) analysis detected no acetaldehyde signals, suggesting that acetaldehyde serves as a possible intermediate, subsequently converting to acetate during the EOR process. The Cu-doped NiOOH exhibited excellent stability, maintaining 73% of its initial current density for 32 hours at 1.7 V vs. RHE in 1 M KOH with 1 M ethanol. Li et al. synthesized a $Co(OH)_2$@$Ni(OH)_2$ heterostructure with a large specific surface area by a one-pot hydrothermal process

using a Ni-doped ZIF-67 precursor.[61] The in situ electrochemical activation process, as shown in Fig. 4d, demonstrated an enhancement in the EOR catalytic performance. XPS analysis in Fig. 4e revealed that the Ni 2p peak shifted by 1.4 eV to a higher binding energy after activation. In addition, an increase in Ni^{3+} species was observed, providing evidence for the conversion of $Ni(OH)_2$ to NiOOH. The $Co(OH)_2$@$Ni(OH)_2$ heterostructure showed superior performance in terms of current density and stability compared to pure $Ni(OH)_2$ and $Co(OH)_2$ catalysts. In 1 M KOH with 1 M ethanol, the catalyst required a potential of 1.301 V vs. RHE to achieve a current density of 10 mA cm^{-2}, which is 92 mV lower than that of $Ni(OH)_2$. It also demonstrated excellent long-term stability, maintaining performance for over 100 hours at 50 mA cm^{-2}. After the 20 h stability test, ^{1}H NMR analysis showed a decrease in the ethanol signal and an increase in the acetic acid signal. Faradaic efficiency (FE) calculations confirmed a high potassium acetate selectivity of 97.9% up to 100 h, indicating improved reaction efficiency. Based on these results, the four-electron EOR pathway of *CH_3-CH_2OH → *CH_3CH_2O → *CH_3CHO → *CH_3CO → *CH_3COOH was proposed (Fig. 4f). During the EOR process, the second dehydrogenation step from *CH_3CH_2O to *CH_3CHO was identified as the rate-determining step. The energy barrier for this step in CoOOH@NiOOH was 1.64 eV, which was significantly lower than that of CoOOH (2.21 eV) and NiOOH (2.76 eV). Furthermore, *CH_3CHO was identified as the most unfavorable intermediate during the EOR process, theoretically explaining why the main product is acetic acid rather than acetaldehyde. Specifically, in the Pt/C||$Co(OH)_2$@$Ni(OH)_2$ two-electrode system, when methanol is added to 1 M KOH, 1.464 V is required to achieve 100 mA cm^{-2}. This is a 200 mV decrease from the typical water splitting value.

2.2 Ammonia oxidation reaction

Ammonia (NH_3) has high potential as an H_2 carrier due to its high hydrogen storage capacity of 17.6 wt%. Unlike conventional hydrogen storage technologies, ammonia is easier and safer to handle, as it exists as a liquid at room temperature and pressure, making storage and transportation more practical.[65,66] The ammonia oxidation reaction (AOR) is the reverse reaction of the Haber–Bosch process. It requires a low thermodynamic potential of 0.06 V, which reduces energy consumption by approximately 95% compared to the OER. Unlike methanol and ethanol oxidation reactions, which produce CO_2, the ammonia oxidation reaction produces N_2, a pollution-free substance.[67,68] The production of N_2 at the anode in an alkaline electrolyte proceeds as follows;

$$2NH_3 + 6OH^- \rightarrow N_2 + 6H_2O + 6e^-$$
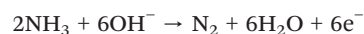
As the applied potential increases, the supply of OH^- also increases, leading to the formation of nitrite and nitrate.[69] The reaction equations for these conversions are:

$$2NH_3 + 7OH^- \rightarrow NO_2^- + 5H_2O + 6e^-$$

$$2NH_3 + 9OH^- \rightarrow NO_3^- + 6H_2O + 6e^-$$

These reactions have significant implications for wastewater treatment, contributing to reducing NH_3 toxicity. In addition, nitrate is an essential compound in the fertilizer industry, while nitrite has a variety of applications such as the manufacture of pharmaceuticals and herbicides.[70]

The AOR involves the breaking of the N–H bond in the ammonia molecule and the release of N_2 gas. Two primary mechanisms have been proposed for the AOR: the Oswin–Salomon mechanism and the Gerischer–Mauerer mechanism. In the Oswin–Salomon mechanism, NH_3 undergoes dehydrogenation, sequentially producing *NH_2, *NH, and *N intermediates, which then combine to form N_2.[71] In the Gerischer–Mauerer mechanism, NH_3 is deprotonated to form an *NH_x intermediate. The *NH_x and *NH_y intermediates subsequently combine to form a dimer (*N_2H_{x+y}), which is converted to N_2 through successive deprotonation steps.[72] However, this process produces N_{ads}, which can accumulate on the catalyst surface, leading to catalyst deactivation. The adsorption and desorption of these intermediates result in a relatively higher overpotential and limited durability. Therefore, catalysts that exhibit high performance and selectivity at low overpotentials, while maintaining stability, are critical for the ammonia oxidation reaction.[73] To address these challenges, researchers are optimizing catalyst surface properties and electronic structure through various material design strategies.

2.2.1 Noble metal-based AOR electrocatalysts. Among the single metals, Pt catalysts show intermediate N_{ads} adsorption energy, which leads to high catalytic activity and excellent N_2 selectivity. Pt selectively generates N_2 at potentials below 0.8 V, preventing the generation of oxygen-containing products such as N_2O and NO.[74] The reactivity of Pt is strongly influenced by the structure of the catalyst. Pt(100) shows an obvious oxidation peak, while little reaction is observed on Pt(111) and Pt(110), confirming the selective reactivity of Pt(100). In addition, the reactivity depends on the terrace size, and the ammonia oxidation peak potential shifts to more positive values as the terrace width decreases. Modifying the morphology of Pt also affects the catalytic activity and overpotential. Yang *et al.* used chronopotentiometry (CP) and CV electrodeposition methods to vary the structure of Pt electrodes on Ni foam.[75] The CP method synthesized dense and circular Pt particles, while the CV method formed smaller and flower-like Pt structures. This is due to the alternating oxidation–reduction reactions during the CV process, especially because the H_2 generated on the Ni foam during the reductive scan affects the deposition process. As the number of CV cycles increased, the number of active sites on the catalyst increased, which improved the AOR performance. To compare the AOR activity according to the Pt morphology, the AOR CV was measured in 5 M KOH with 1 M ammonia at 60 °C. The results showed that 500 CV-Pt exhibited an approximately 3-fold increase in peak current density compared to CP-Pt due to its large specific surface

area, and the onset potential was also shifted in the negative direction. Liu *et al.* synthesized coral-like Pt nanowires using a phytantriol liquid crystal template-assisted electrodeposition method.[76] These unique 3D coral-like nanowires maximized the benefits of nanowires by avoiding stacking and provided a large surface area favorable for enhanced mass transport through multiple nanopores. The nanopores contained a high density of atomic defects, such as edges, steps, and kinks, which greatly enhanced the catalytic activity. As a result, the coral-like Pt nanowires achieved a mass activity of 72.0 mA mg^{-1} in 1 M KOH with 0.05 M $(NH_4)_2SO_4$, approximately three times higher than that of commercial Pt/C. In addition, the unique 1D morphology improved the stability by inhibiting the dissolution commonly observed in spherical nanoparticles. After 100 cycles, the nanowires retained 85.6% of their initial peak current density, compared to 74.8% for commercial Pt/C, demonstrating better stability. These studies show that the morphology of the electrocatalyst is an important factor for the AOR performance.

Introducing other metals on Pt modifies the AOR performance by improving dehydrogenation ability, minimizing catalyst poisoning caused by N_{ads} intermediates, lowering the onset potential, and modulating energy barriers.[77,78] Pillai *et al.* utilized graph neural networks (GNNs) to predict catalytic activity, stability, and catalyst synthesizability descriptors, and then synthesized Pt_3Ru–M (M: Fe, Co, Ni) alloy nanoparticles on reduced graphene oxide (rGO) and experimentally validated their catalytic performance.[79] The onset potential of $Pt_3Ru_{1/2}$-$Co_{1/2}$ in 1 M KOH with 0.1 M ammonia is 0.42 V *vs.* RHE, which is much smaller than that of pure Pt (0.48 V *vs.* RHE) and Pt_3Ru (0.46 V *vs.* RHE). In addition, the peak mass current activity of $Pt_3Ru_{1/2}Co_{1/2}$ is 174.0 A g$_{Pt}^{-1}$, which is more than two times larger than the 78.6 A g$_{Pt}^{-1}$ and 80.2 A g$_{Pt}^{-1}$ of pure Pt and Pt_3-Ru, respectively. The onset potential was observed to decrease as the electrolyte temperature increased from 25 °C to 80 °C, demonstrating that temperature affects the AOR performance. Ru and Co optimize the site by adjusting the electron density on the Pt surface. In particular, Co interacts with Pt–Ru to adjust the antibonding orbital to improve the electronic structure. Moreover, the introduction of Co slightly decreases the N_{2p} orbital resonance energy of the adsorbate, weakening the adsorption strength to an appropriate level. This adjustment allows $Pt_3Ru_{1/2}Co_{1/2}$ to exhibit optimal adsorption properties and show increased catalytic performance. Liu *et al.* improved the AOR performance by activating the inactive (220) facet of a PtMo alloy through single-atom Ni doping.[80] Depending on the Ni doping ratio, $Pt_{93}Mo_7$, Ni_7-$Pt_{86}Mo_7$, and Ni_{22}-$Pt_{71}Mo_7$ catalysts were fabricated. Fig. 5a illustrates the onset potential and mass activity of each catalyst in 1 M KOH with 0.1 M ammonia. The onset potential of Ni_7-$Pt_{86}Mo_7$ was measured to be 0.49 V *vs.* RHE, which is not significantly different from the control. However, Ni_7-$Pt_{86}Mo_7$ achieved a peak current density of 94.96 A g^{-1}, which is significantly higher than that of $Pt_{93}Mo_7$ (58.83 A g^{-1}) and PtIr/C (20.31 A g^{-1}). Fig. 5b presents the results of calculating the limiting potentials at the main crystal facets

© 2025 The Author(s). Co-published by the Institute of Process Engineering, Chinese Academy of Sciences and the Royal Society of Chemistry

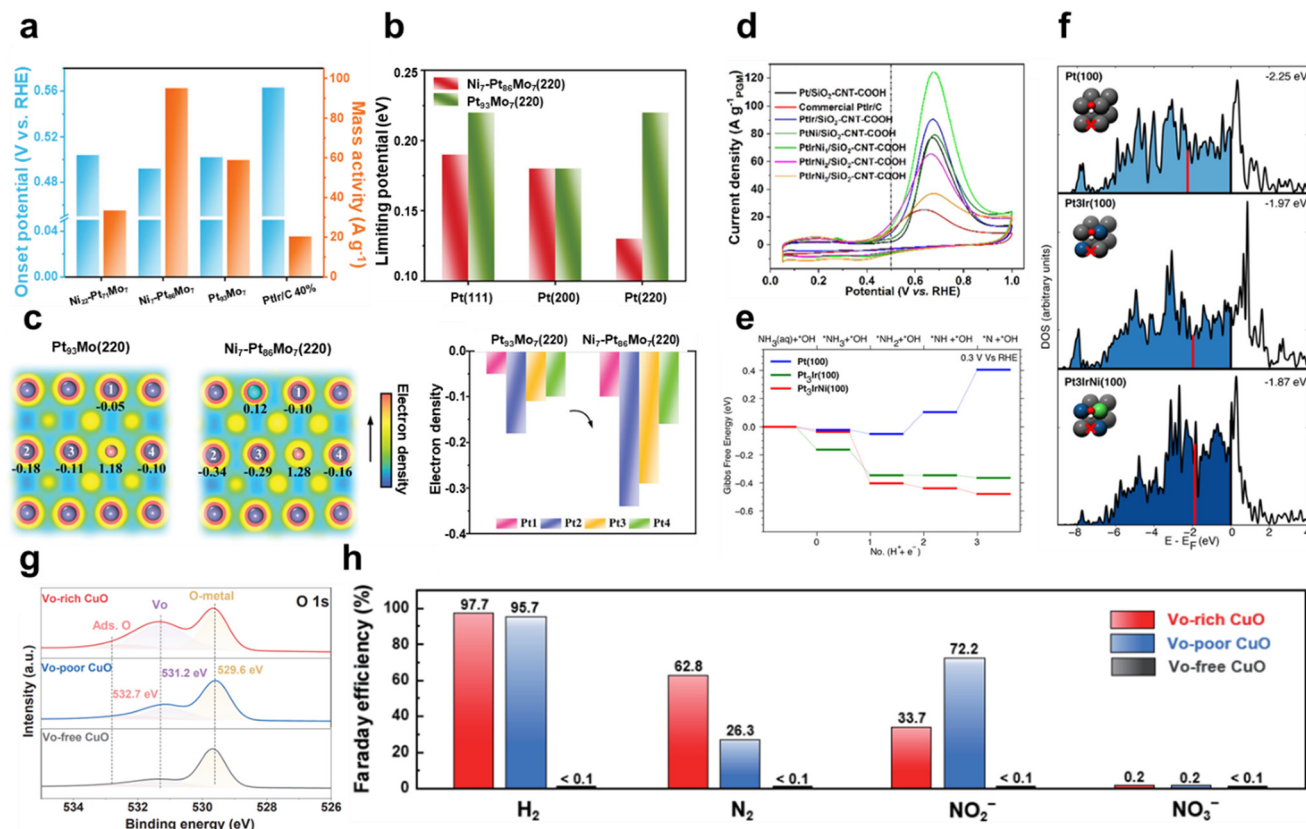*Ind. Chem. Mater.*, 2025, **3**, 277–310 | **285**

Fig. 5 Ammonia oxidation reaction (AOR). (a) Comparison of onset potentials and mass activities for different Pt alloy catalysts in 1 M KOH with 0.1 M NH_3. (b) Limiting potential of different facets in Ni_7-$Pt_{86}Mo_7$ and $Pt_{93}Mo_7$. (c) Electron density contour map and electron densities of specific Pt atoms on the (220) facet of Ni_7-$Pt_{86}Mo_7$ and $Pt_{93}Mo_7$. (a–c) Adapted with permission.[80] Copyright 2023, Wiley-VCH GmbH. (d) CV curves for different Pt catalysts in 1 M KOH with 0.1 M NH_3. (e) Gibbs free-energy pathway for the AOR through DFT calculations on Pt(100), Pt_3Ir(100), and Pt_3IrNi(100) at 0.3 V vs. RHE. (f) Group d-orbital density of states. Red lines indicate the d-band center. (d–f) Adapted with permission.[81] Copyright 2020, American Chemical Society. (g) O 1s XPS spectra of V_O-free, V_O-poor and V_O-rich CuO. (h) Faradaic efficiency of H_2, N_2, NO_2^- and NO_3^- for V_O-free, V_O-poor and V_O-rich CuO at 0.6 V vs. Hg/HgO. (g and h) Adapted with permission.[82] Copyright 2022, Springer Nature.

(111), (200), and (220) in the $Pt_{93}Mo_7$ and Ni_7-$Pt_{86}Mo_7$ models. Unlike the Pt(200) facet, which is naturally the highest AOR active facet, the Pt(220) facet is generally considered an inactive face and has a high energy barrier of 0.22 eV, resulting in a low AOR contribution. However, Ni doping effectively reduces the energy barrier of the (220) facet to 0.13 eV, which is lower than that of the (200) facet. This finding indicates that the (220) facet has been successfully activated thanks to Ni doping. The electron density contour in Fig. 5c demonstrates that doping Ni on the (220) facet causes an obvious electron accumulation around the Pt atoms, resulting in a significant increase in electron density. This supports that Ni doping awakened the inactive facet and modified it into the most active surface.

In particular, the introduction of Ir lowers the onset potential by enhancing ammonia adsorption and promotes the dehydrogenation process.[83] In Pt–Ir alloys, Ir facilitates the adsorption of *N and *NH species, making the vacant sites on Pt available to accept additional intermediates such as *NH_2. Lin et al. introduced a unique PtIrCu AOR catalyst with hyperbranched concave octahedral nanodendrites (HCONDs).[84] In 1 M KOH with 0.1 M ammonia, PtIrCu HCONDs exhibited an onset potential of 0.35 V vs. RHE,

which was much lower than that of PtIr nanocubes (0.43 V vs. RHE), PtCu nanocubes (0.50 V vs. RHE), and commercial Pt/C (0.51 V vs. RHE). The peak current density also showed a notable difference, with PtIrCu HCONDs achieving 122.9 A g_{PGM}^{-1}, more than twice that of commercial Pt/C. PtIrCu HCONDs featured high-index facets such as (553), (331), and (221), providing a high density of active sites and enhancing the interaction with reactants. Furthermore, Cu and Ir atoms partially substitute Pt atoms, inducing a compressive strain of the lattice that weakens the oxygen adsorption and promotes the intermediate desorption. These properties lower the dehydrogenation potential and further accelerate the reaction kinetics, enhancing the AOR activity of PtIrCu HCONDs. Li et al. synthesized PtIrNi alloy nanoparticles on porous silicon dioxide (SiO_2) and carboxyl-functionalized carbon nanotubes (SiO_2–CNT–COOH).[81] Porous SiO_2 effectively provides OH^-, while CNT–COOH has high electrical conductivity, thereby enhancing the catalytic activity of the alloy. The CV graph in Fig. 5d shows the catalytic performance of the alloys with SiO_2–CNT–COOH as the support in 1 M KOH with 0.1 M ammonia. The onset potential of Pt/SiO_2–CNT–COOH was rather high at 0.5 V vs.

RHE, but it shifted negatively to 0.45 V *vs.* RHE after Ir introduction. This is due to the low NH_3 adsorption energy of Ir, which facilitates NH_3 adsorption. The individual introduction of Ni onto Pt has little effect on the onset potential, but the simultaneous introduction of Ir and Ni significantly influences the onset potential thanks to their synergistic effects. In particular, the onset potential of PtIrNi$_1$/SiO$_2$–CNT–COOH (molar ratio of Pt/Ir/Ni = 9 : 1 : 1) was significantly reduced to 0.40 V *vs.* RHE. Fig. 5e shows the free-energy pathway for the NH_3 dehydrogenation step on Pt(100), Pt$_3$Ir(100), and Pt$_3$IrNi(100) surfaces at 0.3 V *vs.* RHE according to DFT calculations. The dehydrogenation of $*NH_2$ to $*NH$ on the Pt(100) surface has a thermodynamic barrier of 0.15 eV, while Pt$_3$Ir(100) becomes thermoneutral, which reduces the reaction barrier. Furthermore, on Pt$_3$IrNi(100) with Ni introduction, the dehydrogenation process becomes exergonic, leading to a predicted lower onset potential of 0.25 V *vs.* RHE. Fig. 5f shows the calculated density of states of the group d-orbital to analyze the changes in the electronic structure of the active site. The d-band center of Pt$_3$Ir(100) is −1.97 eV, which shifts upward compared to −2.25 eV for Pt(100). This supports the previous results that the introduction of Ir enhances the adsorption of $*NH$ intermediates. In Pt$_3$IrNi(100) with Ni introduction, the d-band center further shifts upward to −1.87 eV, which further improves the catalytic performance and is consistent with the lower onset potential.

2.2.2 Non-noble metal-based AOR electrocatalysts. Although precious metal catalysts show excellent performance, catalyst deactivation due to the strong adsorption of N_{ads} is a major factor that limits their practical utilization.[85] To address these issues, research on non-precious metal catalysts with good stability and cost-effectiveness is essential.[86] However, studies reported to date show that the use of non-precious metal catalysts is limited because the AOR mainly occurs at high potentials. Under these conditions, OH^- adsorption increases, leading to side reactions that form by-products such as NO_2^- and NO_3^-. In fuel cells and selective electrochemical systems, it is more important for ammonia to be efficiently and selectively oxidized at low potentials.[87] Therefore, it is urgent to develop non-precious metal-based high-efficiency catalysts with low onset potentials. For this purpose, it is crucial to optimize the reaction pathway through appropriate electronic structure control and to design active sites that enable selective oxidation.[88–90]

Huang *et al.* activated CuO by electrochemically introducing V_O through CV scanning in an alkaline solution.[82] In 1 M KOH with 0.1 M ammonia, V_O-free CuO showed little AOR activity, but the current density progressively increased as the amount of V_O increased. The onset potential of V_O-poor CuO was 0.39 V *vs.* Hg/HgO, and it gradually shifted to 0.29 V *vs.* Hg/HgO as the number of CV cycles increased, resulting in V_O-rich CuO. By analyzing the relative V_O content to lattice oxygen using the O 1s XPS spectrum in Fig. 5g, the oxygen defect peak at 531.2 eV was found to have the largest area in V_O-rich CuO. This confirms that the generation of V_O is the key principle

enhancing the electrochemical activity. DFT calculations revealed that V_O shifts the d-band center of CuO closer to the Fermi level, which stabilizes the $*NH_x$ intermediate and improves the AOR performance. The FE results, shown in Fig. 5h, demonstrated that the N_2 selectivity of V_O-rich CuO was 62.8%, significantly higher than that of the control. These results were attributed to the introduction of V_O, which changed the reaction energy of the dehydrogenation step, enabling selective oxidation to N_2. Nagita *et al.* reported layered MnO_2 thin films (NiCu/MnO$_2$) co-intercalated with Ni^{2+} and Cu^{2+} ions coordinated with water molecules.[91] While single-component Ni/MnO$_2$ and Cu/MnO$_2$ show little difference in current density before and after NH_3 addition, NiCu/MnO$_2$ shows a distinct difference. This shows that the intercalated Cu ions cannot directly oxidize NH_3 at potentials lower than 0.6 V *vs.* Hg/HgO, but facilitate electron transfer when Ni^{2+} is oxidized to Ni^{3+}. In 0.5 M NaOH and 55 mM NH_4Cl, it selectively generated N_2 with an FE of 97.4% at 0.6 V *vs.* Hg/HgO. In contrast, NiCu bimetal showed a lower N_2 selectivity of 53.8% at 0.6 V *vs.* Hg/HgO. This is because the interlayer of NiCu/MnO$_2$ promotes the formation of N–N bonds from partially dehydrogenated NH_3 species before oxidation to NO_x. Wang *et al.* introduced Ni$_1$Cu$_1$Co$_{0.5}$-S-T/CP, a three-dimensional nanoflower structure, by co-doping Co and S onto NiCu.[92] In 1 M NaOH and 0.2 M NH_4Cl, the onset potential of Ni$_1$Cu$_1$Co$_{0.5}$-S-T/CP was 1.241 V *vs.* RHE, which was lower than that of Ni$_1$Cu$_1$-T/CP (1.377 V *vs.* RHE) and Ni$_1$Cu$_1$-S-T/CP (1.374 V *vs.* RHE). S doping induces the surface reconfiguration of the electrode, exposing more active sites and improving the electrical conductivity. Meanwhile, Co doping modifies the NiCu electronic structure and increases the number of redox electron pairs, enhancing the catalytic performance. In addition, Co doping lowers the reaction energy barrier for N–H bond cleavage, which further facilitates the dehydrogenation process. As a result, the co-doping of Co and S accelerates the dehydrogenation reaction through the G–M mechanism, resulting in a high N_2 selectivity of 81.21%. Kashale *et al.* synthesized boron-doped NiCu oxide (NiCuBO) and evaluated its AOR and OER performance.[93] In the NiCuBO/NF-1||NiCuBO/NF-1 two-electrode system, 1.56 V is required to achieve 10 mA cm^{-2} in 1 M KOH with 0.5 M ammonia, representing a 110 mV decrease compared to water electrolysis. Furthermore, at 50 mA cm^{-2}, the system demonstrates excellent stability for 24 h. Fig. 6 shows the N_2 FE as a function of the potential applied to the AOR electrocatalyst. Noble metal-based catalysts exhibit high N_2 FE at low potentials, while non-noble metal-based catalysts exhibit relatively low N_2 FE at high potentials. Therefore, optimizing the operating potentials and controlling the reaction pathway of non-noble metal-based catalysts remain major challenges to improve N_2 selectivity.

2.3 Urea oxidation reaction

Large amounts of urine containing 2–2.5 wt% urea are produced by animals and humans, which requires urine-rich wastewater treatment to prevent producing toxic ammonia and further oxidized species.[94] Electrocatalytic urea oxidation

© 2025 The Author(s). Co-published by the Institute of Process Engineering, Chinese Academy of Sciences and the Royal Society of Chemistry

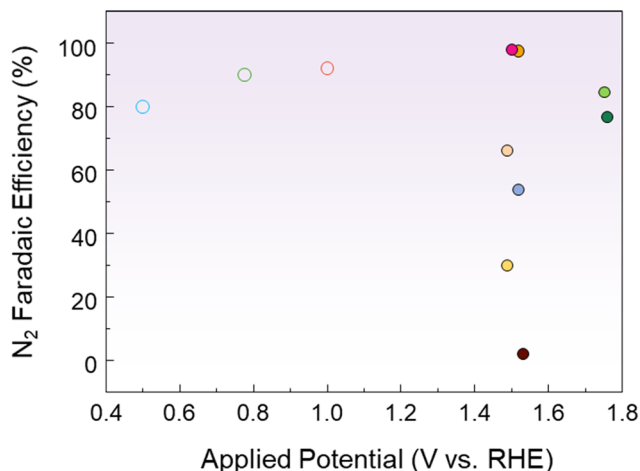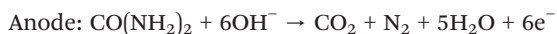*Ind. Chem. Mater.*, 2025, **3**, 277–310 | 287

Fig. 6 Comparison of the AOR performance of various electrocatalysts. Each potential was converted to RHE, considering the reference electrode and pH of the electrolyte. The detailed values are shown in the ESI.†

can be one of the environmentally-friendly technologies by converting urea into N_2, CO_2, and H_2O using sustainable energy-derived electricity. The urea oxidation reaction at the anode requires a theoretical thermodynamic potential of −0.46 V vs. SHE (standard hydrogen electrode) and a cathode with a theoretical potential of −0.83 V vs. SHE for the HER. Therefore, the overall urea electrolysis requires 0.37 V.

$$\text{Anode: } CO(NH_2)_2 + 6OH^- \rightarrow CO_2 + N_2 + 5H_2O + 6e^-$$

$$\text{Cathode: } 6H_2O + 6e^- \rightarrow 3H_2 + 6OH^-$$

$$\text{Overall: } CO(NH_2)_2 + 5H_2O \rightarrow CO_2 + N_2 + 3H_2$$

DFT calculation methods provide a better understanding of the reaction mechanism for the UOR, which can undergo different pathways depending on the electrocatalysts. As a selected example, Zhang et al. showed that the NiOOH surface follows the pathway *CO(NH_2)_2 → *CONHNH_2 → *CONHNH → *CONHN → *CON_2 → *CO → *COOH → *COOHOH → *COO → CO_2.[95] In contrast, the reaction proceeding at NiOO with a higher oxidation surface shows *CO(NH_2)_2 → *CONHNH_2 → *CONHNH → *V_O–CONHN → *V_O–NNH → *V_O–NN → *V_O → V_O–OHOH → H_2O. Although the theoretical voltage required for the UOR is significantly lower than that for the OER (1.23 V), it suffers from sluggish kinetics by the 6-electron transfer process, which requires the design of high-performance UOR electrocatalysts. In 1973, Yao et al. first demonstrated urea oxidation using a Pt anode.[96] Sharing the same considerations for selecting electrocatalyst materials for water electrolysis, platinum group metal (Pt, Rh, Ir)-based materials are not ideal candidates for large-scale applications due to their high cost and scarcity.[97] Non-noble metal-based electrocatalysts have gained attention due to their high performance in alkaline

environments.[98] Gao et al. summarized the three possible UOR pathways under alkaline conditions, depending on the adsorption of urea molecules.[94] Considering that the predominantly used environment for the UOR is alkaline electrolytes, consuming the OH^- at the anode sides, recent research has focused on Ni or Co-based hydroxides, alloys, sulfides, phosphides, selenides, oxides, and so on. Various strategies to develop efficient UOR catalysts include designing heterojunction catalysts, electrocatalysts having high oxidation states, and dual catalytically active sites by doping or mixing catalysts.[99–101] Fig. 7 shows the comparison of urea-assisted water electrolysis using various electrocatalysts.

2.3.1 Ni-based UOR electrocatalysts. Ni-based catalysts have been considered active materials for the UOR, attributed to their high-valence states (Ni^{3+}, Ni^{4+}). Since Boggs et al. first reported non-noble metal Ni-based catalysts for the electrochemical UOR in 2009, Ni-based catalysts, such as Ni-based phosphides, oxides, sulfides, (oxy)hydroxides, hybrids, and single atoms, have gained attention as UOR electrocatalysts with high electrocatalytic activity.[102–104] As selected studies of investigating the catalytic effects of Ni, Jiang et al. reported Ni single atoms anchored on N-doped carbon nanosheets (Ni SAs-NC) as bifunctional catalysts for urea-assisted rechargeable Zn–air batteries.[105] Zhan et al. deposited Ni on Ti foam, synthesizing atomically isolated asymmetric Ni–O–Ti sites.[106] They discovered that oxygenophilic Ti promotes urea adsorption on Ni–O–Ti sites and prevents premature C–N bond cleavage before N–N coupling. As a result, 99% selectivity toward N_2 and 10 day durability, preventing the poisoning of catalysts from NO_x^- and NCO^-, were achieved. Recent studies showed the lattice oxygen mechanism (LOM) as a viable strategy for urea electrolysis. The doping of tungsten on nickel catalysts (Ni-WO_x) affected the electronic structure of the catalysts, which facilitates the formation of active Ni^{3+}, increases d-band occupancy states on W atoms, and changes the chemical
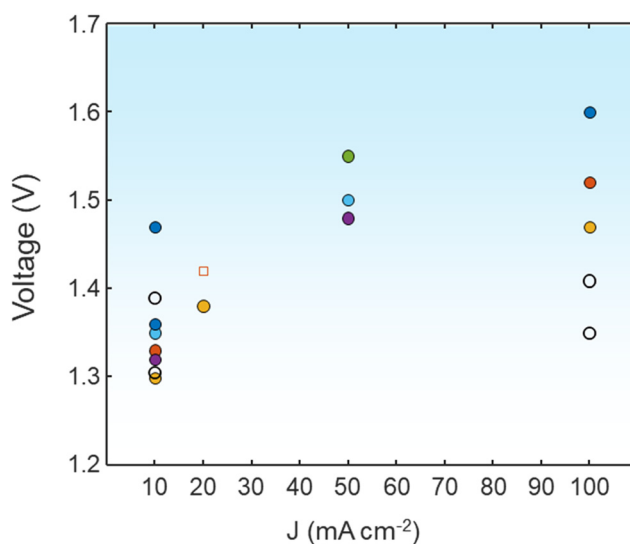

Fig. 7 A comparison of the UOR||HER with various electrocatalysts in terms of cell voltage at various current densities. The detailed values are shown in the ESI.†

environment of Ni and W.[107] As a result, Ni-WO$_x$ catalysts required 1.4 V to deliver the UOR current density of 100 mA cm^{-2}, which is 273 mV lower than that of the OER. Zhang *et al.* demonstrated that the lattice oxygen-involved reaction on Ni^{4+} oxides prepared by electrochemical oxidation of NiClOH showed higher UOR activity compared to Ni^{3+} oxides from Ni(OH)$_2$ oxidation.[95] The energetically preferable UOR pathway on Ni^{4+} oxides was confirmed by DFT, which promotes CO$_2$ generation in reaction steps.

Nickel hydroxide is one of the representative UOR electrocatalysts, which further reacts with OH$^-$ to form NiOOH active species. Sun *et al.* reported synthesized self-supported

hierarchical Ni(OH)$_2$-decorated CuO nanowires supported on Cu foam (Ni(OH)$_2$/CuO NWs/CF) for the UOR.[108] As shown in Fig. 8a, Ni(OH)$_2$ was uniformly electrodeposited on CuO nanowires, which provides substantial active sites and high electrical conductivity for charge transfer. They used DFT calculations to unravel the UOR activity from the Ni(OH)$_2$/CuO NWs/CF by comparing the adsorption energy of urea and OH$^-$ using (111) surface models. Both CuO and Ni(OH)$_2$ have larger adsorption energy toward urea rather than OH$^-$, compared to NiFe LDHs. As depicted in Fig. 8b, by comparing the adsorption energy of OH$^-$ on CuO (111), Ni(OH)$_2$, and CuO (111)/Ni(OH)$_2$, the intermediate adsorption behavior of the Ni(OH)$_2$/CuO NWs/
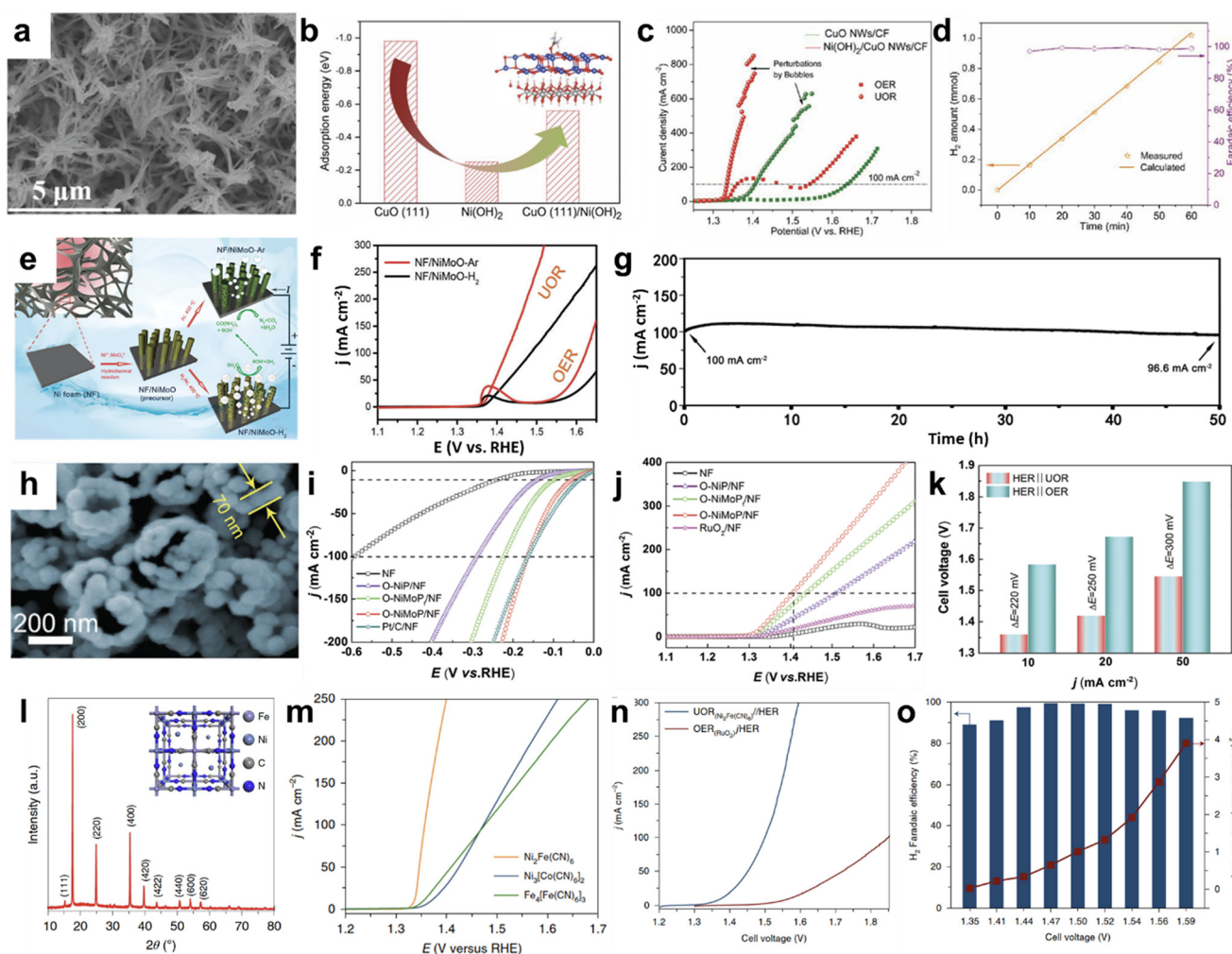

Fig. 8 Urea oxidation reaction (UOR) using Ni-based electrocatalysts. (a) SEM image of Ni(OH)$_2$/CuO NWs/CF. (b) Comparison of adsorption energies of urea of different surface models. (c) Polarization curves for the UOR and OER using CuO NWs/CF and Ni(OH)$_2$/CuO NWs/CF. (d) Faradaic efficiency and generated amount of hydrogen during urea electrolysis. (a–d) Reprinted with permission.[108] Copyright 2022, Wiley-VCH GmbH. (e) Schematic illustration of catalyst preparation of NF/NiMoO–Ar (UOR) and NF/NiMoO–H$_2$ (HER). (f) Polarization curves of NF/NiMoO–Ar and NF/NiMoO–H$_2$ for the UOR and OER. (g) Stability test of urea electrolysis (UOR‖HER) using NF/NiMoO–Ar as a UOR catalyst and NF/NiMoO–H$_2$ as a HER catalyst performed at a cell voltage of 1.58 V. (e–g) Reproduced with permission.[110] Copyright 2018, The Royal Society of Chemistry. (h) SEM image of O–NiMoP/NF. (i) HER polarization curves of various electrocatalysts measured in 1.0 M KOH. (j) UOR polarization curves of various electrocatalysts in 1.0 M KOH with 0.5 M urea. (k) Comparison of cell voltage for water electrolysis and urea electrolysis at different current densities. (h–k) Reproduced with permission.[111] Copyright 2021, Wiley-VCH GmbH. (l) XRD patterns of synthesized Ni$_2$Fe(CN)$_6$ catalysts. The inset shows the schematic illustration of Ni$_2$Fe(CN)$_6$. (m) Polarization curves of various catalysts in 1 M KOH with 0.33 M urea. (n) Comparison of LSV curves of the UOR‖2e$^-$-ORR and OER‖2e$^-$-ORR. (o) Faradaic efficiency and H$_2$ production rate during urea electrolysis at different cell voltages. (l–o) Reprinted with permission.[15] Copyright 2021, Springer Nature.

© 2025 The Author(s). Co-published by the Institute of Process Engineering, Chinese Academy of Sciences and the Royal Society of Chemistry

Ind. Chem. Mater., 2025, 3, 277–310 | 289

CF explains the highly catalytically active UOR performances. The polarization curves of CuO/CF and Ni(OH)$_2$/CuO/CF show the preferential UOR over the OER in 1 M KOH with or without 0.5 M urea. Hierarchical Ni(OH)$_2$/CuO/NF requires 1.334 V to generate the current density of 100 mA cm^{-2} for the UOR, which is 71 mV lower than that of CuO/NF (Fig. 8c). Urea electrolysis was performed by coupling Ni(OH)$_2$/CuO NWs/CF as an anode and Pt/C/NF as a cathode at an applied current density of 20 mA cm^{-2}, showing a linear increment of the H$_2$ amount and nearly 100% faradaic efficiency (Fig. 8d). Chen et al. introduced nickel sulfoselenide (Ni–S–Se) on the Ni(OH)$_2$ surface grown on Ni foam (Ni–S–Se/NF) as HER and UOR catalysts.[109] The presence of S in Ni–S–Se/NF steers the HER with an optimal hydrogen free energy based on DFT calculations, and the in situ formed nickel oxyhydroxide (NiOOH) from sulfoselenide is an active species for the UOR.

Bimetallic nickel–molybdenum (NiMo)-based electrocatalysts have been considered as bifunctional catalysts for water electrolysis, especially showing catalytically active HER performance under alkaline conditions.[112] Therefore, studies of NiMo-based electrocatalysts for urea electrolysis (UOR + HER) have been conducted by researchers. Yu et al. reported porous rod-like NiMoO$_4$ with high oxidation states of the metal elements for an efficient UOR.[110] As depicted in Fig. 8e, they first pre-synthesized NiMoO$_4$·xH$_2$O nanorods on Ni foam, which were subsequently annealed in an Ar atmosphere or reductive H$_2$/Ar (5%/95%) mixture gas to obtain NF/NiMoO–Ar and NF/NiMoO–H$_2$, respectively. Annealing of NiMo-based materials in different atmospheres affected UOR properties, as shown in Fig. 8f. NF/NiMoO–Ar showed a current density of 100 mA cm^{-2} at 1.42 V vs. RHE in 1 M KOH with 0.5 M urea, which is attributed to the easier oxidation of Ni^{2+} to Ni^{3+} by Mo^{6+} in NiMoO-Ar. However, when the sample was annealed under H$_2$ conditions, NF/NiMoO–H$_2$ showed mostly Ni^0, Mo^{3+}, and Mo^{4+}, which makes it difficult to form Ni^{3+} active species. Instead, NF/NiMoO–H$_2$ showed comparable catalytic activity to platinum in 1 M KOH, exhibiting low overpotentials of 11 mV to yield 10 mA cm^{-2} and 53 mV for the current density of 100 mA cm^{-2}. By utilizing NF/NiMoO–Ar as an anode and NF/NiMoO–H$_2$ as a cathode for the overall UOR, the potential of 1.38 V was required to reach the current density of 10 mA cm^{-2} and 1.55 V for 100 mA cm^{-2}. Fig. 8g shows the stable urea electrolysis performed at a cell voltage of 1.58 V for 50 h, indicating potential for a noble-metal-free urea electrolyzer. Jiang et al. synthesized oxygen-incorporated NiMoP nanotube arrays, consisting of interconnected nanoparticles of 70 nm in diameter, as bifunctional electrocatalysts for the UOR and HER (Fig. 8h).[111] The HER polarization curves exhibit that O–NiMoP/NF has a comparable overpotential of 54 mV (at J = 10 mA cm^{-2}) to Pt/C/NF (Fig. 8i). In the case of the UOR, O–NiMoP/NF only requires 1.41 V for generating 100 mA cm^{-2}, which is 340 mV lower than that of the OER. Compared to O–NiP/NF or conventional RuO$_2$/NF, O–NiMoP/NF Mo, P, and O atoms modulated the electronic environment of catalytically active Ni sites, contributing to improved electrocatalytic activity and durability (Fig. 8j). The urea-assisted electrolysis system showed

a cell voltage of 1.55 V at the current density of 50 mA cm^{-2} in 1 M KOH with 0.5 M urea, 0.3 V lower than that of water electrolysis (Fig. 8k). Liu et al. synthesized nickel phosphide nanoflake arrays on carbon cloth (Ni$_2$P NF/CC) as a 3D catalyst electrode for the UOR, which requires 0.447 V to deliver the current density of 100 mA cm^{-2} in 1 M KOH with urea.[113] Urea electrolysis using bifunctional Ni$_2$P NF/CC||Ni$_2$P NF/CC needs a cell voltage of 1.35 V to achieve 50 mA cm^{-2}, 0.58 V lower than that of water electrolysis.

As a form of Ni-based framework electrocatalysts, Geng et al. demonstrated nickel ferrocyanide (Ni$_2$Fe(CN)$_6$) as a high-performance urea oxidation catalyst with high activity and stability.[15] The structural analysis of Ni$_2$Fe(CN)$_6$ using XRD revealed that the Fe atom coordinates with carbon atoms in CN$^-$ and the Ni atoms coordinate with CN$^-$ species and are located in the center (Fig. 8l). Among catalysts having similar structures (Ni$_3$[Co(CN)$_6$]$_2$ and Fe$_4$[Fe(CN)$_6$]$_3$), Ni$_2$Fe(CN)$_6$ having Ni^{2+} and Fe^{2+} showed noticeable UOR properties in 1 M KOH with 0.33 M urea. It requires a potential of 1.35 V to generate a current density of 100 mA cm^{-2}, 330 mV lower than that of the OER (Fig. 8m). As shown in Fig. 8n, urea electrolysis (UOR|| HER) requires a cell voltage of 1.38 V to obtain the current density of 10 mA cm^{-2} and 1.5 V for 100 mA cm^{-2}. This system was energy efficient compared to conventional water electrolysis, which requires 1.56 V and 1.85 V, respectively. The following H$_2$ production rates increased as a function of cell voltage and the faradaic efficiency of urea electrolysis showed over 90% (Fig. 8o). By taking advantage of the structural diversity and porous features of MOFs, Li et al. reported a 2D MOF with mono-coordinated ferrocenecarboxylic acid (Fc) as a UOR catalyst.[114] The NiFe-oxalate MOF, which was prepared by thermochemical treatment of Ni$_3$Fe alloy foam in oxalic acid, showed a UOR current density of 500 mA cm^{-2} at 1.47 V vs. RHE in 1 M KOH with 0.33 M urea.[115] The oxalate ligands induce the charge deficient Ni center and provide stable urea-O adsorption. Furthermore, the incorporated Fe enhances oxalate-O charge density and strengthens the H-bond with urea to overcome the rate-determining C–N cleavage of *CO(NH$_2$). Metallic glasses (MGs) have a high Gibbs free energy state and a high density of low coordination states, which make them promising electrocatalyst candidates. Pei et al. prepared nanostructured Ni–P nanoglasses (NGs) with a heterogeneous microstructure, which showed high catalytic activity toward the UOR, OER, and HER. Ni–P-NG showed a low required potential for delivering 10 mA cm^{-2}.[116]

2.3.2 Co-based UOR electrocatalysts. Urea (Co(NH$_2$)$_2$) has an amino group, which is an electron-donating group, and a carbonyl group, which is an electron-withdrawing group. Therefore, it is required to develop catalysts that behave like Janus particles, having two distinct and different properties on the surfaces. Li et al. developed Schottky heterojunction catalysts by taking metallic CoS$_2$ and semiconducting MoS$_2$ to form a spontaneous electron flow across the CoS$_2$/MoS$_2$ interfaces.[117] The work function of CoS$_2$ corresponds to 3.9 eV and that of n-type MoS$_2$ to 4.8 eV, which generate the electron transfer from CoS$_2$ to MoS$_2$ and form charge density

redistribution confirmed by DFT calculations (Fig. 9a). Urea electrolysis using CoS_2/MoS_2 as both an anode and a cathode requires a cell voltage of 1.54 V to achieve 100 mA cm^{-2}, which is 260 mV less than that of water electrolysis (Fig. 9b). Similarly, Wang et al. designed Schottky catalysts which consist of semiconducting $CoMn_2O_4$ and metallic CoMn to steer the transfer at the interfaces and facilitate the UOR.[118] The work function of CoMn is calculated to be 4 eV and that of $CoMn_2O_4$ is calculated to be 4.53 eV by ultraviolet photoelectron spectroscopy (UPS), forming the Schottky barrier at the $CoMn_2O_4$/CoMn interfaces, as shown in Fig. 9c. This resulted in 1.36 V for the UOR and 1.61 V for the OER at 100 mA cm^{-2}. As the current density increases to 200 mA cm^{-2} and 300 mA cm^{-2}, the required potentials are 1.385 V and 1.41 V, which shows only 50 mV increases to achieve 3-fold current densities (Fig. 9d).

Layered double hydroxides (LDHs) are a widely used form of electrocatalysts. Their 2D structures increase the active surface area and facilitate charge transfer in the oxygen evolution reaction. Song et al. prepared Co(OH)F and CoP-nanoarrays on Ni-foam, which have abundant active sites and facile pathways for ion/electron transport by taking advantage of their porous structure.[120] Using Co–P/NF (cathode) and Co(OH)F/NF (anode), urea electrolysis requires a 1.42 V cell voltage for delivering a current density of 20 mA cm^{-2} in 1 M KOH with 0.7 M urea. Yu et al. reported hierarchical Fe-doped cobalt selenide coupled with FeCo LDH arrays designed for both the UOR and HER.[121] Heterostructured Fe–$Co_{0.85}$Se/FeCo LDH modulated the local interfacial bonding environment, facilitating the electron transfer and interface interactions at the interfacial Co–Se/O–Fe bonding. Free energy diagrams of the UOR through DFT calculation revealed that Fe–$Co_{0.85}$Se/FeCo LDH can stabilize
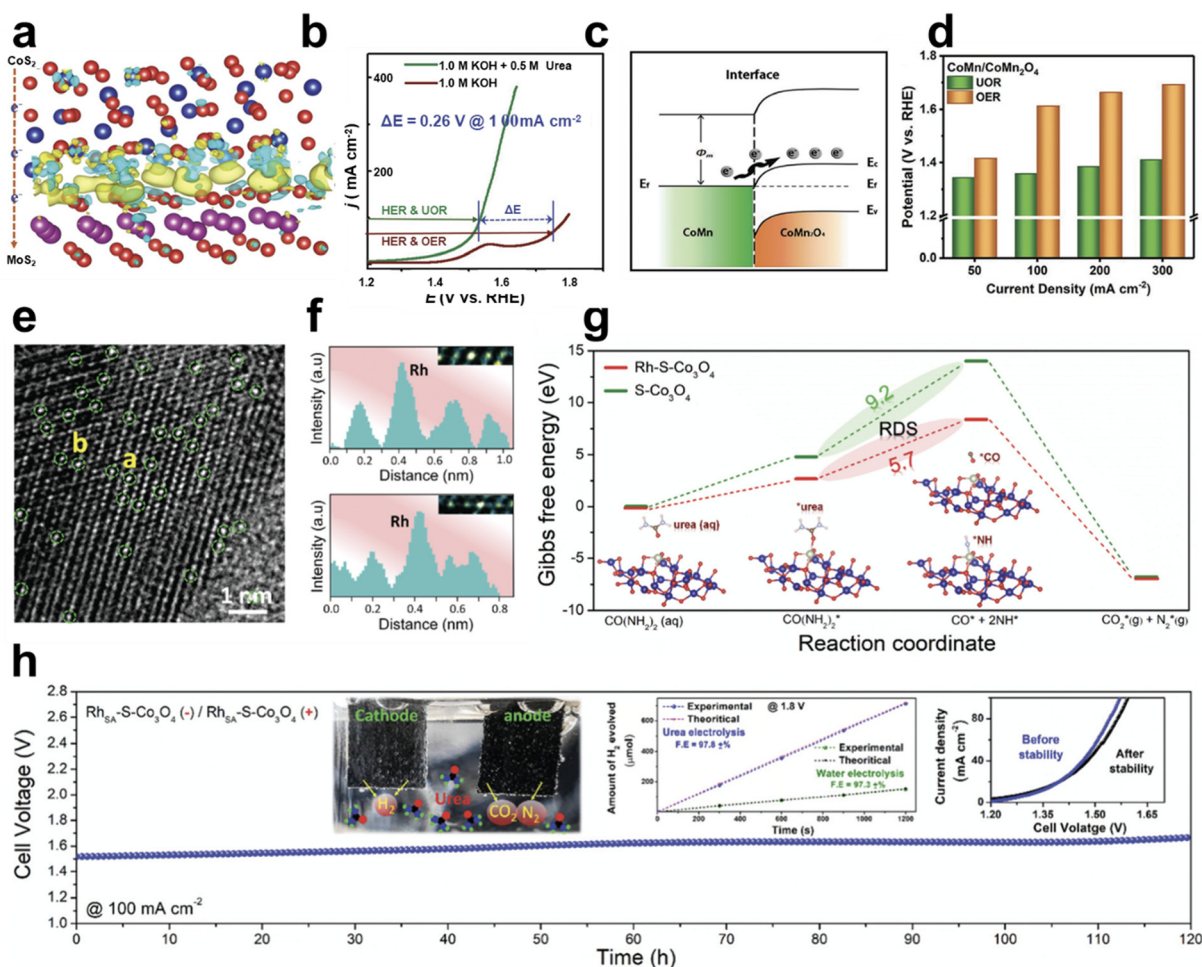

Fig. 9 Urea oxidation reaction (UOR) using Co-based electrocatalysts. (a) The charge density distribution in the CoS_2/MoS_2 heterostructure. (b) Polarization curves of CoS_2–MoS_2 in 1 M KOH with or without 0.5 M urea. (a and b) Reprinted with permission.[117] Copyright 2018, Wiley-VCH GmbH. (c) Energy band diagram of the CoMn/$CoMn_2O_4$ Schottky heterojunction. (d) Comparison of the UOR and OER performance at various current densities. (c and d) Reprinted with permission. Copyright 2020, Wiley-VCH GmbH. (e) TEM image of Rh_{SA}–S-Co_3O_4 with green circles indicating Rh single atom sites on S-Co_3O_4 and (f) line-scanning intensity profile at sites a and b. (g) Reaction free energy profiles of the UOR of S-Co_3O_4 with or without Rh_{SA}. (h) Stability test of urea electrolysis at a current density of 100 mA cm^{-2}. The inset shows the comparison of H_2 generation between urea and water electrolysis at a cell voltage of 1.8 V and the polarization curves before and after urea electrolysis. (e–h) Reprinted with permission.[119] Copyright 2021, The Royal Society of Chemistry.

© 2025 The Author(s). Co-published by the Institute of Process Engineering, Chinese Academy of Sciences and the Royal Society of Chemistry

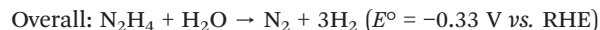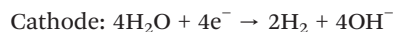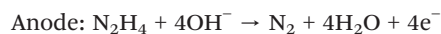Ind. Chem. Mater., 2025, 3, 277–310 | 291

intermediates, resulting in high UOR catalytic activity. Wang *et al.* synthesized Cr-doped CoFe LDH on a Ni foam (NF) nanosheet array as an OER and UOR electrocatalyst, where the catalytic activity originates from the high-valence Cr^{6+} from the spontaneous oxidation of Cr-doped CoFe LDH acting as electron-withdrawing sites.[122] Doping of Cr also enhances the extent of adsorption of the active sites for the H_2O molecules. Urea electrolysis using Cr-doped CoFe LDH/NF (anode) and Pt–C/NF (cathode) required 1.305 V at the current density of 10 mA cm^{-2} in 1 M KOH with 0.33 M urea.

In a one-dimensional form, nanoparticles have been widely used for electrochemical systems due to their tunable size, composition, and nanoparticle–support interaction. Kang *et al.* formed ZIF-67-derived CoP nanoparticles confined in P, N, and Co-doped porous carbon (PNC) and attached to P-doped carbonized wood fibers (PCWF).[123] With an enlarged surface area and high catalytic activity, CoP@PNC/PCWF required 1.321 V to generate a UOR current density of 50 mA cm^{-2}, which is 257 mV lower than that of the OER. Single-atom catalysts (SACs) have shown great promise in energy conversion/applications due to their unique properties (electronic configuration, local coordination) and catalytic activities. However, the high surface energy of SACs causes agglomeration and results in low loading of SACs on the support. Kumar *et al.* introduced single-atom ruthenium (Rh_{SA}) on a tensile-strained Co_3O_4 (S-Co_3O_4) support prepared by liquid N_2-quenching methods, achieving 2 times higher loading of Rh_{SA} for the UOR.[119] As shown in Fig. 9e and f, the TEM image of Ru_{SA}–S-Co_3O_4 and the line scanning profile at sites a and b confirmed the stabilized distribution of Ru_{SA} on the S-Co_3O_4. The required potential to achieve the urea oxidation current density of 10 mA cm^{-2} of Ru_{SA}–S-Co_3O_4 was 1.28 V, 80 mV lower than that of S-Co_3O_4. Ru_{SA}–S-Co_3O_4 also showed 190 mV less potential (at 100 mA cm^{-2}) for the UOR, compared to the OER. The reaction-free energy profiles for the UOR on Ru_{SA}–S-Co_3O_4 and S-Co_3O_4 were calculated to understand the effects of Ru_{SA}. As shown in Fig. 9g, *$CO(NH_2)_2$ to *CO + 2*NH is the rate-determining step (RDS) and Ru_{SA} stabilizes the *CO and *NH intermediates with a moderate urea adsorption energy (1.16 eV) compared to S-Co_3O_4 (1.72 eV), facilitating the adsorption and activation of urea. The urea electrolyzer using Rh_{SA}–S-Co_3O_4 for both the anode and cathode showed over 100 h stability at 100 mA cm^{-2}, confirming the higher amount of hydrogen generation and faradaic efficiency compared to the water electrolysis at 1.8 V (Fig. 9h). Nguyen *et al.* introduced Rh single atoms in Co_3S_4/CoO_x heterostructured nanosheet (NS)-assembled nanotube (NT) arrays on a 3D copper framework (3D-CF).[124] Compared to the pure 3D-CF with low hydrophilicity behavior, Rh–Co_3S_4/CoO_x NTs showed a super-hydrophilic surface, facilitating electrolyte infiltration and increasing the density of accessible active sites. Introducing Rh on Co_3S_4/CoO_x NTs steered the UOR with a low overpotential of 1.32 V at 10 mA cm^{-2}, lower than that of Co_3S_4/CoO_x NTs (1.37 V), CoO_x NTs (1.40 V), and CuO NRs (1.48 V). Furthermore, Rh showed small hydrogen adsorption free energy close to 0

from the DFT calculation, explaining its HER catalytic activity. Using Rh–Co_3S_4/CoO_x NTs as an anode and a cathode, urea electrolysis required a cell voltage of 1.48 V to achieve a current density of 50 mA cm^{-2} and showed stable 50 h operation in 1 M KOH with 0.5 M urea.

2.4 Hydrazine oxidation reaction

Hydrazine (N_2H_4) is a small molecule, an important forming agent propellant and rocket fuel, a crucial electroanalytical target, and a useful reductant in organic synthesis.[125] As a small-molecule oxidation reaction, hydrazine can be easily oxidized at lower potentials than the OER, decreasing significant energy consumption for hydrogen production. The hydrazine oxidation reaction (HzOR) has gained significant research attention due to its low thermodynamic potential (−0.33 V *vs.* RHE) and fast electro-oxidation kinetics.[126]

$$\text{Anode: } N_2H_4 + 4OH^- \rightarrow N_2 + 4H_2O + 4e^-$$

$$\text{Cathode: } 4H_2O + 4e^- \rightarrow 2H_2 + 4OH^-$$

$$\text{Overall: } N_2H_4 + H_2O \rightarrow N_2 + 3H_2 \ (E^\circ = -0.33 \text{ V } vs. \text{ RHE})$$

In detail, the HzOR generally follows the deprotonation pathway *N_2H_4 → *N_2H_3 → *N_2H_2 → *N_2H → *N_2 → N_2. Since hydrazine consists of N and H, the HzOR generates only nitrogen and water. It has a high energy density (5.40 kW h L^{-1}, 1 atm) and is fully miscible in water. Fig. 10 compares the required cell voltage of the HzOR||HER system for delivering various current densities.

Metal phosphide-based hybrid structures have gained attention due to their Pt-like HER activity with lower metal loadings. As HzOR electrocatalysts, Zhu *et al.* synthesized 3D nickel cobalt phosphide heterostructures on Ni foam (Ni-Co-P/NF) with uniformly distributed CoP nanoparticles for both HER and HzOR electrocatalysts.[16] The use of Ni-Co-P/NF catalysts as both an anode and a cathode requires 0.498 V to reach 500 mA cm^{-2}. The high catalytic activity of the catalysts originated from the instantaneous recovery of metal phosphide active sites by N_2H_4, where the oxidized metal phosphide species could be reduced back to active metal phosphides. Li *et al.* designed RuP_2-decorated N, P-doped carbon porous nanosheets (RP-CPM) for both HzOR and HER catalysts.[127] A low cell voltage of 23 mV is required to achieve 10 mA cm^{-2} for HzOR-assisted water electrolysis. DFT calculation results supported the catalytic activity of RP-CPM: hydrogen adsorption on C-active sites is thermoneutral for the HER and favorable hydrazine dehydrogenation on active Ru sites.

Lattice strain engineering is one of the efficient strategies to improve the catalytic activity of various electrocatalysts. Modulating the lattice strain affects the adsorption strength of the reaction intermediates, facilitating the electrochemical reactions. Feng *et al.* manipulated the lattice strain of Ni_2P
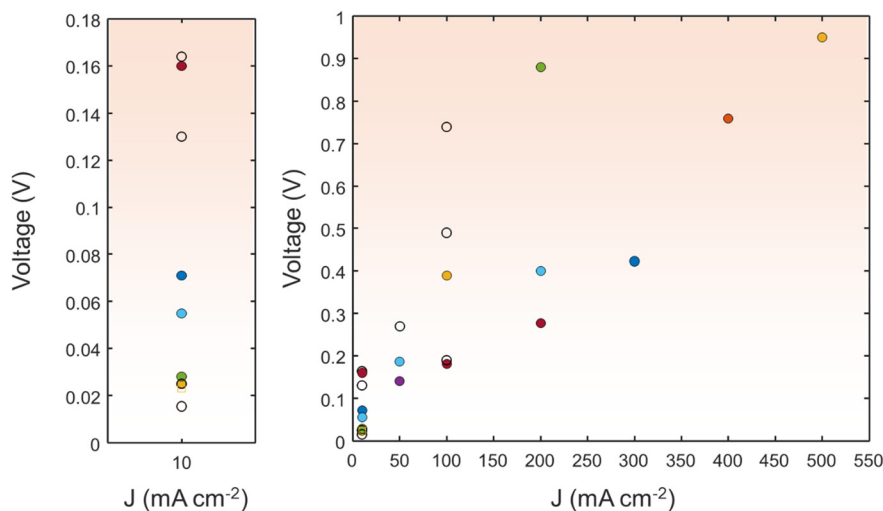
Fig. 10 A comparison of the HzOR||HER with various electrocatalysts in terms of cell voltage at various current densities. The detailed values are shown in the ESI.†

nanosheets by dual cation (Cu and Co) co-doping by synthesizing Ni hydroxide precursors with dopants and subsequent phosphating of precursors to generate metal-doped Ni_2P.[128] As shown in Fig. 11a, synthesized metal-doped Ni_2P shows porous two-dimensional structures with distinct lattice spacing toward the Ni_2P (111) direction. Based on the lattice spacing of pristine Ni_2P (111), doping of Co or Cu induces the tensile strain, while co-doping of Cu and Co formed the compression strain. The effects of strain engineering of Ni_2P nanosheets are shown in the HzOR polarization curves (Fig. 11b). Co-doped Cu_1Co_2-Ni_2P/NF showed the lowest required potential of −52 mV to achieve a current density of 10 mA cm^{-2}. In comparison, those of tensile-strained Cu-Ni_2P/NF and Co-Ni_2P/NF were 18 mV and 28 mV, respectively. The compressive strain reduces the energy barrier of the *N_2H_4 to *N_2H_3 dehydogenation step, contributing to the improved HzOR. With the optimized doping of Ni_2P/NF, hydrazine electrolysis was conducted in 1 M KOH with 0.1 M N_2H_4 using Cu_1Co_2-Ni_2P/NF as both an anode and a cathode. As shown in Fig. 11c, hydrazine-assisted water electrolysis required 0.16 V and 0.39 V to deliver the current density of 10 and 100 mA cm^{-2}, respectively, which are significantly lower than those of the water electrolysis.

Although the platinum group metals are catalytically active, their high costs are challenging for large-scale applications. Therefore, it is required to reduce the amount of PGMs while maintaining their catalytic activity. Composition control of electrocatalysts is one well-known strategy to enhance catalytic activity and stability. Li *et al.* designed a hybrid structure composed of intermetallic $CoPt_3$ and Pt-doped Co particles on the N-doped carbon skeleton ($CoPt_3$/$CoPt{\subset}P_LNC$) with a puff-like structure.[131] Using $CoPt_3$/$CoPt{\subset}P_LNC$ as both an anode and a cathode, the overall hydrazine splitting system requires low cell voltages of 0.13, 0.27, and 0.49 V, which are responsible for generating current

densities of 10, 50 and 100 mA cm^2. Feng *et al.* demonstrated the design of HEAs, which requires mixing of generally five or more elements equally or having relatively large proportions.[132] HEA nanoclusters (NCs), having an average size of 1.48 nm, consist of Pt, Ru, Co, Mo, and Ni with optimized composition. Overall hydrazine oxidation-assisted splitting (OHzS) using HEANCs on carbon supports (C) as both an anode and a cathode requires 0.025 and 0.181 V for generating 10 and 100 mA cm^{-2}.

Ruthenium (Ru) is a promising alternative to the Pt in Pt-group metals for the HER with similar hydrogen bond energy to Pt and electron-rich Ru sites. Ru can also benefit the HzOR because it can stabilize HzOR intermediates, as studied by DFT calculations in previous reports. Considering the overall hydrazine-assisted water electrolysis (HzOR/HER), utilizing Ru as catalytically active species for the HzOR has been studied. Guan *et al.* studied the role of Ru single atoms and nanoclusters prepared on a porous N-doped carbon (Ru/PNC) composite, which requires 1 and −20.4 mV to deliver 10 mA cm^{-2} for the HER and HzOR, respectively.[133] DFT calculations revealed that the Ru SAs have optimal ad/desorption free energies for dehydrogenating N_2H_4 intermediates. Li *et al.* introduced Ru single atoms into the sulfur vacancies of tungsten disulfide nanosheets (WS_2 NSs) using galvanostatic deposition grown on carbon cloth (CC@WS_2/Ru SAs) (Fig. 11d), showing layers of the WS_2 nanosheet structure without a morphology change.[129] The presence of Ru SAs in WS_2 is analyzed through extended EXAFS, where Ru K-edge Fourier-transformed (FT) EXAFS spectra show peaks at 1.63 Å, corresponding to Ru–W, and 2.2 Å, attributed to Ru–S (W bridge) interaction (Fig. 11e). The well-marked Ru–Ru peak at 2.33 Å and Ru–O–Ru peak at 3.19 Å didn't show up, which agrees with the presence of Ru SAs in WS_2. Fig. 11f shows the polarization curves of HzOR-assisted water electrolysis with a distinct configuration, where the CC@WS_2/Ru-450 (anode)|| CC@WS_2/Ru-450 (cathode) system showed the lowest

© 2025 The Author(s). Co-published by the Institute of Process Engineering, Chinese Academy of Sciences and the Royal Society of Chemistry
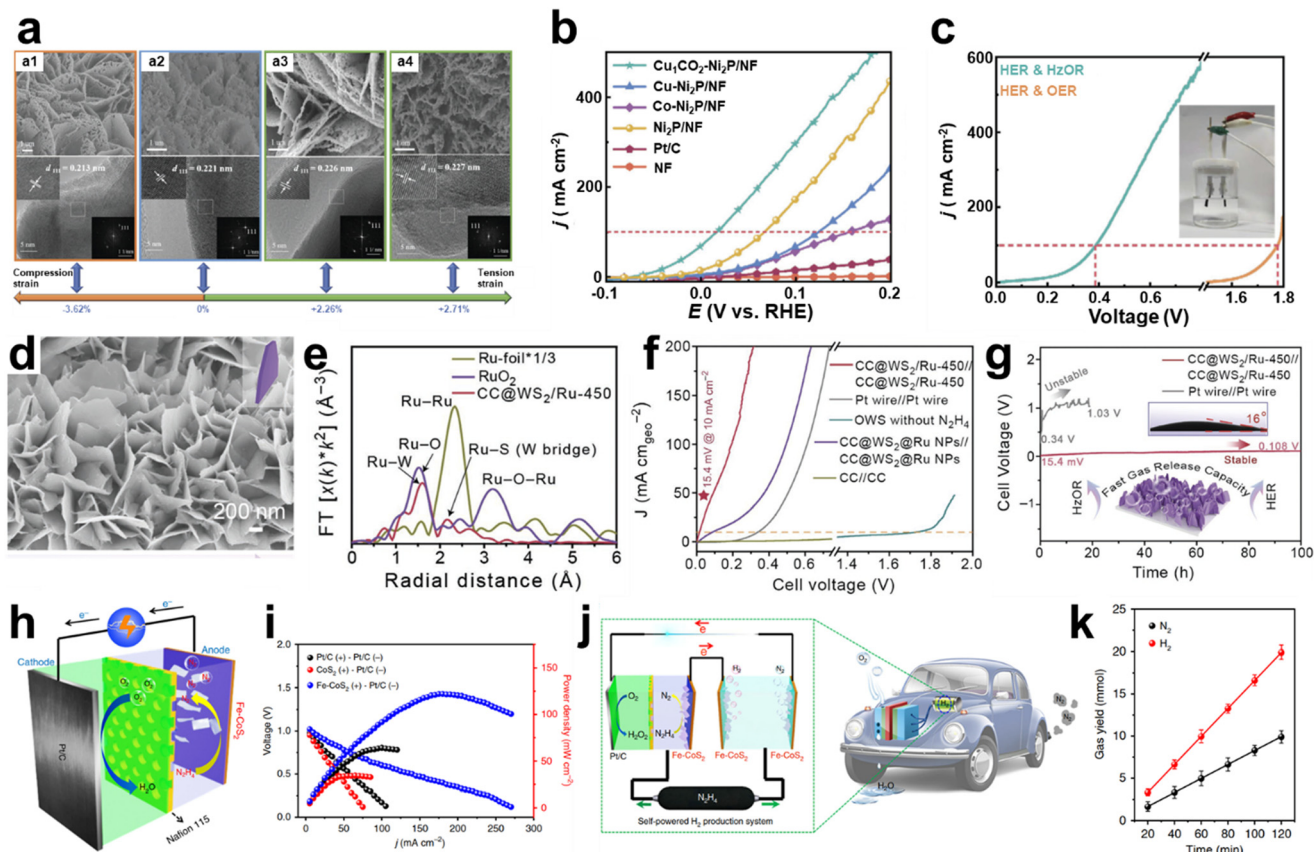
Ind. Chem. Mater., 2025, **3**, 277–310 | **293**

Fig. 11 Hydrazine oxidation reaction (HzOR). (a) SEM (top) and HRTEM (bottom) images of catalysts. a1: Cu_1Co_2-Ni_2P/NF, a2: Ni_2P/NF, a3: Co-Ni_2P/NF, and a4: Cu-Ni_2P/NF. (b) Polarization curves of various catalysts in 1 M KOH with 0.1 M N_2H_4. (c) Polarization curves of Cu_1Co_2-Ni_2P/NF as both an anode and a cathode in 1 M KOH with or without 0.1 M N_2H_4 (inset: image of the two-electrode electrolyzer). (a–c) Reprinted with permission.[128] Copyright 2023, Wiley-VCH GmbH. (d) SEM image of CC@WS_2/Ru-450. (e) FT-EXAFS spectra of CC@WS_2/Ru-450, RuO_2, and Ru-foil. (f) Polarization curves of CC@WS_2/Ru-450 as both an anode and a cathode in 1 M KOH with or without 0.5 M N_2H_4. (g) Stability test of HzOR-assisted water electrolysis using CC@WS_2/Ru-450||CC@WS_2/Ru-450 and Pt wire||Pt wire (inset: contact angle test). (d–g) Reprinted with permission.[129] Copyright 2022, Wiley-VCH GmbH. (h) Schematic illustration of DHzFCs using Fe-CoS_2 nanosheets as the anode and commercial 40 wt% Pt/C as the cathode with O_2 as the oxidizing reagent. (i) Current density–voltage profiles and current density–power density profiles for the DHzFC. (j) Schematic illustration of a self-powered H_2 production system integrated with DHzFC and OHzS systems. (k) N_2 and H_2 generation in the system with 5.3 M hydrazine. (h–k) Reprinted with permission.[130] Copyright 2018, Springer Nature.

potential of 15.4 mV to achieve 10 mA cm^{-2} in 1 M KOH with 0.5 M hydrazine. When the Ru NPs were used instead of Ru SAs, the potential of 86.6 mV was required to reach 10 mA cm^{-2}. Furthermore, water electrolysis using CC@WS_2/Ru-450||CC@WS_2/Ru-450 required a higher voltage of 1.72 V, indicating a significant electric power saving through the HzOR-assisted water splitting reaction. The continuous operation over 100 h at the current density of 10 mA cm^{-2} revealed the durability of the electrolyzer, showing a slight increase of cell voltage to 0.108 V (Fig. 11g). Li *et al.* immobilized Ru SAs into the oxygen vacancies of urchin-like tungsten trioxide (V_O–WO_3) using galvanostatic methods for the HER and HzOR.[134] They demonstrated the pH-universal HER and HzOR properties of V_O–WO_3: the HER performed in acid, alkaline, and neutral environments required the overpotentials of 17, 34, and 64 mV at 10 mA cm^{-2}, and the HzOR performed in alkaline and neutral environments showed the overpotentials of −58 and 23 mV for achieving a current density of 10 mA cm^{-2}, respectively. HzOR-assisted

overall water splitting on CC@WO_3/Ru-450||CC@WO_3/Ru-450 delivers a current density of 10 mA cm^{-2} at 25 mV in 1 M KOH with 0.5 M hydrazine.

Metal sulfides and selenides are promising electrocatalysts due to their unique electronic structure and electrical conductivity. Zhang *et al.* demonstrated a bifunctional tubular cobalt per selenide ($CoSe_2$) nanosheet electrode using a two-step hydrothermal method for the HzOR and HER.[135] Hydrazine-assisted water electrolysis in 1 M KOH with 0.5 M hydrazine using $CoSe_2$/$CoSe_2$ required a cell voltage of 0.164 V at 10 mA cm^{-2}. Liu *et al.* developed bifunctional Fe-doped CoS_2 nanosheets for the HER and HzOR for direct hydrazine fuel cells (DHzFCs) and hydrazine-assisted water electrolyzers.[130] They investigated the effect of Fe-doping on CoS_2 by comparing the free energy profile of the HzOR using DFT calculations. Fe doping decreased the energy barrier of the rate-determining *N_2H_4 to *N_2H_3 step: 0.88 eV and 0.56 eV for CoS_2 and Fe-CoS_2, respectively. By taking advantage of the high catalytic activity and durability of the HzOR using

Fe-CoS$_2$, the DHzFC consisting of Fe-CoS$_2$ (anode) and Pt/C (cathode) was operated using O$_2$ (Fig. 11h). The maximum power density (p_{max}) of Fe-CoS$_2$, CoS$_2$, and Pt/C using the Pt/C cathode showed 125 mW cm^{-2}, 36 mW cm^{-2}, and 66 mW cm^{-2}, respectively (Fig. 11i). They designed a self-powered H$_2$ production system by integrating an overall hydrazine splitting (OHzS) unit and a DHzFC, as shown in Fig. 11j. The OHzS unit generates H$_2$ and N$_2$ at the anode and cathode using Fe-CoS$_2$, where the generated amounts of H$_2$ and N$_2$ gases are measured using gas chromatography with a linear relationship as the measurement time increases (Fig. 11k). The integrated system showed an H$_2$ evolution rate of 9.95 mmol h^{-1}, a faradaic efficiency of 98%, and 20 h stability at room temperature and ambient pressure. This is a promising approach for H$_2$ production without an external bias.

Aligning with the strategy of constructing heterojunction interfaces, nitride-based HzOR catalysts have gained attention due to their promising catalytic activity and physicochemical stability. Qian *et al.* reported hierarchical Ni$_3$N–Co$_3$N porous nanosheet arrays (Ni$_3$N–Co$_3$N PNAs/NF) as bifunctional catalysts for the HER and OER.[136] The comparison of the most stable configurations between Ni$_3$N, Co$_3$N, and the Ni$_3$N–Co$_3$N heterostructure using DFT-calculated free energy diagrams of the HzOR revealed that the RDS for Ni$_3$N–Co$_3$N had a minimum free energy change, indicating higher HzOR activity than other catalysts. Adjustment of doping on metal nitrides was studied by Liu *et al.*, where bifunctional P, W co-doped Co$_3$N nanowire arrays (PW-Co$_3$N NWA/NF) showed high catalytic activity toward the HzOR and HER, requiring −55 mV and −41 mV for achieving 10 mA cm^{-2}, respectively.[137] Low HzOR potentials of 27 and 127 mV *vs.* RHE are required to achieve high current densities of 200 and 600 mA cm^{-2} in 1 M KOH with 0.1 M hydrazine. Doping of P and W decreased the free energy changes for dehydrogenation of *N$_2$H$_4$ to *N$_2$H$_3$ and *N$_2$H$_2$ to *N$_2$H. Mo-doped Ni$_3$N and Ni heterostructure porous nanosheets grown on Ni foam (Mo-Ni$_3$N/Ni/NF) showed the effects of interface engineering and doping, resulting in a cell voltage of 55 mV to deliver 10 mA cm^{-2} in 1 M KOH with 0.1 M hydrazine.[138]

2.5 Oxidation of higher carbon biomass-derived materials

Besides the utilization of methanol and ethanol, even higher carbon materials derived from biomass waste are also highly applied as an alternative to the OER for efficient hydrogen generation. The application of higher carbon material oxidation for anodic reactions can be advantageous when compared to methanol and ethanol oxidation. First, higher carbon materials have the potential to generate more valuable products, as they have various intermediates during the oxidation process.[139,140] However, the oxidation of methanol and ethanol results in the production of low-value products like formaldehyde and acetaldehyde. In extreme cases, they can be fully oxidized to carbon dioxide, which is environmentally undesirable. For a similar reason, methanol or ethanol oxidation is more vulnerable to CO poisoning of the catalyst when compared to the oxidation reaction of higher carbon materials.[141,142] Among various biomass-derived higher carbon materials, glycerol, 5-hydroxymethylfurfural (HMF) and glucose are intensively investigated due to their efficient coupling with the HER through the low oxidation overpotential and economical potential of their oxidation product. In this section, the reaction pathway of glycerol, HMF and glucose oxidation will be presented with their theoretical superiority over the OER. To focus on the comparative energy efficiency of the hybrid water splitting, studies on biomass oxidation coupled with the HER with a 2-electrode system will be briefly covered. Then, in addition to enhanced energy efficiency, research aimed at economic feasibility by enhanced selectivity for a single, high-value product will be presented.

2.5.1 Glycerol oxidation reaction. Among various alternative reactions for anodic water electrolysis, the glycerol oxidation reaction (GEOR) stands out due to its dual advantage of reducing overpotential and generating commercially valuable products. The hydroxyl groups in glycerol provide multiple reactive sites, allowing the formation of a diverse range of oxidation products.[143,144] This flexibility not only improves the economic feasibility of the process but also underscores the importance of selectively targeting desirable products. By carefully tuning reaction conditions and catalyst properties, it becomes possible to achieve an optimal balance between lowering the anodic overpotential and directing the reaction pathway towards high-value chemicals.

In Fig. 12a, the reaction pathway of the GEOR is presented. Starting from glycerol, each oxidation process can be categorized as C–OH oxidation, C=O oxidation, and oxidative C–C cleavage. As the barriers for oxidation of each middle and terminal hydroxyl group are comparable, oxidation reactions of various pathways become inevitably competitive. The ability to control these competitive pathways is crucial for maximizing both efficiency and selectivity in the GEOR. To elucidate the GEOR mechanism, it is crucial to understand the stepwise transformations occurring during the process. The initial step typically involves the adsorption of glycerol onto the catalyst surface, where the interaction between hydroxyl groups and active sites determines the reaction pathway. Subsequent dehydrogenation leads to the formation of glyceraldehyde or dihydroxyacetone, depending on whether the terminal or middle hydroxyl group is oxidized. These intermediates can further undergo oxidation to yield carboxylic acids, such as glyceric acid and tartronic acid, or cleavage reactions, leading to smaller molecules, including formic acid and oxalic acid. The brief overview of recent studies on various GEOR products are provided in Table 1. According to the table, high faradaic efficiency and current density are achieved for formic acid while those of higher carbon products are relatively moderate. From the perspective of catalysts, transition metals are widely applied for the GEOR with formic acid generation. On the other hand, noble metals are featured to generate high carbon products, provoking the necessity for investigation on the

© 2025 The Author(s). Co-published by the Institute of Process Engineering, Chinese Academy of Sciences and the Royal Society of Chemistry

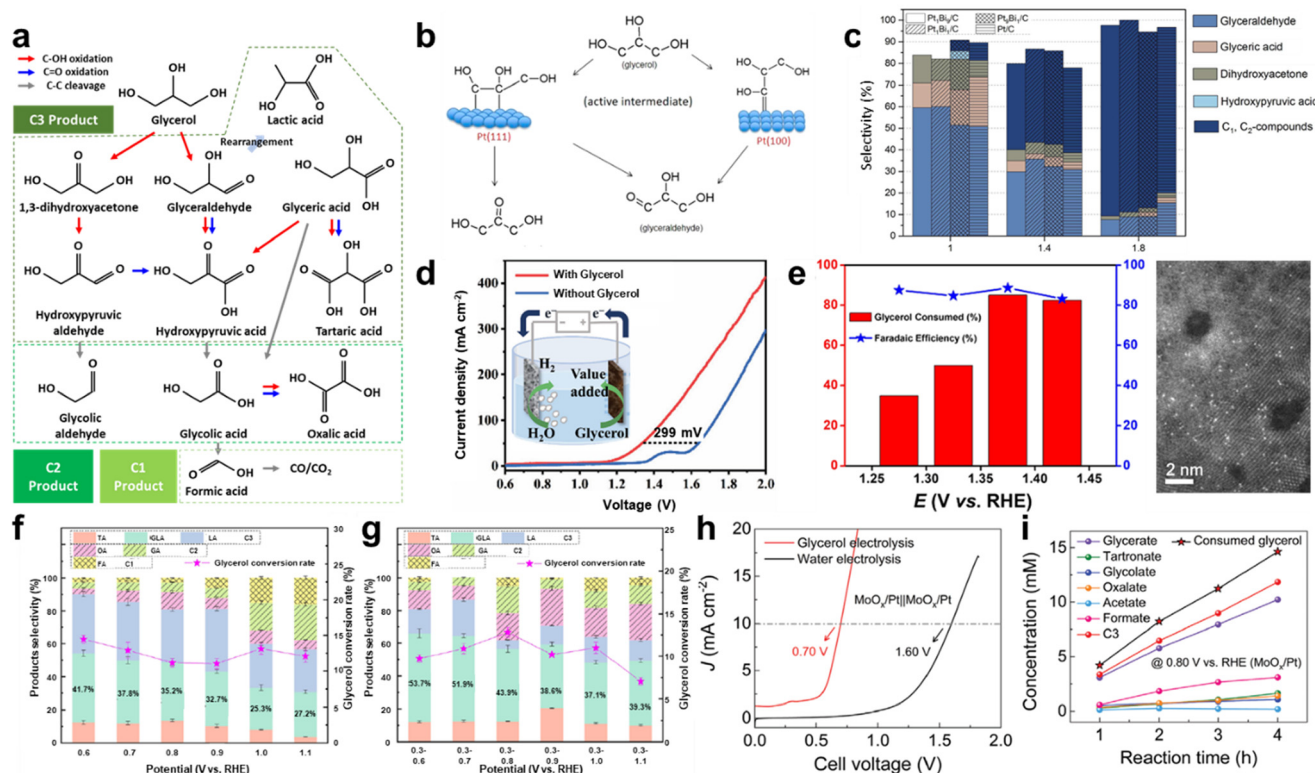*Ind. Chem. Mater.*, 2025, **3**, 277–310 | 295

Fig. 12 Glycerol oxidation reaction (GEOR). (a) Scheme of the GEOR pathway; (b) scheme of the reaction intermediate adsorption in the GEOR on Pt (100) and (111) surfaces. Reprinted with permission.[145] Copyright 2016, American Chemical Society. (c) Product selectivity of direct electrochemical oxidation of 0.1 M glycerol in 0.5 M H_2SO_4 at different electrode potentials. Reprinted with permission.[146] Copyright 2021, Wiley-VCH GmbH. (d) LSV curves (without iR correction) of the overall GOR||HER electrolyzer, which is depicted as an inset. Reprinted with permission.[150] Copyright 2023, Wiley-VCH GmbH. (e) The glycerol conversion and faradaic efficiency of formic acid from Pt_{SA}–NiCo LDH at various potentials. Reprinted with permission.[151] Copyright 2023, Elsevier. Product distribution and conversion rate of the GEOR in the electrolytic modes of (f) CE and (g) PE (E_L = 0.3 V vs. RHE for 0.5 s and EH = 0.6–1.1 V vs. RHE for 0.5 s). (f and g) Reprinted with permission.[152] Copyright 2024, Springer Nature. (h) Comparison of the two-electrode alkaline electrolyzer for the GEOR and water electrolysis. (i) Product concentration and glycerol conversion along with reaction time using the MoO_x/Pt electrode applied at 0.8 V versus RHE based on HPLC analysis. (h and i) Reprinted with permission.[153] Copyright 2021, Wiley-VCH GmbH.

Table 1 Comparison of the applied voltages of GEOR electrocatalysts at various operating current densities for different products

| Anode catalysts | Current density (mA cm^{-2}) | | | | | | Electrolytes (1 M KOH + xM glycerol) | | Ref. |
	1	10	20	100	150	300	Glycerol (M)	Product (FE)	
$NiCo_2O_4$						1.42	0.1	Formic acid (89.9% at 1.42 V)	150
$NiCo_2O_4$/NF					1.6		0.1	Formic acid (97% at 1.6 N)	154
$NiOOH/Ni_3S_2$/NF		1.227					0.1	Formic acid (97.7% at 1.4 V)	155
Pt_{SA}–NiCo LDH/NF				1.37			0.1	Formic acid (88.7% at 1.375 V)	156
$CoMoO_4$		1.105					0.1	Formic acid (90% at 1.26 V)	157
CoNiCuMnMo NPs/CC		1.25					0.1	Formic acid (93.5% at 1.25 V)	158
MnO_2–CuO/CF		1.3					0.1	DHA (54% at 1.3 V)	159
CoO_x	1.57						0.1 (1 M $Na_2B_4O_7$)	DHA (49.4% at 1.5 V)	160
NiOOH	1.62						0.01 (0.75 M H_3BO_3 wt KOH)	DHA (44% at 1.52 V)	161
Co–B_i/CF	1.52						0.1 (0.2 M $Na_2B_4O_7$)	DHA (35% at 1.52 V)	162
MoO_x/Pt		0.7					0.1	Glyceric acid (70% at 0.8 V)	163
Pt/C–Al_2O_3				0.5			1 (1 M NaOH)	Lactic acid (31.3% at 0.5 V)	164
Pt/NiF		0.65					1 (3 M KOH)	Lactic acid (64% at 0.65 V)	165

reaction pathway and mechanism. Followed by such research trends, mechanisms underlying the GEOR have been thoroughly studied on noble metal catalysts. Noble metals, particularly Pt and Au, provide a well-defined platform for understanding the relationship between adsorption structures and reaction pathways. Garcia et al. presented how the glycerol adsorption structure can lead to different product selectivities.[145] According to Fig. 12b, glycerol

adsorbs on the Pt surface in different ways, depending on the surface facet of the Pt catalyst. Specifically, Pt (111) surfaces were shown to favor the oxidation of terminal hydroxyl groups, leading to the formation of glyceraldehyde and other terminal oxidation products. In contrast, Pt (110) and Pt(100) surfaces facilitated the oxidation of secondary hydroxyl groups, resulting in a higher yield of dihydroxyacetone. In addition to the catalyst structure, reaction conditions such as the reaction potential and pH play a significant role in the reaction pathways of the GEOR. Guschakowskin *et al.* investigated the varying behavior of the GEOR with Pt-based catalysts.[146] According to Fig. 12c, the selectivity to various products at different applied potentials on Pt–Bi alloys is presented. At moderate potentials, the reaction pathway is dominated by the C3 products, optimizing selectivity towards these value-added chemicals. However, at higher potentials, further oxidation results in the oxidative C–C bond cleavage and increases the yields of C1 and C2 products. While moderate potentials are ideal for achieving high C3 selectivity, the conversion rate remains limited to about half of the higher potential. This indicates that for the practical application, the balanced potential that ensures both adequate selectivity and a sufficient conversion rate has to be acquired. The influence of pH on the GEOR is another critical factor determining reaction efficiency and selectivity. In addition to the potential, Hamada *et al.* presented that the GEOR kinetics and overpotential are closely correlated to pH.[147] In acidic media, high overpotential was required for the large oxidation current, leading to forming formic acid with multiple C–C bond cleavage. On the other hand, in alkaline media, glycerol exhibited a much higher oxidation current density at low overpotential. The improved oxidation kinetics in alkaline media is contributed by the promotion of the deprotonation step in the basic environment. Kwon *et al.* further presented the product selectivity of the GEOR with noble metals at different pH values based on the new HPLC method.[148] For the Pt catalyst, it sustains the catalytic activity under acidic conditions to basic conditions but lowered pH still significantly deactivates the GEOR, similar to the former study. The trend of major products changes from glyceric acid to formic acid along with the pH decrease. Compared to Pt, high oxidation potential is necessary for the GEOR on Au. In alkaline media, Au shows stronger catalytic activity at high potential than Pt, although the product mainly comprises formic acid. In contrast to its strong activity in alkaline media, Au completely loses its glycerol oxidation activity in acid. Verma *et al.* approached the Au-catalyzed GEOR theoretically to understand the origin of pH dependency.[149] According to the DFT calculations, the GEOR activity and selectivity are controlled by the presence of a surface-bound hydroxyl group. With the environment of experimental onset potential under alkaline conditions, the Au surface has modest OH coverage, optimal for the formation of glyceric acid. Calculated thermodynamic reaction barriers indicate that the surface OH and clean Au site cooperatively facilitate the kinetics and thermodynamics of glyceric acid formation.

Moving beyond the mechanistic studies on noble metal catalysts, recent research has increasingly focused on utilizing transition metal-based catalysts, based on a full system with the cathodic HER. Among transition metals, Ni, Co and their alloys have shown promising activity and stability under alkaline conditions. Luo *et al.* presented a $NiCo_2O_4$ catalyst deposited on Ni foam ($NiCo_2O_4$/NF) for a highly efficient GEOR.[150] In Fig. 12d, the comparison of the two-electrode system LSV curves is presented. For the GEOR and HER coupled system, a 299 mV lower cell voltage (1.34 V) was required at 50 mA cm^{-2} compared to water splitting. High selectivity toward formic acid was also confirmed in the half-cell system, as the faradaic efficiency for formic acid was 89.9% at 1.42 V. The outstanding performance of the $NiCo_2O_4$/NF arises from the oxygen vacancy generation and formation of highly active Ni^{III}–OOH/Co^{III}–OOH species, driven by the substitution of Ni for octahedral Co^{3+}. Wu *et al.* further enhanced the activity of the $NiCo_2O_4$/NF catalyst by controlling the shape of synthesized $NiCo_2O_4$.[166] With the hydrothermal approach, the synthesized $NiCo_2O_4$ has globular cactuses, fully covered with numerous nanowhiskers, which provide large reaction sites. With the hierarchical $NiCo_2O_4$ structure, a faradaic efficiency of 97% toward formate was achieved at 1.6 V. The overpotential in the two-electrode electrolyzer was reduced to 320 mV lower than that of the conventional water electrolysis system. To understand the exact reaction pathway on $NiCo_2O_4$, isotope-labelling NMR analysis was conducted. Two types of glycerol with isotope ^{13}C in different positions were used for the GEOR, and the position of ^{13}C was traced during the reaction pathway to formate. The oxidation route of glycerol was confirmed as glycerol → glyceraldehyde → glycerate → glycollate → formate, and C–C cleavage always occurs to C–C bonding next to the carboxyl group. The suggested reaction pathway is regarded as universal for the similar transition metal-based formate/formic acid generation, which was also observed through *in situ* electrochemical spectroscopy.[167] In addition to the transition metal-based catalysts, Yu *et al.* applied a single atom catalyst to further maximize the energetic efficiency of the GEOR-coupled HER. Using NiCo layered double hydroxide (NiCo LDH) as a base structure, Pt single atoms are anchored at the oxygen vacancies, forming a Pt–O$_5$ penta-coordination.[151] The synthesized Pt single atom-decorated NiCo LDH (Pt$_{SA}$–NiCo LDH) has excellent catalytic properties not only for the GEOR, but also for the HER. Thus, a two-electrode system with the Pt$_{SA}$–NiCo LDH electrode as both the cathode and anode provides the current density of 100 mA cm^{-2} at only 1.37 V. As presented in Fig. 12e, even the faradaic efficiency toward formic acid has a competitive value of 88.7% at 1.37 V. From the DFT simulation, decorated single atom Pt sites are revealed to be a locally charge deficient region, providing HER active sites by lowering the d-band center.

While there have been numerous studies with low overpotential as a hybrid reaction for the HER, mostly their anodic products are limited to formic acid. Various research studies are striving to enhance selectivity for the relatively valuable C3 products, but most studies are still limited to the

half-cell level, hardly considering the cathodic HER performance. The difficulty of achieving high selectivity for C3 products with enough current level for an efficient HER is mainly due to the continuous oxidation of GEOR intermediates to C1 products at oxidative potential. To ensure sufficient current level and C3 product selectivity, a strategy to prevent C–C cleavage through continuous oxidation is required. As part of that strategy, Chen et al. proposed a GEOR at pulsed potential.[152] In Fig. 12f and g, the faradaic efficiency of a Pt–graphite (Pt@G) catalyst through constant-potential electrocatalysis (CE) and pulsed-potential electrocatalysis (PE) is presented. In the potential range, the selectivity for glyceric acid was enhanced and some of the formic acid decreased in the high potential region (1.0–1.1 V) with the application of PE. Here, PE is composed of a high potential section for the GEOR and a low potential section with open circuit potential (OCP). The PE electrolytic mode prevents the overaccumulation of intermediate species at the catalyst surface, releasing the intermediate as a product, and accelerates the re-adsorption of glycerol and hydroxyl groups under OCP for the repetitive GEOR. PE also enhances the current density for the GEOR in the high potential range by avoiding the poisoning of the catalyst surface with intermediates. Yu et al. presented a composite of MoO_x nanosheets and Pt nanoparticles (MoO_x/Pt) as a GEOR/HER bifunctional catalyst which operates at an extremely low cell voltage of 0.7 V with a current density of 10 mA cm^{-2}.[153] As shown in Fig. 12h, the GEOR of MoO_x/Pt reduced the overpotential by 0.9 V compared to conventional water splitting. The point of the study is that such superior energetic efficiency was acquired while ensuring high C3 selectivity. From Fig. 12i, a high concentration of glycerate among various products, which is equivalent to a faradaic efficiency of ~70%, can be confirmed. According to the DFT simulation, MoO_x has the special role of attracting glycerol to the Pt interface, reducing the onset potential of the GEOR. Further, the electronic interaction between MoO_x and Pt improves the reactivity of interfacial sites for both the GEOR and HER.

2.5.2 HMF oxidation reaction and glucose oxidation reaction. Unlike the complex reaction pathways and various products of the GEOR, the oxidation of HMF can be simply presented as Fig. 13a. With the stable furfural ring structure, C–C cleavage hardly occurs during the HMFOR. Therefore, possible pathways of the HMF oxidation reaction (HMFOR) can be divided into the oxidation of alcohol and aldehyde groups, each leads to diformylfuran (DFF) and 5-hydroxymethyl-2-furancarboxylic acid (HMFCA), respectively. The continuous oxidation of DFF and HMFCA forms 5-formyl-2-furancarboxylic acid (FFCA) and finally 2,5-furandicarboxylic acid (FDCA). Between various reaction products, FDCA is regarded as the most valuable chemical feedstock.

Various noble metals are applied for the HMFOR to achieve maximized FDCA selectivity. However, most noble metal catalysts presented inferior FDCA yields when compared to other transition metal-based catalysts. Pt and

Ru catalysts are revealed to convert HMF to DFF, but further oxidation to FDCA is hardly observed.[175,176] Au and Pd catalysts prefer to generate HMFCA, but still oxidation to FDCA is not favorable either.[177,178] To overcome the inferior performance of monometallic noble metal catalysts, Park et al. proposed Au–Pd bimetallic electrodes and fabricated a HER/HMFOR full cell with an optimized cathode and anode.[168] As presented in Fig. 13b, the electrochemical performances of three differently deposited Au–Pd bimetallic films are compared. The layer-by-layer structure of the bimetallic films is fabricated by dipping of ITO glass in Au/Pd-nanosized graphene oxide (nGO) precursor solution, which leads to Au or Pd layer formation through electrostatic interaction between noble metal and nGO. According to Fig. 13b, the FDCA yield apparently increased when the bimetallic film was applied. Particularly, the FDCA selectivity was increased to an ~10% yield in Pd_7/Au_7 and $(AuPd)_7$, while Au_7/Pd_7 has a lower value. Considering that the single Au electrode gives a high HFCA yield, HMF oxidation to HFCA is favorable in the Au site. Therefore, the outer Au region of Pd_7/Au_7 can generate HFCA to be transferred to the Pd layer for further oxidation to FDCA, leading to higher FDCA selectivity.

While noble metal-based catalysts only provide limited selectivity toward FDCA, most studies with transition metal-based catalysts provide excellent FDCA yields comparatively. To compare the intrinsic properties of various transition metal elements, Taitt et al. synthesized NiOOH, CoOOH, and FeOOH and investigated their catalytic properties.[179] Among the three elements, NiOOH was the most efficient catalyst for the HMFOR, achieving 96% faradaic efficiency at 1.47 V vs. RHE. The current density for the HMFOR was also the highest with the NiOOH catalyst. In the case of the CoOOH catalyst, the initiation of the HMFOR was observed at a lower potential than NiOOH, which was confirmed in the indirect HMFOR mediated with $Co(OH)_2$/CoOOH. However, the slow speed of $Co(OH)_2$/CoOOH conversion leads to low current density, which is not practical for application. FeOOH barely showed any catalytic activity for the HMFOR below the onset potential for water oxidation. Wang et al. investigated a strategy to enhance the Ni catalyst for the HMFOR by controlling the different particle aggregation structures.[180] With the electrodeposition of Ni on carbon paper at different current densities, various Ni nanoparticle assemblies of ordered nanoarray, disordered nanoarray and random aggregation were fabricated. Among various structures, the ordered nanoarray structure presented the best performance of 99.2% FDCA yield at a potential of 1.36 V. The high performance of the ordered nanoarray is closely related to the activation of Ni particles. The less agglomerated structure of the ordered nanoarray sample provides large interfacial areas between Ni and the aqueous electrolyte, leading to the facile conversion of surface $Ni(OH)_2$ to NiOOH. The high coverage of catalytically active Ni(III) oxyhydroxide promotes the high yield of FDCA at comparatively low potential. Lu et al. proposed alloy catalysts with integrated catalytic sites for the HMFOR based on Co_3O_4.[181] According to the DFT simulation,
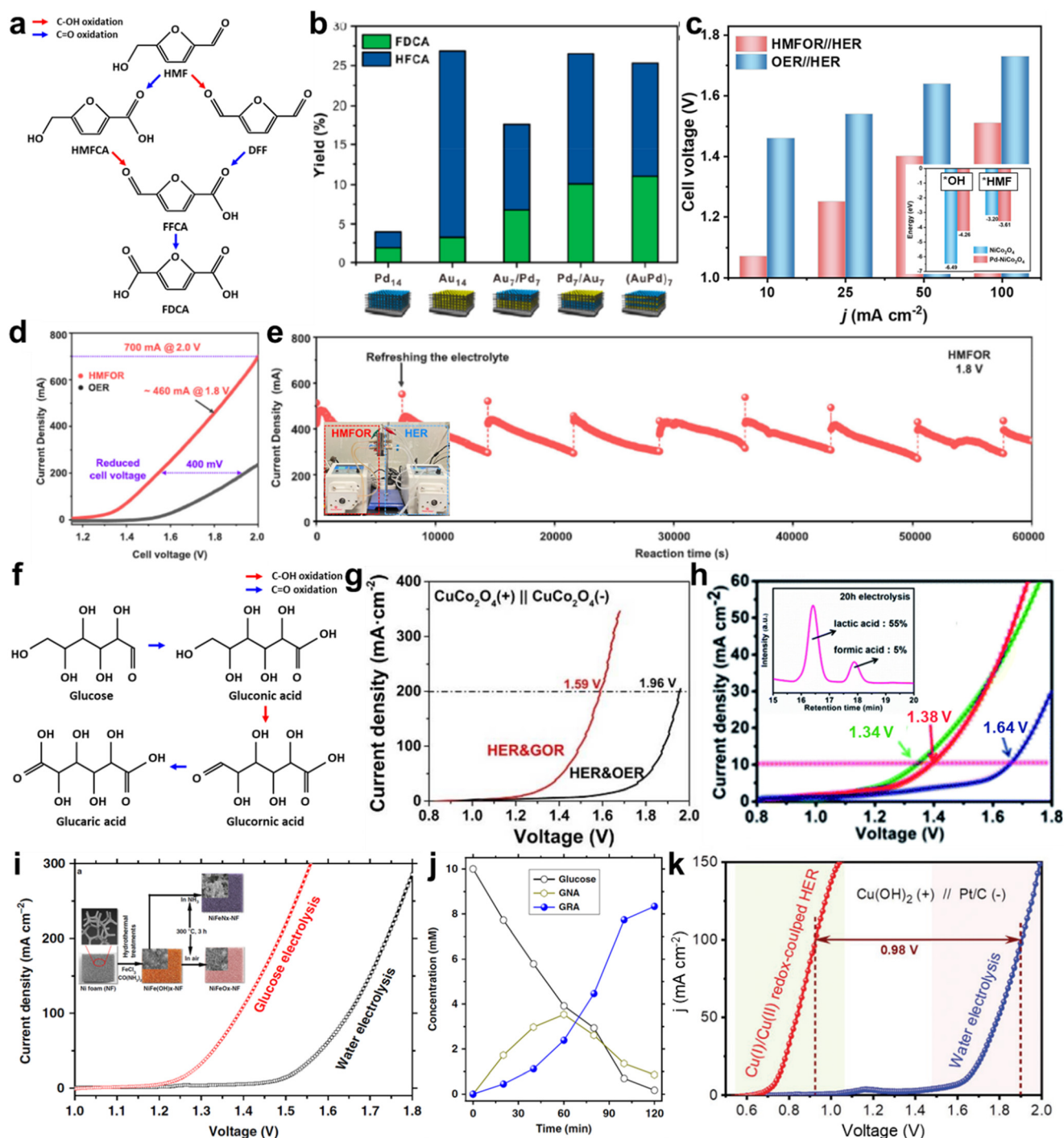
Fig. 13 HMF and glucose oxidation reaction (HMFOR & GOR). (a) Scheme of the HOR pathway; (b) yield of FDCA from each electrode during the electrochemical oxidation. Reprinted with permission.[168] Copyright 2020, American Chemical Society. (c) Comparison of the voltages required to achieve different current densities with *HMF and *OH adsorption energy on NiCo$_2$O$_4$ and Pd-NiCo$_2$O$_4$ as an inset. Reprinted with permission.[169] Copyright 2024, Springer Nature. (d) The LSV curves of the A-Co-Ni$_2$P catalyst in the MEA. (e) Stability measurement for the MEA electrolyzer at 1.8 V over A-Co-Ni$_2$P in 1 M KOH containing 0.1 M HMF. (d and e) Reprinted with permission.[170] Copyright 2024, Springer Nature. (f) Scheme of the GOR pathway. (g) LSV curves in a two-electrode system based on the bifunctional CuCoO$_4$ electrode for glucose electrolysis and water electrolysis. Reprinted with permission.[171] Copyright 2024, The Royal Society of Chemistry. (h) Comparison of polarization curves for water electrolysis, initial glucose electrolysis and after long-term electrolysis with the HPLC analysis result of the yield of oxidation products after 20 h electrolysis as an inset. Reprinted with permission.[172] Copyright 2022, The Royal Society of Chemistry. (i) Comparison of glucose electrolysis and water electrolysis with the anodic NiFeO$_x$-NF and cathodic NiFeN$_x$-NF catalysts (scan rate: 5 mV s^{-1}, glucose concentration: 100 mM, 1 M KOH). (j) Concentration of glucose and oxidation products as a function of time for the chronoamperometric test at 1.3 V *vs.* RHE. (i and j) Reprinted with permission.[173] Copyright 2020, Springer Nature. (k) The LSV profiles in a two-electrode flow cell electrolyzer using Cu(OH)$_2$ as the anodic electrode and Pt/C as the cathodic electrode. Reprinted with permission.[174] Copyright 2021, Wiley-VCH GmbH.

© 2025 The Author(s). Co-published by the Institute of Process Engineering, Chinese Academy of Sciences and the Royal Society of Chemistry

Ind. Chem. Mater., 2025, **3**, 277–310 | **299**

Co_3O_4 catalysts have higher activity for aldehyde oxidation than hydroxyl groups, while NiO has an opposite trend. Therefore, introducing Ni into the tetrahedral sites of Co_3O_4 can generate optimal integrated catalytic sites, favorable for both aldehyde and hydroxyl group oxidation. With the optimization of Ni composition, the $Ni_{0.5}Co_{2.5}O_4$ catalyst achieved a faradaic efficiency of 90.3% for FDCA at 1.5 V vs. RHE. To further enhance the catalytic properties of Ni doped Co_3O_4, Jiang et al. applied a cascade structure of $Pd-NiCo_2O_4$.[169] Based on the Ni-doped Co_3O_4, Pd was loaded by immersing $NiCo_2O_4$ in palladium chloride ethanol solution. The fabricated $Pd-NiCo_2O_4$ can be applied as a bifunctional catalyst for both the OER and HMFOR. As shown in Fig. 13c, $Pd-NiCo_2O_4$ demonstrated remarkable performance in a 2-electrode full cell system, achieving a current density of 100 mA cm^{-2} at a low cell voltage of 1.51 V. FDCA selectivity was also observed as an extremely high faradaic efficiency of 99.6% in the half cell system and ~80% with the full cell system. Both current density and faradaic efficiency were sustained for more than 14 hours for the full cell system. To understand the superior performance of $Pd-NiCo_2O_4$, the role of Pd was understood based on the DFT simulation. From the inset of Fig. 13c, the binding energies of the hydroxyl group and HMF were compared on $NiCo_2O_4$ and $Pd-NiCo_2O_4$. With the additional Pd on $NiCo_2O_4$, the binding energy of HMF increased, while the opposite was observed for the hydroxyl group. The enhanced adsorption behavior of HMF induces facile initiation of the HMFOR and is even beneficial to the desorption in subsequent steps.[182,183] Chen et al. presented low-crystalline Co-doped nickel phosphide (A-Co-Ni$_2$P), achieving industrial current density in a half cell system, which reaches the ampere level.[170] Under the alkaline conditions of 1 M KOH, the current density of 1290 mA cm^{-2} was observed at a potential of 1.6 V, with nearly 100% FDCA yield. According to Fig. 13d, by applying the membrane electrode assembly (MEA) setup for the coupled HMFOR/HER, 200 mA cm^{-2} was acquired at 1.54 V even in a full cell system, which is 400 mV lower than that of the conventional OER coupled system. The operating stability of the HMFOR with MEA was evaluated at a voltage of 1.8 V, and stable electrolysis was maintained for 60 000 s, as shown in Fig. 13e. The electrooxidation of HMF with A-Co-Ni$_2$P was revealed to involve a coupling of electrochemical and non-electrochemical reactions through in situ ATR-FTIR. The electrochemical reaction goes through the dehydrogenation of the aldehyde group of HMF, followed by hydration and oxidation of the hydroxyl group, and finally oxidation to FDCA (HMF → HMFCA → FFCA → FDCA). The non-electrochemical reaction is related to the Cannizzaro reaction of DFF, which occurs under alkaline conditions. Without external potential, DFF rapidly converts to HMF and FFCA by the HMFOR.[184,185]

Similar to the GEOR, the glucose oxidation reaction (GOR) also can have various products during the electrooxidation process. Considering that glucose has a longer carbon chain than glycerol, the possible reaction pathway should be much more complex. Still, as it was the same in the GEOR, the products with a higher number of carbon chains are more desirable, and products without C–C cleavage are preferred.

In this point, representative reaction pathways with preferred intermediates are presented in Fig. 13f. In particular, gluconic acid is considered as one of the most valuable products commercially. However, various studies which coupled the GOR with the HER mostly generate formic acid as the main product due to the difficulty of controlling continuous oxidation with C–C cleavage. Here, studies focused on energetically enhanced HER/GOR coupled systems will be discussed first, followed by approaches that aim for efficient hydrogen generation with valorized GOR products.

Lin et al. investigated the optimal catalyst based on spinel Co_3O_4, by introducing various transition metal elements.[171] With a hydrothermal method, MCo_2O_4 (M = Co, Mn, Cu, Ni, and Zn) catalysts were synthesized on Ni foam and their performances for the GOR were compared. The trend of the catalytic activity was confirmed as Cu > Co > Zn > Ni > Mn and $CuCo_2O_4$ exhibited excellent GOR electrocatalytic activity, which requires 1.31 V vs. RHE for 200 mA cm^{-2} with 98% formic acid faradaic efficiency. According to Fig. 13g, fabricated $CuCo_2O_4$ also presented moderate activity for the HER, and 2-electrode HER/GOR performance with bifunctional $CuCo_2O_4$ could achieve 200 mA cm^{-2} at 1.59 V, which is 370 mV lower than that of the water electrolysis system. The GOR mechanism of $CuCo_2O_4$ was confirmed through in situ Raman spectroscopy and electrochemical impedance spectroscopy (EIS). When the oxidative potential was applied, the Co_3O_4 reconstruction to CoOOH was observed and its amount increased along with potential. However, as the potential entered the region of the GOR, some of the CoOOH remained unchanged, which indicates that reconstructed CoOOH is consumed in the indirect oxidation of glucose. To further enhance the catalytic properties of transition metal introduced Co_3O_4 catalysts, Zhang presented $NiO/NiCo_2O_4$ nanowires on nickel foam ($NiO/NiCo_2O_4/NF$) through a facile solvothermal reaction and calcination. From the DFT simulation, charge transfer from NiO to $NiCo_2O_4$ was observed, generating high oxidation state Ni at the interface, which can optimize the catalytic performance.[186] In addition, the porous nanowire structure of $NiO/NiCo_2O_4/NF$ generates enriched interfacial active sites and promotes the diffusion of active substances. Thanks to the morphology and synergetic interaction between NiO and $NiCo_2O_4$, remarkably low potentials of 0.212 V and 1.128 V vs. RHE for 100 mA cm^{-2} were achieved in the HER and GOR with a 72% yield of formic acid. Li et al. proposed a hybrid catalyst of cobalt nanoparticles supported on nitrogen doped porous carbon (Co@NFC) as a bifunctional HER/GOR catalyst and the generation of lactic acid as the main GOR product.[187] The conversion of glucose to lactic acid can occur in alkaline aqueous solution, starting from the isomerization of glucose. With the Co@NFC bifunctional catalyst, a voltage of 1.56 V was applied to reach 10 mA cm^{-2}, which is 180 mV lower than that of conventional water splitting. While the electrochemical performance is not much noticeable, the valorization of the GOR was achieved through a 45.4% yield of lactic acid. Wu et al. further improved the yield for lactic acid by applying a Co@CoO composite anchored on graphene.[172] To

maximize the catalytic activity, the Mott–Schottky heterojunction of Co@CoO was controlled by exploiting defective MOF precursors during the synthesis process. From Fig. 13h, the synthesized Co@CoO catalyst exhibited a 300 mV lowered GOR potential of 1.34 V for 10 mA cm^{-2} when compared to water electrolysis, and such performance was retained after 80 h of long-term operation. The product yield was observed through HPLC after 20 h of electrolysis, and lactic acid accounts for 55% of the product. Liu *et al.* fabricated a nanostructured NiFe oxide (NiFeO$_x$) anode and NiFe nitride (NiFeN$_x$) cathode assembly for efficient electrochemical glucaric acid and H$_2$ production.[173] The electrolyzer assembled with these two catalysts can deliver 100 mA cm^{-2} at 1.39 V, which is nearly 300 mV lower than that of water electrolysis as shown in Fig. 13i. The anode with NiFeO$_x$ was confirmed to be efficient for glucaric acid (GRA) generation. According to Fig. 13j, as the concentration of glucose decreases with oxidation, gluconic acid (GNA) is first generated and oxidized, which results in accumulation of GRA. Zhang *et al.* presented a glucose-assisted Cu(I)/Cu(II) redox-coupled hydrogen production system, which provided gluconic acid as the main product.[174] The fabricated system was comprised of a Cu(OH)$_2$ anode and a Pt/C cathode separated by an alkaline membrane. According to Fig. 13k, the glucose-assisted Cu(I)/Cu(II) redox-coupled HER exhibited a remarkable decrease of 0.98 V potential compared to water electrolysis for 100 mA cm^{-2}. The liquid product at the anode was also analyzed by HPLC and only gluconic acid was detected, with a faradaic efficiency of 98.7%. The reaction mechanism of glucose on Cu(OH)$_2$ was explained with Raman, XPS and DFT simulation. With the *ex situ* Raman and XPS, it is confirmed that the glucose is oxidized through dehydrogenation, reducing Cu(II) of Cu(OH)$_2$ to Cu(I). The reduced Cu(I) is again oxidized to Cu(II) with oxidative potential, again ready to dehydrogenate glucose. The indirect oxidation of glucose through the Cu(I)/Cu(II) redox couple was compared with direct oxidation through DFT simulation. In the indirect oxidation, glucose dehydrogenation leads to H$_2$O formation with the hydroxyl group of Cu(OH)$_2$, leaving Cu$_2$O, which is also confirmed in the experimental result. With the interaction with Cu, the reaction barrier is highly stabilized to 0.61 eV, while the dehydrogenation without Cu(OH)$_2$ should overcome 1.76 eV.

3 Challenges and perspectives

Substituting the OER with a thermodynamically favorable alternative oxidation reaction is promising for producing H$_2$ with reduced energy consumption. Several advantages of chemical-assisted water electrolysis include: (1) water electrolysis can potentially explode due to the crossover of produced H$_2$ and O$_2$; this explosion risk can be mitigated by replacing the OER with other oxidation reactions. (2) Oxidation of wastewater, which contains ammonia or urea, can effectively remove contaminants while generating H$_2$; (3) organic alternative oxidation reactions can produce value-added products. Despite these advantages, there is still plenty of room to be considered for the industrial application of chemical-
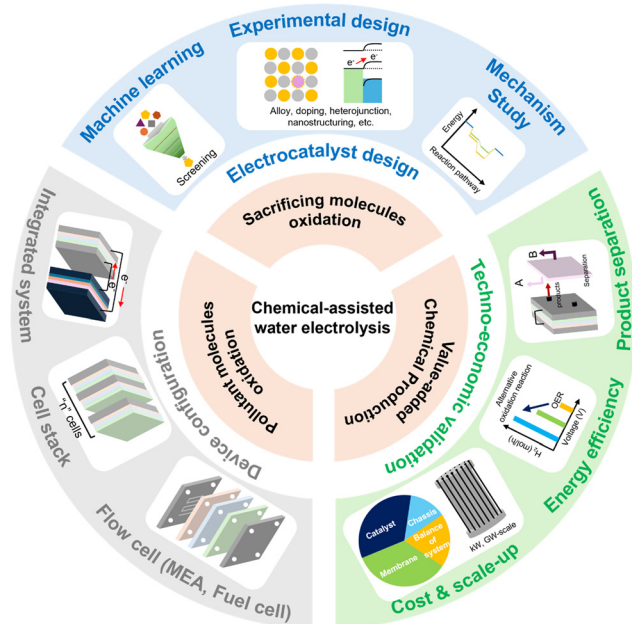

Fig. 14 Schematic illustration of perspectives for chemical-assisted water electrolysis.

assisted water electrolysis as an alternative to conventional water electrolysis, as outlined below (Fig. 14).

Electrocatalyst design – securing the durability of chemical-assisted oxidation reactions with low overpotentials is a key area of interest. Extensive efforts have been made to develop cost-effective, catalytically active electrocatalysts for chemical-assisted water electrolysis, employing strategies such as alloying, nanostructuring, and doping. However, these reactions still require higher overpotentials than their thermodynamic reaction potentials. A notable issue in the AOR is that only Pt demonstrates selectivity toward direct N$_2$ production at low voltage, but it suffers from deactivation due to surface poisoning by *N intermediates. One approach to mitigate this poisoning is operating the AOR with pulse cycling to facilitate the desorption of intermediates, although this is impractical for industrial operations. Another proposed solution is chronopotentiometry measurements at a lower operating voltage, which use partial catalytically active sites. However, this eventually results in complete deactivation due to poisoning of all active sites. Non-noble metal-based catalysts that selectively generate N$_2$ have also been studied by several researchers. However, to date, no catalyst has been found that operates at voltages as low as Pt. Therefore, developing novel catalysts capable of operating at low voltages remains essential. Similarly, the alcohol oxidation reactions using Pt catalysts suffer from CO poisoning, which deteriorates the durability of the reaction. To address this, researchers explore non-precious metal-based catalysts, though these often require high operating potential. Recent research has focused on photoelectrochemical methanol oxidation to reduce energy consumption by harnessing solar energy.[188,189]

© 2025 The Author(s). Co-published by the Institute of Process Engineering, Chinese Academy of Sciences and the Royal Society of Chemistry

Ind. Chem. Mater., 2025, **3**, 277–310 | **301**

The fundamental investigation of chemical-assisted water oxidation reaction catalytic processes is pivotal to understanding the reaction mechanism of catalysts and addressing challenges such as strong adsorption of intermediates, catalyst dissolution, deactivation, and high energy barriers for the reaction. Thermodynamic-based DFT calculations have been instrumental in elucidating reaction mechanisms and identifying active catalytic surfaces. The rapid advancement of artificial intelligence has further enhanced catalyst design for electrochemical reactions by enabling data-driven screening of candidate materials for target reactions.[190] Recent studies have shown the screening of electrocatalysts for chemical-assisted water oxidation reactions.[79,132,191] Further systematic studies are required to screen electrocatalysts with multiple components for alternative water oxidation reactions, particularly multi-electron transfer reactions with ensured interpretability and reliability of machine learning models. In summary, combined high-throughput materials discovery, experimental catalyst development strategies, and materials characterization will pave the way for the design of catalytically active and durable chemical-assisted water oxidation electrocatalysts.

Device design – for industrial applications, achieving high current densities (scale of A cm^{-2}) and long-term stability (>10 000 h) using chemical-assisted water electrolysis is required. The development of MEA, a form of direct assembly of the anode, membrane, and cathode, has made it possible to reduce ohmic and mass transport losses, thereby achieving high operating current density. Studies have demonstrated ampere-scale electrochemical systems for chemical-assisted water electrolysis systems, suggesting a potential pathway toward industrial-scale applications.[170,192,193] Additionally, fuel cell-type devices have been demonstrated, which may require elevated temperatures to achieve high performance.[194,195] As an integrated system, the self-powered H$_2$ production system has been demonstrated by combining direct DHzF and OHzS.[137] However, the chemical-assisted water electrolysis system still requires advanced device design for large-scale, durable operation. To achieve this, further development of durable membranes with low product crossover, along with large-scale and uniform catalyst preparation methods, is required. The design of stack devices should also be followed by dynamic modeling and optimized operation environments.

Techno-economic aspects – meeting cost-effectiveness, energy efficiency, and scalability is crucial for chemical-assisted water electrolysis to serve as an alternative to conventional water electrolysis for hydrogen production at the system scale. Several factors must be considered for industrial applications, given the specific challenges of each reaction. The HzOR, which requires a very low voltage, represents a double-edged sword. On the positive side, the low voltage requirement enables significant savings in electrical energy consumption. However, from another perspective, it can be seen as hydrazine splitting rather than hydrazine-assisted water splitting. As pointed out by Badreldin *et al.*, the electrochemical oxidation of N$_2$H$_4$ generates 2 moles of H$_2$, but the N$_2$H$_4$ synthesis process consumes 3 moles of H$_2$, leading to a net-negative production

of 1 mol H$_2$ per 1 mole of N$_2$H$_4$.[196] In addition, sufficient N$_2$H$_4$, a key reactant for H$_2$ production, should be supplied to the system, increasing overall costs. Therefore, it is necessary to balance the cost reduction from low energy consumption with the offsetting of the resource costs for N$_2$H$_4$. The concept of wastewater treatment or utilizing sacrificial reagents from wastewater should consider the use of low concentration reactants. To date, the use of actual wastewater for oxidation reactions has not been fully realized. In contrast to lab-scale research that uses high-purity, concentrated reactants (*e.g.*, urea, ammonia), actual wastewater may introduce unforeseen issues, such as oxidation of pollutants, catalyst deactivation, stack failure due to impurities, and low operational current density from low reactant concentrations. This requires a pretreatment step and continuous supply of wastewater streams, which consume energy and incur additional costs. The categorization of chemical-assisted water oxidation may involve the generation of gaseous products from urea, ammonia, or hydrazine, or liquid value-added products from organic feedstocks. If multiple products are generated at the anode side, they must be sequestrated for further utilization. In terms of generating value-added products, complete oxidation of alcohols to CO$_2$ has a low economic benefit. Glycerol oxidation reactions face challenges in controlling products due to their susceptibility to further oxidation, resulting in various products with small amounts. The process of separating multiple products also adds extra costs, highlighting the need for optimization of catalyst design, reaction conditions, and selective product formation to enhance economic viability.

In summary, we introduced 5 representative chemical-assisted oxidation reactions using agents (ammonia, alcohol, urea, hydrazine, and glycerol) as promising alternatives to the sluggish OER. In particular, we summarized the recent research on designing electrocatalysts for each reaction, explaining the catalyst design strategies and their effects on the catalytic activity. The various strategies were adjusted for electrocatalyst design, such as alloying, doping, heterostructure formation, control of dimensions from 3D to atomic scales, nanostructuring, *etc.* Overall, the chemical-assisted oxidation reaction and HER demonstrated promising systems with lower cell voltages compared to conventional water electrolysis (OER + HER). Considering the current state of the technology, future efforts should focus on integrating fundamental studies of catalytic reaction mechanisms, advancing electrocatalyst development, and conducting techno-economic assessments to meet the industrial performance requirements. With continued research and electrocatalyst development, chemical-assisted water electrolysis could become an environmentally friendly and energy-efficient technology, significantly contributing to the hydrogen economy.

Data availability

No primary research results, software or code have been included and no new data were generated or analyzed as part of this review.

Conflicts of interest

The authors declare no conflicts of interest.

Acknowledgements

References

1 *The New York Times*, https://www.nytimes.com/2023/12/04/climate/global-fossil-fuel-emissions.html, (accessed December 2024).

2 T. Capurso, M. Stefanizzi, M. Torresi and S. M. Camporeale, Perspective of the role of hydrogen in the 21st century energy transition, *Energy Convers. Manage.*, 2022, **251**, 114898.

3 A. Z. Arsad, M. A. Hannan, A. Q. Al-Shetwi, M. J. Hossain, R. A. Begum, P. J. Ker, F. Salehi and K. M. Muttaqi, Hydrogen electrolyser for sustainable energy production: A bibliometric analysis and future directions, *Int. J. Hydrogen Energy*, 2023, **48**, 4960–4983.

4 S. G. Nnabuife, K. A. Quainoo, A. K. Hamzat, C. K. Darko and C. K. Agyemang, Innovative strategies for combining solar and wind energy with green hydrogen systems, *Appl. Sci.*, 2024, **14**, 9771.

5 Y. Gu, Q. Chen, J. Xue, Z. Tang, Y. Sun and Q. Wu, Comparative techno-economic study of solar energy integrated hydrogen supply pathways for hydrogen refueling stations in China, *Energy Convers. Manage.*, 2020, **223**, 113240.

6 J. H. Lim, K. Kim, J. H. Kang, K. C. Kwon and H. W. Jang, Tailored two-dimensional transition metal dichalcogenides for water electrolysis: Doping, defect, phase, and heterostructure, *ChemElectroChem*, 2024, **11**, e202300614.

7 Z. Li, L. Sheng, R. Deng, Z. Zheng, P. Hou, M. Chen, Z. Ma, K. Sun, Y. Wang, Q. Liu, P. Xu, X. Ma and H. Chu, Regulating crystal phase in Ir-Ge interstitials for hydrogen evolution electrocatalysis, *ACS Energy Lett.*, 2023, **8**, 5136–5142.

8 H. Yang, M. Driess and P. W. Menezes, Self-supported electrocatalysts for practical water electrolysis, *Adv. Energy Mater.*, 2021, **11**, 2102074.

9 I. C. Man, H.-Y. Su, F. Calle-Vallejo, H. A. Hansen, J. I. Martínez, N. G. Inoglu, J. Kitchin, T. F. Jaramillo, J. K. Nørskov and J. Rossmeisl, Universality in oxygen evolution electrocatalysis on oxide surfaces, *ChemCatChem*, 2011, **3**, 1159–1165.

10 G. F. Swiegers, A. L. Hoang, A. Hodges, G. Tsekouras, C.-Y. Lee, K. Wagner and G. Wallace, Current status of *membraneless* water electrolysis cells, *Curr. Opin. Electrochem.*, 2022, **32**, 100881.

11 F. Arshad, T. ul Haq, I. Hussain and F. Sher, Recent advances in electrocatalysts toward alcohol-assisted, energy-saving hydrogen production, *ACS Appl. Energy Mater.*, 2021, **4**, 8685–8701.

12 K. Veeramani, G. Janani, J. Kim, S. Surendran, J. Lim, S. C. Jesudass, S. Mahadik, H. Lee, T.-H. Kim, J. K. Kim and U. Sim, Hydrogen and value-added products yield from hybrid water electrolysis: A critical review on recent developments, *Renewable Sustainable Energy Rev.*, 2023, **177**, 113227.

13 Y. Jun, J. Bang, S. Hong, S. Young Kim and S. Hyun Ahn, Unveiling facet engineering of ultrathin Pt overlayers for enhanced ammonia oxidation reaction, *Chem. Eng. J.*, 2024, **498**, 155433.

14 C. Bianchini and P. K. Shen, Palladium-based electrocatalysts for alcohol oxidation in half cells and in direct alcohol fuel cells, *Chem. Rev.*, 2009, **109**, 4183–4206.

15 S.-K. Geng, Y. Zheng, S.-Q. Li, H. Su, X. Zhao, J. Hu, H.-B. Shu, M. Jaroniec, P. Chen, Q.-H. Liu and S.-Z. Qiao, Nickel ferrocyanide as a high-performance urea oxidation electrocatalyst, *Nat. Energy*, 2021, **6**, 904–912.

16 L. Zhu, J. Huang, G. Meng, T. Wu, C. Chen, H. Tian, Y. Chen, F. Kong, Z. Chang, X. Cui and J. Shi, Active site recovery and N-N bond breakage during hydrazine oxidation boosting the electrochemical hydrogen production, *Nat. Commun.*, 2023, **14**, 1997.

17 C. Chen, Z. Zhou, J. Liu, B. Zhu, H. Hu, Y. Yang, G. Chen, M. Gao and J. Zhang, Sustainable biomass upgrading coupled with H_2 generation over in-situ oxidized Co_3O_4 electrocatalysts, *Appl. Catal., B*, 2022, **307**, 121209.

18 J.-T. Ren, L. Chen, H.-Y. Wang, W.-W. Tian and Z.-Y. Yuan, Water electrolysis for hydrogen production: from hybrid systems to self-powered/catalyzed devices, *Energy Environ. Sci.*, 2024, **17**, 49–113.

19 S. A. Lee, J. Bu, J. Lee and H. W. Jang, High-entropy nanomaterials for advanced electrocatalysis, *Small Sci.*, 2023, **3**, 2200109.

20 T.-G. Vo, C.-C. Kao, J.-L. Kuo, C. Chiu and C.-Y. Chiang, Unveiling the crystallographic facet dependence of the photoelectrochemical glycerol oxidation on bismuth vanadate, *Appl. Catal., B*, 2020, **278**, 119303.

21 Y. Kuang, W. Qiao, S. Wang, F. Yang and L. Feng, Doping and interfacial engineering of $MoSe_2$ nanosheets by NH_3 plasma promoted Pt for methanol electrolysis, *ACS Mater. Lett.*, 2024, **6**, 1722–1731.

22 Z. Li, J. Li, Z. Zheng, K. Jiang, T. Zheng, D. Wang, H. Wei, Z. Shi, X. Li and H. Chu, Roles of hydroxyl and oxygen vacancy of $CeO_2 \cdot xH_2O$ in Pd-catalyzed ethanol electro-oxidation, *Sci. China: Chem.*, 2022, **65**, 877–884.

23 Y. Kuang, M. Li, L. Fu and L. Feng, Deciphering promotion of MoP over MoC in Pt catalysts for methanol-assisted water splitting reaction, *J. Colloid Interface Sci.*, 2025, **679**, 921–929.

24 L. Fan, Y. Ji, G. Wang, J. Chen, K. Chen, X. Liu and Z. Wen, High entropy alloy electrocatalytic electrode toward alkaline glycerol valorization coupling with acidic hydrogen production, *J. Am. Chem. Soc.*, 2022, **144**, 7224–7235.

25 K. Hou, S. Zhang, P. Yin, T. Liu, Y. Cao, M. Wang, W. Zhan and L. Wu, Zinc vaporization induced formation of desired Ni nanoparticles coated with ultrathin carbon shells for efficient electrocatalytic H_2 production coupling with

© 2025 The Author(s). Co-published by the Institute of Process Engineering, Chinese Academy of Sciences and the Royal Society of Chemistry

Ind. Chem. Mater., 2025, **3**, 277–310 | **303**

methanol upgrading, *ACS Appl. Mater. Interfaces*, 2024, **16**, 52326–52338.

26 F. Si, J. Liu, Y. Zhang, B. Zhao, Y. Liang, X. Wu, X. Kang, X. Yang, J. Zhang, X.-Z. Fu and J.-L. Luo, Surface spin enhanced high stable NiCo$_2$S$_4$ for energy-saving production of H$_2$ from water/methanol coelectrolysis at high current density, *Small*, 2023, **19**, 2205257.

27 M. He, C. Feng, T. Liao, S. Hu, H. Wu and Z. Sun, Low-cost Ni$_2$P/Ni$_{0.96}$S heterostructured bifunctional electrocatalyst toward highly efficient overall urea-water electrolysis, *ACS Appl. Mater. Interfaces*, 2020, **12**, 2225–2233.

28 D. M. Fadzillah, S. K. Kamarudin, M. A. Zainoodin and M. S. Masdar, Critical challenges in the system development of direct alcohol fuel cells as portable power supplies: An overview, *Int. J. Hydrogen Energy*, 2019, **44**, 3031–3054.

29 S. P. S. Badwal, S. Giddey, A. Kulkarni, J. Goel and S. Basu, Direct ethanol fuel cells for transport and stationary applications – A comprehensive review, *Appl. Energy*, 2015, **145**, 80–103.

30 A. M. Sheikh, K. E.-A. Abd-Alftah and C. F. Malfatti, On reviewing the catalyst materials for direct alcohol fuel cells (DAFCs), *J. Multidiscip. Eng. Sci. Technol.*, 2014, **1**, N42350050.

31 X. Liu, Y. Han, Y. Guo, X. Zhao, D. Pan, K. Li and Z. Wen, Electrochemical hydrogen generation by oxygen evolution reaction-alternative anodic oxidation reactions, *Adv. Energy Sustainability Res.*, 2022, **3**, 2200005.

32 Z. Jusys, J. Kaiser and R. J. Behm, Methanol electrooxidation over Pt/C fuel cell catalysts: Dependence of product yields on catalyst loading, *Langmuir*, 2003, **19**, 6759–6769.

33 D. S. Mekazni, R. M. Arán-Ais, A. Ferre-Vilaplana and E. Herrero, Why methanol electro-oxidation on platinum in water takes place only in the presence of adsorbed OH, *ACS Catal.*, 2022, **12**, 1965–1970.

34 B. Zhu, B. Dong, F. Wang, Q. Yang, Y. He, C. Zhang, P. Jin and L. Feng, Unraveling a bifunctional mechanism for methanol-to-formate electro-oxidation on nickel-based hydroxides, *Nat. Commun.*, 2023, **14**, 1686.

35 L. E. Heim, H. Konnerth and M. H. G. Prechtl, Future perspectives for formaldehyde: Pathways for reductive synthesis and energy storage, *Green Chem.*, 2017, **19**, 2347–2355.

36 S. Jones, K. Tedsree, M. Sawangphruk, J. S. Foord, J. Fisher, D. Thompsett and S. C. E. Tsang, Promotion of direct methanol electro-oxidation by Ru terraces on Pt by using a reversed spillover mechanism, *ChemCatChem*, 2010, **2**, 1089–1095.

37 G. Hou, J. Parrondo, V. Ramani and J. Prakash, Kinetic and mechanistic investigation of methanol oxidation on a smooth polycrystalline Pt surface, *J. Electrochem. Soc.*, 2013, **161**, F252.

38 S. Li, Z. Fan, Y. Li, Y. Zhang, Y. Zhao, J. Zhao, J. Zhang and Z. Wang, Efficient catalysis for acidic methanol oxidation: Exploration of a low-platinum quaternary alloy catalyst via a two-step method, *Chem. Eng. J.*, 2024, **500**, 156355.

39 Y.-T. Kim, K. Ohshima, K. Higashimine, T. Uruga, M. Takata, H. Suematsu and T. Mitani, Fine size control of platinum on carbon nanotubes: From single atoms to clusters, *Angew. Chem., Int. Ed.*, 2006, **45**, 407–411.

40 X. Chen, M.-M. Liang, J. Xu, H.-L. Sun, C. Wang, J. Wei, H. Zhang, W.-M. Yang, Z.-L. Yang, J.-J. Sun, Z.-Q. Tian and J.-F. Li, Unveiling the size effect of Pt-on-Au nanostructures on CO and methanol electrooxidation by in situ electrochemical SERS, *Nanoscale*, 2020, **12**, 5341–5346.

41 J. Ruan, Y. Chen, G. Zhao, P. Li, B. Zhang, Y. Jiang, T. Ma, H. Pan, S. X. Dou and W. Sun, Cobalt single atoms enabling efficient methanol oxidation reaction on platinum anchored on nitrogen-doped carbon, *Small*, 2022, **18**, 2107067.

42 Y. Hao, D. Yu, S. Zhu, C.-H. Kuo, Y.-M. Chang, L. Wang, H.-Y. Chen, M. Shao and S. Peng, Methanol upgrading coupled with hydrogen product at large current density promoted by strong interfacial interactions, *Energy Environ. Sci.*, 2023, **16**, 1100–1110.

43 Y. Kuang, W. Qiao, S. Wang, F. Yang and L. Feng, Doping and interfacial engineering of MoSe$_2$ nanosheets by NH$_3$ plasma promoted Pt for methanol electrolysis, *ACS Mater. Lett.*, 2024, **6**, 1722–1731.

44 Y. Zhou, Q. Wang, X. Tian and L. Feng, Efficient bifunctional catalysts of CoSe/N-doped carbon nanospheres supported Pt nanoparticles for methanol electrolysis of hydrogen generation, *Nano Res.*, 2022, **15**, 8936–8945.

45 S. Zhang, Z. Zeng, Q. Li, B. Huang, X. Zhang, Y. Du and C.-H. Yan, Lanthanide electronic perturbation in Pt–Ln (La, Ce, Pr and Nd) alloys for enhanced methanol oxidation reaction activity, *Energy Environ. Sci.*, 2021, **14**, 5911–5918.

46 H. Li, Y. Han, H. Zhao, W. Qi, D. Zhang, Y. Yu, W. Cai, S. Li, J. Lai, B. Huang and L. Wang, Fast site-to-site electron transfer of high-entropy alloy nanocatalyst driving redox electrocatalysis, *Nat. Commun.*, 2020, **11**, 5437.

47 D. Majumdar and S. K. Bhattacharya, Recent developments of methanol electrooxidation using nickel-based nanocatalysts, *ChemistrySelect*, 2022, **7**, e202201807.

48 L. Li, W. Gao, M. Lei and D. Wen, Alkali-induced transformation of Ni-MOF into Ni(OH)$_2$ nanostructured flowers for efficient electrocatalytic methanol oxidation reaction, *Chem. – Eur. J.*, 2021, **27**, 10966–10972.

49 W. Yang, X. Yang, J. Jia, C. Hou, H. Gao, Y. Mao, C. Wang, J. Lin and X. Luo, Oxygen vacancies confined in ultrathin nickel oxide nanosheets for enhanced electrocatalytic methanol oxidation, *Appl. Catal., B*, 2019, **244**, 1096–1102.

50 K. Hou, S. Zhang, P. Yin, T. Liu, Y. Cao, M. Wang, W. Zhan and L. Wu, Zinc vaporization induced formation of desired Ni nanoparticles coated with ultrathin carbon shells for efficient electrocatalytic H$_2$ production coupling with methanol upgrading, *ACS Appl. Mater. Interfaces*, 2024, **16**, 52326–52338.

51 Y. Qin, H. Huang, W. Yu, H. Zhang, Z. Li, Z. Wang, J. Lai, L. Wang and S. Feng, Porous PdWM (M = Nb, Mo and Ta) trimetallene for high C1 selectivity in alkaline ethanol oxidation reaction, *Adv. Sci.*, 2022, **9**, 2103722.

52 C. Liang, R. Zhao, T. Chen, Y. Luo, J. Hu, P. Qi and W. Ding, Recent approaches for cleaving the C–C bond during ethanol electro-oxidation reaction, *Adv. Sci.*, 2024, **11**, 2308958.

53 S. C. S. Lai, S. E. F. Kleijn, F. T. Z. Öztürk, V. C. van Rees Vellinga, J. Koning, P. Rodriguez and M. T. M. Koper, Effects of electrolyte pH and composition on the ethanol electro-oxidation reaction, *Catal. Today*, 2010, **154**, 92–104.

54 X. Fu, C. Wan, Y. Huang and X. Duan, Noble metal based electrocatalysts for alcohol oxidation reactions in alkaline media, *Adv. Funct. Mater.*, 2022, **32**, 2106401.

55 Z.-Y. Li, J. Zhou, L.-S. Tang, X.-P. Fu, H. Wei, M. Xue, Y.-L. Zhao, C.-J. Jia, X.-M. Li, H.-B. Chu and Y. Li, Hydroxyl-rich ceria hydrate nanoparticles enhancing the alcohol electrooxidation performance of Pt catalysts, *J. Mater. Chem. A*, 2018, **6**, 2318–2326.

56 H.-F. Wang and Z.-P. Liu, Comprehensive mechanism and structure-sensitivity of ethanol oxidation on platinum: New transition-state searching method for resolving the complex reaction network, *J. Am. Chem. Soc.*, 2008, **130**, 10996–11004.

57 B. Pierozynski, On the ethanol electrooxidation reaction on catalytic surfaces of Pt in 0.1 M NaOH, *Int. J. Electrochem. Sci.*, 2012, **7**, 4261–4271.

58 G. Liu, W. Zhou, Y. Ji, B. Chen, G. Fu, Q. Yun, S. Chen, Y. Lin, P.-F. Yin, X. Cui, J. Liu, F. Meng, Q. Zhang, L. Song, L. Gu and H. Zhang, Hydrogen-intercalation-induced lattice expansion of Pd@Pt core–shell nanoparticles for highly efficient electrocatalytic alcohol oxidation, *J. Am. Chem. Soc.*, 2021, **143**, 11262–11270.

59 W. Yan, G. Li, S. Cui, G.-S. Park, R. Oh, W. Chen, X. Cheng, J.-M. Zhang, W. Li, L.-F. Ji, O. Akdim, X. Huang, H. Lin, J. Yang, Y.-X. Jiang and S.-G. Sun, Ga-modification near-surface composition of Pt–Ga/C catalyst facilitates high-efficiency electrochemical ethanol oxidation through a C2 intermediate, *J. Am. Chem. Soc.*, 2023, **145**, 17220–17231.

60 Y. Wang, M. Zheng, Y. Li, C. Ye, J. Chen, J. Ye, Q. Zhang, J. Li, Z. Zhou, X.-Z. Fu, J. Wang, S.-G. Sun and D. Wang, p–d Orbital hybridization induced by a monodispersed Ga site on a Pt$_3$Mn nanocatalyst boosts ethanol electrooxidation, *Angew. Chem., Int. Ed.*, 2022, **61**, e202115735.

61 Z. Li, S. Ning, J. Xu, J. Zhu, Z. Yuan, Y. Wu, J. Chen, F. Xie, Y. Jin, N. Wang, H. Meng and S. Sun, In situ electrochemical activation of Co(OH)$_2$@Ni(OH)$_2$ heterostructures for efficient ethanol electrooxidation reforming and innovative zinc–ethanol–air batteries, *Energy Environ. Sci.*, 2022, **15**, 5300–5312.

62 X. Tan, S. Chen, D. Yan, R. Du, Q. Zhong, L. Liao, Z. Tang and F. Zeng, Recent advances in Ni-based catalysts for the electrochemical oxidation of ethanol, *J. Energy Chem.*, 2024, **98**, 588–614.

63 X. Chi, L. Gao, W. Zhou, Y. Zhang and T. Hu, Enhanced electrocatalytic performance of 2D Ni-MOF for ethanol oxidation reaction by loading carbon dots, *J. Solid State Chem.*, 2022, **311**, 123094.

64 H. Wang, A. Guan, J. Zhang, Y. Mi, S. Li, T. Yuan, C. Jing, L. Zhang, L. Zhang and G. Zheng, Copper-doped nickel oxyhydroxide for efficient electrocatalytic ethanol oxidation, *Chin. J. Catal.*, 2022, **43**, 1478–1484.

65 S. A. Lee, M. G. Lee and H. W. Jang, Catalysts for electrochemical ammonia oxidation: Trend, challenge, and promise, *Sci. China Mater.*, 2022, **65**, 3334–3352.

66 C. Zhong, W. B. Hu and Y. F. Cheng, Recent advances in electrocatalysts for electro-oxidation of ammonia, *J. Mater. Chem. A*, 2013, **1**, 3216–3238.

67 H. Mashhadimoslem, M. Safarzadeh Khosrowshahi, M. Delpisheh, C. Convery, M. Rezakazemi, T. M. Aminabhavi, M. Kamkar and A. Elkamel, Green ammonia to hydrogen: Reduction and oxidation catalytic processes, *Chem. Eng. J.*, 2023, **474**, 145661.

68 Q. Qian, Y. Zhu, N. Ahmad, Y. Feng, H. Zhang, M. Cheng, H. Liu, C. Xiao, G. Zhang and Y. Xie, Recent advancements in electrochemical hydrogen production via hybrid water splitting, *Adv. Mater.*, 2024, **36**, 2306108.

69 H. Liu, X. Xu, D. Guan and Z. Shao, Minireview on the electrocatalytic ammonia oxidation reaction for hydrogen production and sewage treatment, *Energy Fuels*, 2024, **38**, 919–931.

70 S. Cohen, S. Johnston, C. K. Nguyen, T. D. Nguyen, D. A. Hoogeveen, D. V. Zeil, S. Giddey, A. N. Simonov and D. R. MacFarlane, A CoO$_x$H$_y$/β-NiOOH electrocatalyst for robust ammonia oxidation to nitrite and nitrate, *Green Chem.*, 2023, **25**, 7157–7165.

71 H. G. Oswin and M. Salomon, The anodic oxidation of ammonia at platinum black electrodes in aqueous KOH electrolyte, *Can. J. Chem.*, 1963, **41**, 1686–1694.

72 H. Gerischer and A. Mauerer, Untersuchungen zur anodischen oxidation von ammoniak an platin-elektroden, *J. Electroanal. Chem. Interfacial Electrochem.*, 1970, **25**, 421–433.

73 N. M. Adli, H. Zhang, S. Mukherjee and G. Wu, Review—Ammonia oxidation electrocatalysis for hydrogen generation and fuel cells, *J. Electrochem. Soc.*, 2018, **165**, J3130.

74 A. C. A. de Vooys, M. T. M. Koper, R. A. van Santen and J. A. R. van Veen, The role of adsorbates in the electrochemical oxidation of ammonia on noble and transition metal electrodes, *J. Electroanal. Chem.*, 2001, **506**, 127–137.

75 Y. Yang, J. Kim, H. Jo, A. Seong, M. Lee, H.-K. Min, M. Seo, Y. Choi and G. Kim, A rigorous electrochemical ammonia electrolysis protocol with in operando quantitative analysis, *J. Mater. Chem. A*, 2021, **9**, 11571–11579.

76 J. Liu, Z. Liu, H. Wang, B. Liu, N. Zhao, C. Zhong and W. Hu, Designing nanoporous coral-like Pt nanowires architecture for methanol and ammonia oxidation reactions, *Adv. Funct. Mater.*, 2022, **32**, 2110702.

77 F. J. Vidal-Iglesias, J. Solla-Gullón, V. Montiel, J. M. Feliu and A. Aldaz, Screening of electrocatalysts for direct ammonia fuel cell: Ammonia oxidation on PtMe (Me: Ir, Rh, Pd, Ru) and preferentially oriented Pt(100) nanoparticles, *J. Power Sources*, 2007, **171**, 448–456.

© 2025 The Author(s). Co-published by the Institute of Process Engineering, Chinese Academy of Sciences and the Royal Society of Chemistry

Ind. Chem. Mater., 2025, **3**, 277–310 | **305**

78 M. H. M. T. Assumpção, R. M. Piasentin, P. Hammer, R. F. B. De Souza, G. S. Buzzo, M. C. Santos, E. V. Spinacé, A. O. Neto and J. C. M. Silva, Oxidation of ammonia using PtRh/C electrocatalysts: Fuel cell and electrochemical evaluation, *Appl. Catal., B*, 2015, **174–175**, 136–144.

79 H. S. Pillai, Y. Li, S.-H. Wang, N. Omidvar, Q. Mu, L. E. K. Achenie, F. Abild-Pedersen, J. Yang, G. Wu and H. Xin, Interpretable design of Ir-free trimetallic electrocatalysts for ammonia oxidation with graph neural networks, *Nat. Commun.*, 2023, **14**, 792.

80 S. Liu, Y. Jiang, M. Wang, Y. Huan, Y. He, Q. Cheng, Y. Cheng, J. Liu, X. Zhou, T. Qian and C. Yan, Awakening (220) as one more active facet of PtMo alloy via single-atom doping to boost ammonia electrooxidation in direct ammonia fuel cell, *Adv. Funct. Mater.*, 2023, **33**, 2306204.

81 Y. Li, X. Li, H. S. Pillai, J. Lattimer, N. Mohd Adli, S. Karakalos, M. Chen, L. Guo, H. Xu, J. Yang, D. Su, H. Xin and G. Wu, Ternary PtIrNi catalysts for efficient electrochemical ammonia oxidation, *ACS Catal.*, 2020, **10**, 3945–3957.

82 J. Huang, Z. Chen, J. Cai, Y. Jin, T. Wang and J. Wang, Activating copper oxide for stable electrocatalytic ammonia oxidation reaction via in-situ introducing oxygen vacancies, *Nano Res.*, 2022, **15**, 5987–5994.

83 H. Fang, C. Liao, Q. Cai, F. Zhong, L. Lin, C. Chen, Y. Luo and L. Jiang, Tuning surficial atomic configuration of Pt–Ir catalysts for efficient ammonia oxidation and low-temperature direct ammonia fuel cells, *Chem. Eng. Sci.*, 2023, **280**, 118836.

84 X. Lin, X. Zhang, Z. Wang, X. Zhu, J. Zhu, P. Chen, T. Lyu, C. Li, Z. Qun Tian and P. Kang Shen, Hyperbranched concave octahedron of PtIrCu nanocrystals with high-index facets for efficiently electrochemical ammonia oxidation reaction, *J. Colloid Interface Sci.*, 2021, **601**, 1–11.

85 H. Kim, W. Yang, W. H. Lee, M. H. Han, J. Moon, C. Jeon, D. Kim, S. G. Ji, K. H. Chae, K.-S. Lee, J. Seo, H.-S. Oh, H. Kim and C. H. Choi, Operando stability of platinum electrocatalysts in ammonia oxidation reactions, *ACS Catal.*, 2020, **10**, 11674–11684.

86 W. Xu, D. Du, R. Lan, J. Humphreys, D. N. Miller, M. Walker, Z. Wu, J. T. S. Irvine and S. Tao, Electrodeposited NiCu bimetal on carbon paper as stable non-noble anode for efficient electrooxidation of ammonia, *Appl. Catal., B*, 2018, **237**, 1101–1109.

87 H. Shi, J. Tang, W. Yu, M. O. Tadé and Z. Shao, Advances in power generation from ammonia via electrocatalytic oxidation in direct ammonia fuel cells, *Chem. Eng. J.*, 2024, **488**, 150896.

88 S. He, Y. Chen, M. Wang, H. Nuomin, P. Novello, X. Li, S. Zhu and J. Liu, Metal nitride nanosheets enable highly efficient electrochemical oxidation of ammonia, *Nano Energy*, 2021, **80**, 105528.

89 Y.-J. Shih and C.-H. Hsu, Kinetics and highly selective N₂ conversion of direct electrochemical ammonia oxidation in an undivided cell using NiCo oxide nanoparticle as the anode and metallic Cu/Ni foam as the cathode, *Chem. Eng. J.*, 2021, **409**, 128024.

90 H. Zhang, H. Wang, L. Zhou, Q. Li, X. Yang, Y. Wang, M. Zhang and Z. Wu, Efficient and highly selective direct electrochemical oxidation of ammonia to dinitrogen facilitated by NiCu diatomic site catalysts, *Appl. Catal., B*, 2023, **328**, 122544.

91 K. Nagita, Y. Yuhara, K. Fujii, Y. Katayama and M. Nakayama, Ni- and Cu-co-intercalated layered manganese oxide for highly efficient electro-oxidation of ammonia selective to nitrogen, *ACS Appl. Mater. Interfaces*, 2021, **13**, 28098–28107.

92 H. Wang, X. Tong, L. Zhou, Y. Wang, L. Liao, S. Ouyang and H. Zhang, Unique three-dimensional nanoflower-like NiCu electrodes constructed by Co, S co-doping for efficient ammonia oxidation reaction, *Sep. Purif. Technol.*, 2022, **303**, 122293.

93 A. Ashok Kashale, C.-T. Wu, H.-F. Hsu and I.-W. Peter Chen, In-situ monitoring intermediate stages in ammonia oxidation reaction via high performance NiCuBOx-1/NF electrocatalysts, *Chem. Eng. J.*, 2023, **474**, 145907.

94 X. Gao, S. Zhang, P. Wang, M. Jaroniec, Y. Zheng and S.-Z. Qiao, Urea catalytic oxidation for energy and environmental applications, *Chem. Soc. Rev.*, 2024, **53**, 1552–1591.

95 L. Zhang, L. Wang, H. Lin, Y. Liu, J. Ye, Y. Wen, A. Chen, L. Wang, F. Ni, Z. Zhou, S. Sun, Y. Li, B. Zhang and H. Peng, A lattice-oxygen-involved reaction pathway to boost urea oxidation, *Angew. Chem., Int. Ed.*, 2019, **58**, 16820–16825.

96 S. J. Yao, S. K. Wolfson, B. K. Ahn and C. C. Liu, Anodic oxidation of urea and an electrochemical approach to de-ureation, *Nature*, 1973, **241**, 471–472.

97 Z.-P. Wu, X. F. Lu, S.-Q. Zang and X. W. Lou, Non-noble-metal-based electrocatalysts toward the oxygen evolution reaction, *Adv. Funct. Mater.*, 2020, **30**, 1910274.

98 S. Chen, J. Duan, A. Vasileff and S. Z. Qiao, Size fractionation of two-dimensional sub-nanometer thin manganese dioxide crystals towards superior urea electrocatalytic conversion, *Angew. Chem., Int. Ed.*, 2016, **55**, 3804–3808.

99 D. Zhu, H. Zhang, J. Miao, F. Hu, L. Wang, Y. Tang, M. Qiao and C. Guo, Strategies for designing more efficient electrocatalysts towards the urea oxidation reaction, *J. Mater. Chem. A*, 2022, **10**, 3296–3313.

100 C. Liu, P. Wang, B. Hu, X. Liu, R. Huang and G. Zhou, Asymmetric configuration activating lattice oxygen via weakening d-p orbital hybridization for efficient C/N separation in urea overall electrolysis, *J. Energy Chem.*, 2024, **92**, 233–239.

101 D. Zhu, C. Guo, J. Liu, L. Wang, Y. Du and S.-Z. Qiao, Two-dimensional metal–organic frameworks with high oxidation states for efficient electrocatalytic urea oxidation, *Chem. Commun.*, 2017, **53**, 10906–10909.

102 B. K. Boggs, R. L. King and G. G. Botte, Urea electrolysis: Direct hydrogen production from urine, *Chem. Commun.*, 2009, 4859.

103 K. Yang, L. Hao, L. Hou, J. Zhang and J.-H. Yang, Summary and application of Ni-based catalysts for electrocatalytic urea oxidation, *Int. J. Hydrogen Energy*, 2024, **51**, 966–981.

104 Z. Ji, Y. Song, S. Zhao, Y. Li, J. Liu and W. Hu, Pathway manipulation via Ni, Co, and V ternary synergism to realize high efficiency for urea electrocatalytic oxidation, *ACS Catal.*, 2022, **12**, 569–579.

105 H. Jiang, J. Xia, L. Jiao, X. Meng, P. Wang, C.-S. Lee and W. Zhang, Ni single atoms anchored on N-doped carbon nanosheets as bifunctional electrocatalysts for urea-assisted rechargeable Zn-air batteries, *Appl. Catal., B*, 2022, **310**, 121352.

106 G. Zhan, L. Hu, H. Li, J. Dai, L. Zhao, Q. Zheng, X. Zou, Y. Shi, J. Wang, W. Hou, Y. Yao and L. Zhang, Highly selective urea electrooxidation coupled with efficient hydrogen evolution, *Nat. Commun.*, 2024, **15**, 5918.

107 L. Wang, Y. Zhu, Y. Wen, S. Li, C. Cui, F. Ni, Y. Liu, H. Lin, Y. Li, H. Peng and B. Zhang, Regulating the local charge distribution of Ni active sites for the urea oxidation reaction, *Angew. Chem., Int. Ed.*, 2021, **60**, 10577–10582.

108 H. Sun, J. Liu, G. Chen, H. Kim, S. Kim, Z. Hu, J. Chen, S. Haw, F. Ciucci and W. Jung, Hierarchical structure of CuO nanowires decorated with Ni(OH)$_2$ supported on Cu foam for hydrogen production via urea electrocatalysis, *Small Methods*, 2022, **6**, 2101017.

109 N. Chen, Y.-X. Du, G. Zhang, W.-T. Lu and F.-F. Cao, Amorphous nickel sulfoselenide for efficient electrochemical urea-assisted hydrogen production in alkaline media, *Nano Energy*, 2021, **81**, 105605.

110 Z.-Y. Yu, C.-C. Lang, M.-R. Gao, Y. Chen, Q.-Q. Fu, Y. Duan and S.-H. Yu, Ni–Mo–O nanorod-derived composite catalysts for efficient alkaline water-to-hydrogen conversion via urea electrolysis, *Energy Environ. Sci.*, 2018, **11**, 1890–1897.

111 H. Jiang, M. Sun, S. Wu, B. Huang, C. Lee and W. Zhang, Oxygen-incorporated NiMoP nanotube arrays as efficient bifunctional electrocatalysts for urea-assisted energy-saving hydrogen production in alkaline electrolyte, *Adv. Funct. Mater.*, 2021, **31**, 2104951.

112 M. Fang, W. Gao, G. Dong, Z. Xia, S. Yip, Y. Qin, Y. Qu and J. C. Ho, Hierarchical NiMo-based 3D electrocatalysts for highly-efficient hydrogen evolution in alkaline conditions, *Nano Energy*, 2016, **27**, 247–254.

113 D. Liu, T. Liu, L. Zhang, F. Qu, G. Du, A. M. Asiri and X. Sun, High-performance urea electrolysis towards less energy-intensive electrochemical hydrogen production using a bifunctional catalyst electrode, *J. Mater. Chem. A*, 2017, **5**, 3208–3213.

114 M. Li, H. Sun, J. Yang, M. Humayun, L. Li, X. Xu, X. Xue, A. Habibi-Yangjeh, K. Temst and C. Wang, Mono-coordinated metallocene ligands endow metal-organic frameworks with highly efficient oxygen evolution and urea electrolysis, *Chem. Eng. J.*, 2022, **430**, 132733.

115 J. Kim, M. Kim, S. S. Han and K. Cho, Accessible Ni-Fe-oxalate framework for electrochemical urea oxidation with radically enhanced kinetics, *Adv. Funct. Mater.*, 2024, **34**, 2315625.

116 C. Pei, S. Chen, T. Zhao, M. Li, Z. Cui, B. Sun, S. Hu, S. Lan, H. Hahn and T. Feng, Nanostructured metallic glass in a highly upgraded energy state contributing to efficient catalytic performance, *Adv. Mater.*, 2022, **34**, 2200850.

117 C. Li, Y. Liu, Z. Zhuo, H. Ju, D. Li, Y. Guo, X. Wu, H. Li and T. Zhai, Local charge distribution engineered by schottky heterojunctions toward urea electrolysis, *Adv. Energy Mater.*, 2018, **8**, 1801775.

118 C. Wang, H. Lu, Z. Mao, C. Yan, G. Shen and X. Wang, Bimetal Schottky heterojunction boosting energy-saving hydrogen production from alkaline water via urea electrocatalysis, *Adv. Funct. Mater.*, 2020, **30**, 2000556.

119 A. Kumar, X. Liu, J. Lee, B. Debnath, A. R. Jadhav, X. Shao, V. Q. Bui, Y. Hwang, Y. Liu, M. G. Kim and H. Lee, Discovering ultrahigh loading of single-metal-atoms via surface tensile-strain for unprecedented urea electrolysis, *Energy Environ. Sci.*, 2021, **14**, 6494–6505.

120 M. Song, Z. Zhang, Q. Li, W. Jin, Z. Wu, G. Fu and X. Liu, Ni-foam supported Co(OH)F and Co–P nanoarrays for energy-efficient hydrogen production via urea electrolysis, *J. Mater. Chem. A*, 2019, **7**, 3697–3703.

121 H. Yu, S. Zhu, Y. Hao, Y. Chang, L. Li, J. Ma, H. Chen, M. Shao and S. Peng, Modulating local interfacial bonding environment of heterostructures for energy-saving hydrogen production at high current densities, *Adv. Funct. Mater.*, 2023, **33**, 2212811.

122 Z. Wang, W. Liu, Y. Hu, M. Guan, L. Xu, H. Li, J. Bao and H. Li, Cr-doped CoFe layered double hydroxides: Highly efficient and robust bifunctional electrocatalyst for the oxidation of water and urea, *Appl. Catal., B*, 2020, **272**, 118959.

123 J. Kang, F. Yang, C. Sheng, H. Xu, J. Wang, Y. Qing, Y. Wu and X. Lu, CoP nanoparticle confined in P, N Co-doped porous carbon anchored on P-doped carbonized wood fibers with tailored electronic structure for efficient urea electro-oxidation, *Small*, 2022, **18**, 2200950.

124 D. C. Nguyen, T. L. L. Doan, S. Prabhakaran, D. H. Kim, N. H. Kim and J. H. Lee, Rh single atoms/clusters confined in metal sulfide/oxide nanotubes as advanced multifunctional catalysts for green and energy-saving hydrogen productions, *Appl. Catal., B*, 2022, **313**, 121430.

125 T. Y. Burshtein, Y. Yasman, L. Muñoz-Moene, J. H. Zagal and D. Eisenberg, Hydrazine oxidation electrocatalysis, *ACS Catal.*, 2024, **14**, 2264–2283.

126 S. Li, Y. Hou, L. Jiang, G. Feng, Y. Ge and Z. Huang, Progress in hydrazine oxidation-assisted hydrogen production, *Energy Rev.*, 2025, **4**, 100105.

127 Y. Li, J. Zhang, Y. Liu, Q. Qian, Z. Li, Y. Zhu and G. Zhang, Partially exposed RuP$_2$ surface in hybrid structure endows its bifunctionality for hydrazine oxidation and hydrogen evolution catalysis, *Sci. Adv.*, 2020, **6**, eabb4197.

128 C. Feng, M. Lv, J. Shao, H. Wu, W. Zhou, S. Qi, C. Deng, X. Chai, H. Yang, Q. Hu and C. He, Lattice strain engineering of Ni$_2$P enables efficient catalytic hydrazine oxidation-assisted hydrogen production, *Adv. Mater.*, 2023, **35**, 2305598.

129 J. Li, Y. Li, J. Wang, C. Zhang, H. Ma, C. Zhu, D. Fan, Z. Guo, M. Xu, Y. Wang and H. Ma, Elucidating the critical

© 2025 The Author(s). Co-published by the Institute of Process Engineering, Chinese Academy of Sciences and the Royal Society of Chemistry

Ind. Chem. Mater., 2025, **3**, 277–310 | **307**

role of ruthenium single atom sites in water dissociation and dehydrogenation behaviors for robust hydrazine oxidation-boosted alkaline hydrogen evolution, *Adv. Funct. Mater.*, 2022, **32**, 2109439.

130 X. Liu, J. He, S. Zhao, Y. Liu, Z. Zhao, J. Luo, G. Hu, X. Sun and Y. Ding, Self-powered H$_2$ production with bifunctional hydrazine as sole consumable, *Nat. Commun.*, 2018, **9**, 4365.

131 Z. Li, W. Wang, Q. Qian, Y. Zhu, Y. Feng, Y. Zhang, H. Zhang, M. Cheng and G. Zhang, Magic hybrid structure as multifunctional electrocatalyst surpassing benchmark Pt/C enables practical hydrazine fuel cell integrated with energy-saving H$_2$ production, *eScience*, 2022, **2**, 416–427.

132 G. Feng, Y. Pan, D. Su and D. Xia, Constructing fully-active and ultra-active sites in high-entropy alloy nanoclusters for hydrazine oxidation-assisted electrolytic hydrogen production, *Adv. Mater.*, 2024, **36**, 2309715.

133 X. Guan, Q. Wu, H. Li, S. Zeng, Q. Yao, R. Li, H. Chen, Y. Zheng and K. Qu, Identifying the roles of Ru single atoms and nanoclusters for energy-efficient hydrogen production assisted by electrocatalytic hydrazine oxidation, *Appl. Catal., B*, 2023, **323**, 122145.

134 J. Li, C. Zhang, C. Zhang, H. Ma, Y. Yang, Z. Guo, Y. Wang and H. Ma, Electronic configuration of single ruthenium atom immobilized in urchin-like tungsten trioxide towards hydrazine oxidation-assisted hydrogen evolution under wide pH media, *Chem. Eng. J.*, 2022, **430**, 132953.

135 J. Zhang, H. Wang, Y. Tian, Y. Yan, Q. Xue, T. He, H. Liu, C. Wang, Y. Chen and B. Y. Xia, Anodic hydrazine oxidation assists energy-efficient hydrogen evolution over a bifunctional cobalt perselenide nanosheet electrode, *Angew. Chem., Int. Ed.*, 2018, **57**, 7649–7653.

136 Q. Qian, J. Zhang, J. Li, Y. Li, X. Jin, Y. Zhu, Y. Liu, Z. Li, A. El-Harairy, C. Xiao, G. Zhang and Y. Xie, Artificial heterointerfaces achieve delicate reaction kinetics towards hydrogen evolution and hydrazine oxidation catalysis, *Angew. Chem., Int. Ed.*, 2021, **60**, 5984–5993.

137 Y. Liu, J. Zhang, Y. Li, Q. Qian, Z. Li, Y. Zhu and G. Zhang, Manipulating dehydrogenation kinetics through dual-doping Co$_3$N electrode enables highly efficient hydrazine oxidation assisting self-powered H$_2$ production, *Nat. Commun.*, 2020, **11**, 1853.

138 Y. Liu, J. Zhang, Y. Li, Q. Qian, Z. Li and G. Zhang, Realizing the synergy of interface engineering and chemical substitution for Ni$_3$N enables its bifunctionality toward hydrazine oxidation assisted energy-saving hydrogen production, *Adv. Funct. Mater.*, 2021, **31**, 2103673.

139 H. Luo, J. Barrio, N. Sunny, A. Li, L. Steier, N. Shah, I. E. L. Stephens and M. Titirici, Progress and perspectives in photo- and electrochemical-oxidation of biomass for sustainable chemicals and hydrogen production, *Adv. Energy Mater.*, 2021, **11**, 2101180.

140 Y. Li, Z. Dang and P. Gao, High-efficiency electrolysis of biomass and its derivatives: Advances in anodic oxidation reaction mechanism and transition metal-based electrocatalysts, *Nano Sel.*, 2021, **2**, 847–864.

141 Z. Wei, S. Yu and C. Li, Research development of anti-CO poisoning in electrocatalytic methanol oxidation processes: A review, *Catal. Sci. Technol.*, 2024, **14**, 5128–5142.

142 J. Kaur, R. K. Gupta and A. Kumar, Electrocatalytic ethanol oxidation reaction: Recent progress, challenges, and future prospects, *Discover Nano*, 2024, **19**, 137.

143 M. Kumar, B. Meena, A. Yu, C. Sun and S. Challapalli, Advancements in catalysts for glycerol oxidation via photo-/electrocatalysis: A comprehensive review of recent developments, *Green Chem.*, 2023, **25**, 8411–8443.

144 N. Cai, C. Jin, C. Wan and R. Dong, Highly active PdAg/C catalysts for the electrooxidation of propan-1-ol, *J. Electrochem. Soc.*, 2017, **164**, H437.

145 A. C. Garcia, M. J. Kolb, C. Van Nierop, Y. Sanchez, J. Vos, Y. Y. Birdja, Y. Kwon, G. Tremiliosi-Filho and M. T. M. Koper, Strong impact of platinum surface structure on primary and secondary alcohol oxidation during electro-oxidation of glycerol, *ACS Catal.*, 2016, **6**, 4491–4500.

146 M. Guschakowski and U. Schröder, Direct and indirect electrooxidation of glycerol to value-added products, *ChemSusChem*, 2021, **14**, 5216–5225.

147 T. Hamada, A. R. Circelli, H. Inoue, C. A. Randall and E. L. Clark, Investigating the origins of the pH-dependent oxidation of glycerol over platinum using differential electrochemical mass spectrometry, *J. Phys. Chem. C*, 2024, **128**, 10790–10801.

148 Y. Kwon, K. J. P. Schouten and M. T. M. Koper, Mechanism of the catalytic oxidation of glycerol on polycrystalline gold and platinum electrodes, *ChemCatChem*, 2011, **3**, 1176–1185.

149 A. M. Verma, L. Laverdure, M. M. Melander and K. Honkala, Mechanistic origins of the pH dependency in au-catalyzed glycerol electro-oxidation: Insight from first-principles calculations, *ACS Catal.*, 2022, **12**, 662–675.

150 W. Luo, H. Tian, Q. Li, G. Meng, Z. Chang, C. Chen, R. Shen, X. Yu, L. Zhu, F. Kong, X. Cui and J. Shi, Controllable electron distribution reconstruction of spinel NiCo$_2$O$_4$ boosting glycerol oxidation at elevated current density, *Adv. Funct. Mater.*, 2024, **34**, 2306995.

151 H. Yu, W. Wang, Q. Mao, K. Deng, Z. Wang, Y. Xu, X. Li, H. Wang and L. Wang, Pt single atom captured by oxygen vacancy-rich NiCo layered double hydroxides for coupling hydrogen evolution with selective oxidation of glycerol to formate, *Appl. Catal., B*, 2023, **330**, 122617.

152 W. Chen, L. Zhang, L. Xu, Y. He, H. Pang, S. Wang and Y. Zou, Pulse potential mediated selectivity for the electrocatalytic oxidation of glycerol to glyceric acid, *Nat. Commun.*, 2024, **15**, 2420.

153 X. Yu, E. C. dos Santos, J. White, G. Salazar-Alvarez, L. G. M. Pettersson, A. Cornell and M. Johnsson, Electrocatalytic glycerol oxidation with concurrent hydrogen evolution utilizing an efficient MoO/Pt catalyst, *Small*, 2021, **17**, 2104288.

154 G. Wu, X. Dong, J. Mao, G. Li, C. Zhu, S. Li, A. Chen, G. Feng, Y. Song, W. Chen and W. Wei, Anodic glycerol oxidation to formate facilitating cathodic hydrogen

evolution with earth-abundant metal oxide catalysts, *Chem. Eng. J.*, 2023, **468**, 143640.

155 L. Xu, Y. Yang, C. Li, R. Ning, J. Ma, M. Yao, S. Geng and F. Liu, Unveiling the mechanism of electrocatalytic oxidation of glycerol by in-situ electrochemical spectroscopy, *Chem. Eng. J.*, 2024, **481**, 148304.

156 H. Yu, W. Wang, Q. Mao, K. Deng, Z. Wang, Y. Xu, X. Li, H. Wang and L. Wang, Pt single atom captured by oxygen vacancy-rich NiCo layered double hydroxides for coupling hydrogen evolution with selective oxidation of glycerol to formate, *Appl. Catal., B*, 2023, **330**, 122617.

157 X. Yu, R. B. Araujo, Z. Qiu, E. Campos dos Santos, A. Anil, A. Cornell, L. G. M. Pettersson and M. Johnsson, Hydrogen evolution linked to selective oxidation of glycerol over CoMoO$_4$—A theoretically predicted catalyst, *Adv. Energy Mater.*, 2022, **12**, 2103750.

158 L. Fan, Y. Ji, G. Wang, J. Chen, K. Chen, X. Liu and Z. Wen, High entropy alloy electrocatalytic electrode toward alkaline glycerol valorization coupling with acidic hydrogen production, *J. Am. Chem. Soc.*, 2022, **144**, 7224–7235.

159 Z. Huang, H. Ren, J. Guo, Y. Tang, D. Ye, J. Zhang and H. Zhao, High DHA selectivity and low-cost electrode for glycerol oxidation: CuO regulates MnO$_2$ electron density to promote DHA desorption, *Appl. Catal., B*, 2024, **351**, 123986.

160 T.-G. Vo, P.-Y. Ho and C.-Y. Chiang, *Operando* mechanistic studies of selective oxidation of glycerol to dihydroxyacetone over amorphous cobalt oxide, *Appl. Catal., B*, 2022, **300**, 120723.

161 M. K. Goetz, M. T. Bender and K.-S. Choi, Predictive control of selective secondary alcohol oxidation of glycerol on NiOOH, *Nat. Commun.*, 2022, **13**, 5848.

162 X. Huang, Y. Zou and J. Jiang, Electrochemical oxidation of glycerol to dihydroxyacetone in borate buffer: Enhancing activity and selectivity by borate–polyol coordination chemistry, *ACS Sustainable Chem. Eng.*, 2021, **9**, 14470–14479.

163 X. Yu, E. C. dos Santos, J. White, G. Salazar-Alvarez, L. G. M. Pettersson, A. Cornell and M. Johnsson, Electrocatalytic glycerol oxidation with concurrent hydrogen evolution utilizing an efficient MoO/Pt catalyst, *Small*, 2021, **17**, 2104288.

164 H. Luo, M. Xu, S. Liu, G. Tarantino, H. Ye, H. Yadegari, A. Y. Li, C. Hammond, G. Kastlunger, I. E. L. Stephens and M.-M. Titirici, Selective glycerol to lactic acid conversion via a tandem effect between platinum and metal oxides with abundant acid groups, *EES Catal.*, 2025, **3**, 87–96.

165 S. Angizi, M. Nankali, A. Foroozan, J. Park, E. Yelekli Kirici, N. Noor, M. Fefer, Y. Terazono and D. Higgins, 3D bimetallic platinum-nickel electrodes for electro-oxidation of glycerol at ambient conditions, *Adv. Funct. Mater.*, 2024, 2420622.

166 G. Wu, X. Dong, J. Mao, G. Li, C. Zhu, S. Li, A. Chen, G. Feng, Y. Song, W. Chen and W. Wei, Anodic glycerol oxidation to formate facilitating cathodic hydrogen evolution with earth-abundant metal oxide catalysts, *Chem. Eng. J.*, 2023, **468**, 143640.

167 L. Xu, Y. Yang, C. Li, R. Ning, J. Ma, M. Yao, S. Geng and F. Liu, Unveiling the mechanism of electrocatalytic oxidation of glycerol by in-situ electrochemical spectroscopy, *Chem. Eng. J.*, 2024, **481**, 148304.

168 M. Park, M. Gu and B.-S. Kim, Tailorable electrocatalytic 5-hydroxymethylfurfural oxidation and H$_2$ production: Architecture–performance relationship in bifunctional multilayer electrodes, *ACS Nano*, 2020, **14**, 6812–6822.

169 X. Jiang, X. Ma, Y. Yang, Y. Liu, Y. Liu, L. Zhao, P. Wang, Y. Zhang, Y. Lin and Y. Wei, Enhancing the electrocatalytic oxidation of 5-hydroxymethylfurfural through cascade structure tuning for highly stable biomass upgrading, *Nano-Micro Lett.*, 2024, **16**, 275.

170 L. Chen, C. Yu, X. Song, J. Dong, J. Mu and J. Qiu, Integrated electrochemical and chemical system for ampere-level production of terephthalic acid alternatives and hydrogen, *Nat. Commun.*, 2024, **15**, 8072.

171 X. Lin, X. Xue and J. Du, Electrochemical glucose-to-formic acid conversion coupled with alkaline hydrogen production over nanostructured CuCo$_2$O$_4$ catalysts, *J. Mater. Chem. A*, 2024, **12**, 32095–32103.

172 M. Wu, J. Zhao, C. Li and R. Liu, Heterogeneity in a metal–organic framework in situ guides engineering Co@CoO heterojunction for electrocatalytic H$_2$ production in tandem with glucose oxidation, *J. Mater. Chem. A*, 2022, **10**, 4791–4799.

173 W.-J. Liu, Z. Xu, D. Zhao, X.-Q. Pan, H.-C. Li, X. Hu, Z.-Y. Fan, W.-K. Wang, G.-H. Zhao, S. Jin, G. W. Huber and H.-Q. Yu, Efficient electrochemical production of glucaric acid and H$_2$ via glucose electrolysis, *Nat. Commun.*, 2020, **11**, 265.

174 Y. Zhang, B. Zhou, Z. Wei, W. Zhou, D. Wang, J. Tian, T. Wang, S. Zhao, J. Liu, L. Tao and S. Wang, Coupling glucose-assisted Cu(I)/Cu(II) redox with electrochemical hydrogen production, *Adv. Mater.*, 2021, **33**, 2104791.

175 S. R. Kubota and K.-S. Choi, Electrochemical oxidation of 5-hydroxymethylfurfural to 2,5-furandicarboxylic acid (FDCA) in acidic media enabling spontaneous FDCA separation, *ChemSusChem*, 2018, **11**, 2138–2145.

176 R. Latsuzbaia, R. Bisselink, A. Anastasopol, H. van der Meer, R. van Heck, M. S. Yagüe, M. Zijlstra, M. Roelands, M. Crockatt, E. Goetheer and E. Giling, Continuous electrochemical oxidation of biomass derived 5-(hydroxymethyl)furfural into 2,5-furandicarboxylic acid, *J. Appl. Electrochem.*, 2018, **48**, 611–626.

177 D. J. Chadderdon, L. Xin, J. Qi, Y. Qiu, P. Krishna, K. L. More and W. Li, Electrocatalytic oxidation of 5-hydroxymethylfurfural to 2,5-furandicarboxylic acid on supported Au and Pd bimetallic nanoparticles, *Green Chem.*, 2014, **16**, 3778–3786.

178 N. Heidary and N. Kornienko, Operando Raman probing of electrocatalytic biomass oxidation on gold nanoparticle surfaces, *Chem. Commun.*, 2019, **55**, 11996–11999.

179 B. J. Taitt, D.-H. Nam and K.-S. Choi, A comparative study of nickel, cobalt, and iron oxyhydroxide anodes for the electrochemical oxidation of 5-hydroxymethylfurfural to 2,5-furandicarboxylic acid, *ACS Catal.*, 2019, **9**, 660–670.

© 2025 The Author(s). Co-published by the Institute of Process Engineering, Chinese Academy of Sciences and the Royal Society of Chemistry

Ind. Chem. Mater., 2025, **3**, 277–310 | 309

180 J. Wang, W. Zhao, H. Yu, W. Wang, Y. Xu, L.-L. Shen, G.-R. Zhang and D. Mei, Enhanced electrochemical oxidation of 5-hydroxymethylfurfural over tailored nickel nanoparticle assembly, *Appl. Catal., B*, 2024, **353**, 124086.

181 Y. Lu, T. Liu, Y.-C. Huang, L. Zhou, Y. Li, W. Chen, L. Yang, B. Zhou, Y. Wu, Z. Kong, Z. Huang, Y. Li, C.-L. Dong, S. Wang and Y. Zou, Integrated catalytic sites for highly efficient electrochemical oxidation of the aldehyde and hydroxyl groups in 5-hydroxymethylfurfural, *ACS Catal.*, 2022, **12**, 4242–4251.

182 Z. Wang, S. Shen, Z. Lin, W. Tao, Q. Zhang, F. Meng, L. Gu and W. Zhong, Regulating the local spin state and band structure in Ni_3S_2 nanosheet for improved oxygen evolution activity, *Adv. Funct. Mater.*, 2022, **32**, 2112832.

183 Q. Xu, J. Zhang, H. Zhang, L. Zhang, L. Chen, Y. Hu, H. Jiang and C. Li, Atomic heterointerface engineering overcomes the activity limitation of electrocatalysts and promises highly-efficient alkaline water splitting, *Energy Environ. Sci.*, 2021, **14**, 5228–5259.

184 B. You, N. Jiang, X. Liu and Y. Sun, Simultaneous H_2 generation and biomass upgrading in water by an efficient noble-metal-free bifunctional electrocatalyst, *Angew. Chem., Int. Ed.*, 2016, **55**, 9913–9917.

185 B. You, X. Liu, N. Jiang and Y. Sun, A general strategy for decoupled hydrogen production from water splitting by integrating oxidative biomass valorization, *J. Am. Chem. Soc.*, 2016, **138**, 13639–13646.

186 Z. Zhang, X. Liang, J. Li, J. Qian, Y. Liu, S. Yang, Y. Wang, D. Gao and D. Xue, Interfacial engineering of $NiO/NiCo_2O_4$ porous nanofibers as efficient bifunctional catalysts for rechargeable zinc–air batteries, *ACS Appl. Mater. Interfaces*, 2020, **12**, 21661–21669.

187 D. Li, Y. Huang, Z. Li, L. Zhong, C. Liu and X. Peng, Deep eutectic solvents derived carbon-based efficient electrocatalyst for boosting H_2 production coupled with glucose oxidation, *Chem. Eng. J.*, 2022, **430**, 132783.

188 D. Paital, V. Thambi, M. S. Kutwal and S. Khatua, Porous plasmonic Au–Ag@Au nanostructures for photoelectrochemical methanol oxidation, *ACS Appl. Nano Mater.*, 2022, **5**, 13286–13294.

189 S. Mohajernia, S. Hejazi, P. Andryskova, G. Zoppellaro, O. Tomanec, R. Zboril and P. Schmuki, Conductive Cu-doped TiO_2 nanotubes for enhanced photoelectrochemical methanol oxidation and concomitant hydrogen generation, *ChemElectroChem*, 2019, **6**, 1244–1249.

190 R. Ding, J. Chen, Y. Chen, J. Liu, Y. Bando and X. Wang, Unlocking the potential: Machine learning applications in electrocatalyst design for electrochemical hydrogen energy transformation, *Chem. Soc. Rev.*, 2024, **53**, 11390–11461.

191 H. Xin, T. Mou, H. S. Pillai, S.-H. Wang and Y. Huang, Interpretable machine learning for catalytic materials design toward sustainability, *Acc. Mater. Res.*, 2024, **5**, 22–34.

192 S. Li, S. Wang, Y. Wang, J. He, K. Li, Y. Xu, M. Wang, S. Zhao, X. Li, X. Zhong and J. Wang, Doped Mn enhanced NiS electrooxidation performance of HMF into FDCA at industrial-level current density, *Adv. Funct. Mater.*, 2023, **33**, 2214488.

193 Essential role of lattice oxygen in methanol electrochemical refinery toward formate, https://www.science.org/doi/10.1126/sciadv.adh9487, (accessed 20 January 2025).

194 Y. Li, H. S. Pillai, T. Wang, S. Hwang, Y. Zhao, Z. Qiao, Q. Mu, S. Karakalos, M. Chen, J. Yang, D. Su, H. Xin, Y. Yan and G. Wu, High-performance ammonia oxidation catalysts for anion-exchange membrane direct ammonia fuel cells, *Energy Environ. Sci.*, 2021, **14**, 1449–1460.

195 P. Wang, H. Cui and C. Wang, Ultrathin PtMo-CeO hybrid nanowire assemblies as high-performance multifunctional catalysts for methanol oxidation, oxygen reduction and hydrogen oxidation, *Chem. Eng. J.*, 2022, **429**, 132435.

196 A. Badreldin, E. Youssef, A. Djire, A. Abdala and A. Abdel-Wahab, A critical look at alternative oxidation reactions for hydrogen production from water electrolysis, *Cell Rep. Phys. Sci.*, 2023, **4**, 101427.